The Applications of Microfluidic Platforms for Cancer Research: The Tumor Microenvironment and Drug Delivery Systems

by
Karolina Papera Valente
B.Sc., Instituto Superior Tecnico, Lisbon, Portugal, 2010
M.Sc., Instituto Superior Tecnico, Lisbon, Portugal, 2012

A Dissertation Submitted in Partial Fulfillment
of the Requirements for the Degree of

DOCTOR OF PHILOSOPHY

in the Department of Mechanical Engineering

University of Victoria

Supervisory committee

The Applications of Microfluidic Platforms for Cancer Research: The Tumor Microenvironment and Drug Delivery Systems

by

Karolina Papera Valente
B.Sc., Instituto Superior Tecnico, Lisbon, Portugal, 2010
M.Sc., Instituto Superior Tecnico, Lisbon, Portugal, 2012

Supervisory committee

Dr. Afzal Suleman, Co-Supervisor
Department of Mechanical Engineering

Dr. Alexandre Brolo, Co-Supervisor and Non-Departmental Member
Department of Chemistry

Dr. Rustom Bhiladvala, Departmental Member
Department of Mechanical Engineering

Abstract

This work describes the use of microfluidic technology and biomaterials in cancer research by mimicking the extracellular matrix (ECM) and development of drug delivery system. Initially, biomaterials such as Gelatin methacryloyl (GelMA) and collagen type I were combined to create a hydrogel composite able to mimic both healthy and cancerous ECM. The impact of the tumor microenvironment was analyzed by using the hydrogel inside of a pressurized microfluidic device and by tracking the movement of gold nanoparticles (GNPs). The GNPs showed a decrease in diffusion coefficient of 77% when analyzed in cancerous conditions. This investigation was further explored by analyzing the diffusion of charged GNPs in the same system, while also tracking cellular uptake. An inverse correlation between diffusion and cellular uptake was obtained for charged GNPs in breast cancer cells. Due to the tunable properties and biocompatibility of GelMA, this hydrogel was also employed in the development of pH-responsive drug delivery systems. Since GelMA contains a gelatin backbone, two responsive polymers (Polymers A and B) were synthesized. Microspheres of ~40 μm were fabricated in flow focusing microfluidic devices. Polymer A microspheres displayed a swelling increase of 167% in pH 6.0, while polymer B spheres showed a 296% swelling in pH 10. Considering the unique properties of the tumor microenvironment such as leaky vasculature and acid pH environment, polymer A was selected to be used in the production of nanocarriers. The behavior of this polymer in acidic environment illustrated its potential applicability as drug delivery systems to the tumor area. Polymer A nanogels displayed a uniform size of 74 ± 7 nm. Lastly, GNPs were added to the solution of polymer A, leading to the fabrication of GNPs-loaded nanogels, presenting a homogenous distribution of gold particles inside nanogels.

Table of contents

List of tables

List of figures

List of abbreviations

^1H NMR - proton nuclear magnetic resonance
2D - two-dimensional
3D - three-dimensional
AM - methacryl groups
APTES - (3-Aminopropyl)triethoxysilane
Au - gold
bFGF - basic fibroblast growth factor
bioMEMS - biological microelectromechanical systems
CAF - fluorescent carboxylated PS Latex Particles
CFP - capillary fluid pressure
CO_2 - carbon dioxide
Coll I - collagen type I
$CONH_2$ - amide
COOH - carboxylic acid
D_2O - deuterium oxide
DCIS - ductal carcinoma in situ
DMEM - dulbecco’s modified eagle’s medium
DOX - doxorubicin
DOX-DNA - doxorubicin conjugated to DNA
DS - degree of substitution
ECM - extracellular matrix
EMEM - eagle’s Minimum Essential Medium
EMT - epithelial mesenchymal transition
EPR - enhanced permeability and retention
FBS - fetal bovine serum
FRAP - fluorescence recovery after photobleaching
GelMA - gelatin methacryloyl
GMA - glycidyl methacrylate
GMA_1 - 3-methacryloyl-1-glycerylester
GMA_2 - 3-methacryloyl-2-glycerylester
GNP - gold nanoparticle
HCl - hydrochloric acid
HMDS - hexamethyldisilazane
ICP-MS - inductively coupled plasma mass spectrometry
IFP - interstitial fluid pressure
IgG - immunoglobulin G
LDH - lactate dehydrogenase
LFP - lymph fluid pressure
LSM - laser scanning microscope
MAA - methacrylic anhydride
MET - mesenchymal-epithelial transition
MMP - matrix metalloproteinase
MW - molecular weight
MWCO - molecular weight cut-off
$NaHCO_3$ - sodium bicarbonate
OH - hydroxide
OPC - oligodendrocyte progenitor cells
PBS - phosphate buffered saline
PCL - polycaprolactone
PDMS - polydimethylsiloxane
PEG - polyethylene glycol
pH - power of hydrogen
PS - polystyrene
RGD - arginine-glycine-aspartic acid
SEM - scanning electron microscope
Si_3N_4 - silicon nitride
SO_3H - sulfonic acid
SS - stainless steel
TEM - transmission electron microscope
THF - tetrahydrofuran
TMSP - trimethylsilylpropanoic acid
TMSPMA - (Trimethoxysilyl)propyl methacrylate
TNBS - 2,4,6,-Trinitrobenzenesulfonic
UV - ultraviolet
UV-Vis - ultraviolet–visible
VEGF - vascular endothelial growth factors

Acknowledgements

I am profoundly grateful to my supervisors Dr. Suleman and Dr. Brolo for giving me the opportunity and guidance to explore different ideas and to grow as a person and as a scientist. I would also like to thank my committee member, Dr. Bhiladvala, for his valuable feedback and advice during my doctoral degree and for the completion of this dissertation.

To all the members of the Brolo group who have encouraged and supported me along the way. Special thank you to Ugur Dagli for constantly believing in me, and to Bruno da Fonseca for all the encouraging words and for always being there for me (every single time). It has been an honor to be part of this group and to teach and learn together.

To Cameron Polglase for being so supportive, encouraging, helpful, and inspiring. I could not have asked for a better student to work with. I am very proud of everything we have accomplished, and I am sure that you will have a brilliant carrier. Thank you.

To Dr. Devika Chithrani for all the guidance, encouraging words and for believing in me. You are an inspiration to me.

To Carolyn Swayze, for all the support and for being such an inspirational woman.

To Laila Abelseth and Ian Fraser, for the endless help and support.

To Vanessa Muir, for being an amazing friend and for never doubting that I could do it.

To Mario Bras, for everything.

I also would like to thank Brent Owen for his assistance and support with TEM and to Christopher Barr for his help with HNMR. Thank you the CAMTEC staff, for their instruction in many of the instruments used.

To all my friends that have supported and helped me during this journey. I could not have done this without all of you.

To the Garlands, my family in Canada, for supporting, believing and encouraging me throughout the end of this journey. Thank you.

Lastly, I would like to thank my family for their endless support, trust, encouragement, and patience throughout this journey.

Karolina Papera Valente

University of Victoria

June 2020

Dedication

I dedicate this dissertation to all the women in Science: Search for your voice and when you find it, shatter the glass ceiling and make it to be heard.

And to Katarina, of course.

Chapter 1 Introduction[a]

Cancer is a devastating disease that affects millions of people every year. According to the National Cancer Institute, by 2024 almost 19 million people are expected to be living beyond a cancer diagnosis [1]. Due to the evident increase of people diagnosed with cancer and undergoing treatment, the National Expenditures for Cancer Care in the United States is projected to grow from US$125 billion in 2010 to US$156 billion in 2020.

Even though cancer is referred to as a single disease, cancer is composed by hundreds of diseases that have a main factor in common: uncontrolled cell growth. This group of diseases arise from a set of mutations on the cell DNA caused by genetic and environmental factors. Cancer defies the most basic behavior of normal cells such as controlled division, specialized character situated in a specific location of the body and survival just as long as required. Instead, cancer cells proliferate uncontrollably, invading territories of healthy cells and affecting the functionalization of different organs. Some cancer cells have the ability to migrate from their primary tumor location to a different location in the body through blood vessels and lymphatic system during metastasis [2, 3]. This invasion of new organs is responsible for about 90% of cancer deaths [4, 5].

Cancers can be diagnosed during routine tests such as physical examination, blood tests or screening procedures. More specific tests can be requested by the physician in order to confirm the occurrence of cancer [6]. Once the cancer is confirmed, different treatment approaches may be taken depending on the type of cancer, size of the tumor and the ability of the person to tolerate

---

[a] The following chapter contains excerpts from: Valente, K.P; Khetani,S.; Kolahchi, A.R.; Sanati-Nezhad, A.; Suleman, A.; Akbari, M. Microfluidic technologies for anticancer drug studies, *Drug Discovery Today*, **2017**, 22, 11, 1654-1670.

certain side effects [6]. Treatment options consist of surgery, radiation therapy, systemic therapy (chemotherapy) and target therapy.

In order to better understand this devastating disease and to better predict the response of cancer to current therapeutic treatments, traditional drug studies are performed in two-dimensional (2D) cultures, where cells are seeded on flat plates to form a monolayer. This method has been extensively used by researchers and pharmaceutical companies due to its simplicity. However, the translation of the results obtained from cancer cell monolayers to a tumor is not very promising since 2D models are unable to replicate the cell-cell and cell-extracellular matrix signaling of complex three-dimensional (3D) tissues [7]. For instance, in a 2D model, the cells are cultured on hard plastic substrates and are exposed to uniform concentrations of nutrients and drugs in a static condition [8]. However, natural tumor cells reside in a 3D matrix with a disorganized network of blood vessels that distribute the bioactive molecules non-uniformly [9]. Therefore, great effort has been made during the past few years to develop more reliable *in vitro* models by utilizing biomaterials and microfluidic technology [9]. Three-dimensional cell cultures allow the combination of multiple cell types and the presence of stromal and extracellular matrix [10]. Moreover, the cell-cell and cell-ECM interactions combined with a 3D architecture creates a closer functional resemblance of the *in vivo* tumor. In addition, 3D tumor models demonstrate less sensitivity to cytotoxic agents.

There are different methods used in the creation of 3D cell cultures, such as spheroids (agglomeration of cells) and scaffolds. Spheroids have been widely used in the development of 3D high throughput cell culture systems. The advantages of the use of spheroids over 2D cell cultures are numerous such as the recapitulation of a 3D architecture of the tissue, including hypoxic regions on larger spheroids, and the possibility to recreate cell-cell and cell-matrix interactions

[11]. Spheroids can also better mimic the response of the 3D tumor to cytotoxic treatments in terms of drug sensitivity and resistance [12]. However, even though the benefits of using spheroids are evident, there are still a few challenges to be overcome since spheroid culture is time-consuming, requires intensive labor and may lack consistency in the production of uniform spheroid sizes [12].

Even though spheroids are able to mimic the 3D architecture of tumor and tissues, spheroids still lack the presence of chemical and physical properties of the extracellular matrix. Bioengineered scaffolds have been extensively used for mimicking the complexities of the tumor microenvironment [13]. Scaffolds provide a 3D structural support to the cells and mimic physicochemical cues of the native tissue [14]. Scaffolds can be produced from naturally-derived materials [15] or synthetic biomaterials [15, 16] using biofabrication strategies including electrospinning [17], particle-leaching [18], direct writing [19], and weaving [20].

Hydrogels can be used as scaffolds. Hydrogels are 3D networks composed of polymeric materials (natural and synthetic) capable of absorbing a considerable amount of water and swelling in aqueous medium, while maintaining physical integrity due to the presence of hydrophilic functional groups (-OH, -COOH, $-SO_3H$ and $–CONH_2$) [21]. The use of hydrogels as scaffolding materials has recently drawn much attention as their physicochemical properties can be tuned to match the properties of the natural tissue [22, 23].

Comparatively to spheroids, scaffolds combine properties of the ECM in order to better recapitulate *in vivo* cell-ECM interactions. The presence of a scaffold provides not only structural support to encapsulated cells, but may also affect cell behavior and function [24]. However, there are still limitations on the use of bioengineered scaffolds. Synthetic, natural or a combination of both, the material used in the construction of a scaffold needs not only to be compatible but also required to match the mechanical properties seen in the natural tissue [25]. The matching of stiffness, elasticity, porosity and biodegradability rate can be challenging for the case of highly complex tissues and may require the combination of more sophisticated and complex biomaterials.

Even though 3D cell culture models present many advantages when compared to 2D cell monolayers, 3D cell cultures still do not mimic relevant key aspects of *in vivo* tissues [26]. 3D *in vitro* cell cultures fail to reproduce a dynamic environment, where interactions and communications between different cell cultures is seen in presence of fluid flow perfusion [27, 28]. Microfluidic technology has been applied to bioengineering research in order to overcome the limitations seen in the current 3D cell culture models.

Microfluidic technology is based on the field of biological microelectromechanical systems (bioMEMS) and it has been employed in chemistry, pharmaceutical, biological and medical research. Microfluidics studies the transport and manipulation of microliter/nanoliter volumes in channels with dimensions as small as the human hair [29]. With the advent of microfluidics technology, novel culturing platforms have been emerged that can be continuously perfused and imitate the physiological functions of tissues and organs [30].

Microfluidic devices allow the creation of an *in vitro* tumor environment that closely resembles the *in vivo* situation due to precise spatial and temporal control of nutrients, oxygen and cytotoxic drug delivery [8] and integrated biochemical and mechanical features [27]. In addition to providing a more realistic *in vitro* environment for small-scale systems, microfluidic devices are cost-efficient since they require small sample and reagent volumes, transparent and can be used to perform high throughput assays [31].

Microfluidic technology can also be applied to the development of drug delivery systems. Drug carrier particles can be fabricated in droplet-based microfluidic devices displaying mono-dispersed and size-controllable nano/microparticles [32]. When compared to bulk methods, microfluidics allow the generation of monodispersed particles with high encapsulation efficiency based on the control of the geometries of the chip and flow rate of solution [33].

1.1. The Tumor Microenvironment

Tumor microenvironment is complex and plays an important role in the growth, invasions and metastasis of cancers [34]. The environment of a normal tissue is extremely altered in presence of a tumor. The invasion and the proliferation of cells in the tumor can reorganize the ECM of the tissue, increase interstitial pressure, and create hypoxic regions within the cells [35] (**Figure 1.1**). The ECM is mainly composed of biomolecules such as proteins, polysaccharides and water and it is responsible for providing a physical scaffold for cells, containing biochemical and biomechanical cues that can direct cellular differentiation and homeostasis [36].

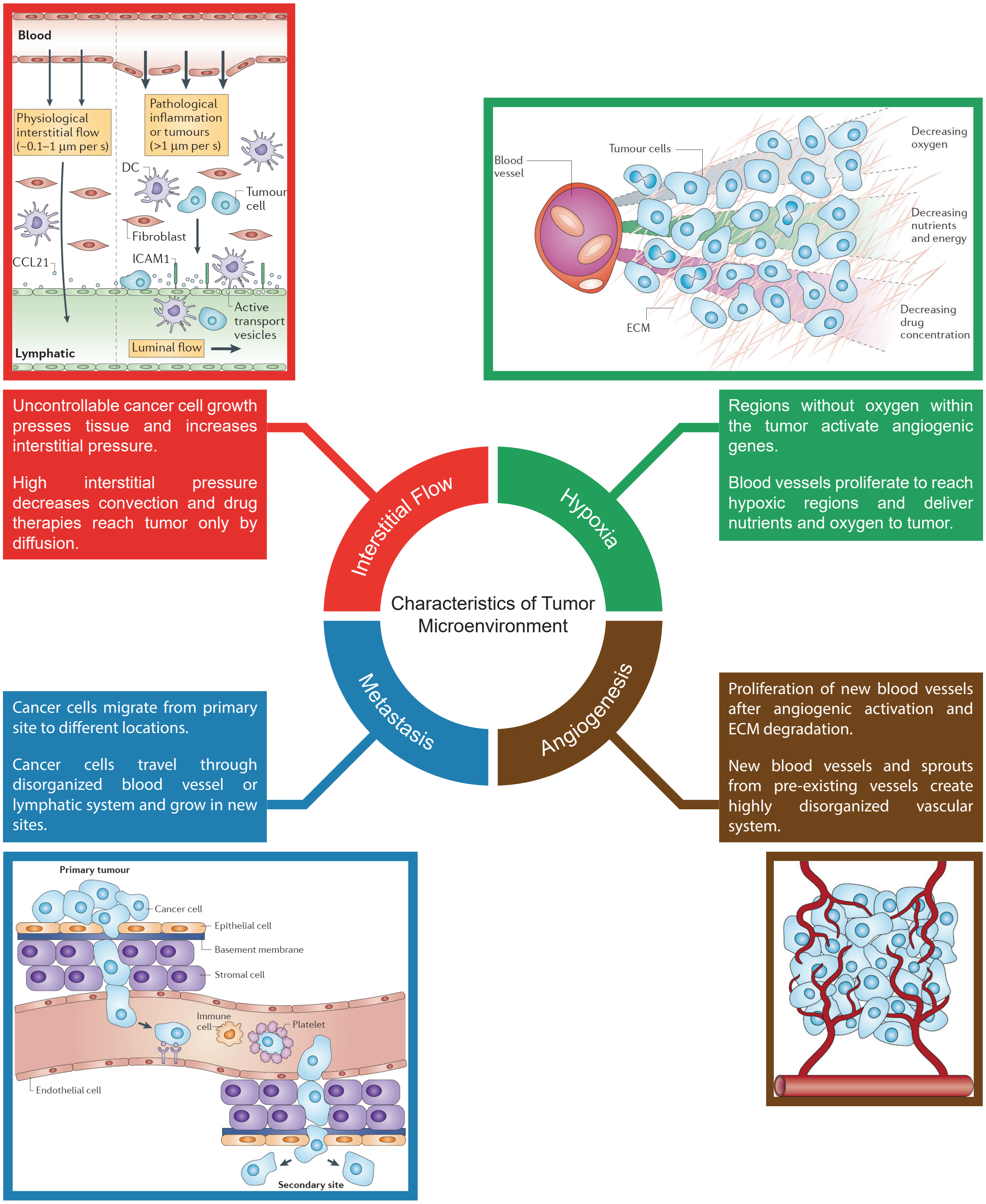

Uncontrollable cancer cell growth presses tissue and increases interstitial pressure.

High interstitial pressure decreases convection and drug therapies reach tumor only by diffusion.

Regions without oxygen within the tumor activate angiogenic genes.

Blood vessels proliferate to reach hypoxic regions and deliver nutrients and oxygen to tumor.

Cancer cells migrate from primary site to different locations.

Cancer cells travel through disorganized blood vessel or lymphatic system and grow in new sites.

Proliferation of new blood vessels after angiogenic activation and ECM degradation.

New blood vessels and sprouts from pre-existing vessels create highly disorganized vascular system.

Figure 1.1 Characteristic of the tumor microenvironment
Abnormal interstitial flow caused by pressure of cancer cells on tissue results in drainage of tissue lymphatics and decreases the efficacy of drug therapies. Hypoxia caused by absence of oxygen results in the activation of angiogenic genes. Angiogenesis resulting from the activation of angiogenic genes causes the proliferation of blood vessels and a disorganized blood network. Tumor metastasis results from the migration of cancer cells from the primary site to different tissues via intravasation into blood vessels and the lymphatic system [37].

In addition to waste products, the degradation of protein components such as collagen and fibronectin also occurs inside the tissue [29]. This protein deposition creates a stiffening in the ECM and it is a diagnostic indicator in solid cancer [38]. A deregulated and abnormal ECM can also influence the behavior of endothelial cells, playing an important role in tumor angiogenesis [39]. Moreover, the structure of the vascular network in tumors is highly disorganized, display unusual leakiness and express surface molecules that mediate the diffusion of tumor cells in the bloodstream and preserve the tumor microenvironment [40]. Such abnormalities in the tumor tissue results in the resistance of tumor cells to therapeutic agents and affects the transport of drug within the tumor [41].

1.1.1. Effect of Hypoxia and Interstitial Pressure on Drug Penetration

One of the most well-known hallmarks of cancer is uncontrollable growth and multiplication of cancer cells [42]. Since this growth occurs within a healthy tissue, the cancer cells develop a ‘stressful’ environment by pressing the cancer on the surrounding tissue and extracellular matrix. Elastic stress (in terms of Young’s modulus) increases on this tissue, which can in return result in an increase in the intratumoral pressure [43]. The increase in pressure creates an interstitial fluid flow from the tumor to the surrounding healthy tissue, draining tissue lymphatics [41, 43–45]. Poorly organized vascularization system combined with the rapid proliferation of cancer cells increases the amount of toxins and biomolecules, contributing to a raise in pressure in the tissue. These inhibits the distribution of large molecules by convection (pressure gradient) [43, 45–47]. Therefore, within solid tumors, it is very common to see the presence of hypoxic regions [35]. In these hypoxic regions, cancer cells use oxidative pathways to metabolize and produce more lactic acid and carbonic acid [48]. Consequently, the increase in interstitial pressure does not allow a good clearance of waste products, due to an increase in localized pressure, and alters the pH within the tumor (decrease in pH from 7.4 to 5.8 in some cancers) [45].

1.1.1.1. Hypoxia

Hypoxic regions are present in most tumors and they increase the resistance of the cancer to therapeutic treatments [41]. In the case of systemic therapy, cytotoxic drugs are delivered to damage fast growing cells. However, in many tumors blood flows in a disorganized manner and, due to excessive growth of cancer cells, blood vessels are not capable to reach all parts of the tumor, generating hypoxic regions where neither oxygen, nutrients or cytotoxic drugs can be delivered to the cells [41, 45] . Consequently, hypoxic regions are often close to necrotic regions and are therapeutic resistance [45, 49]. However, in order to survive, tumor hypoxia activates genes associated to angiogenesis in cancer cells [49] by secreting angiogenic activators such as vascular endothelial growth factors (VEGF) and basic fibroblast growth factor (bFGF) [50–52]. These angiogenic factors stimulate proliferation of blood vessels by sending a signal to induce new endothelial cell growth and ECM degradation (matrix metalloproteinases) [50]. The degradation of the ECM allows endothelial cells to migrate and to start the division process, initiating blood vessel growth and sprouting from pre-existing blood vessels [50, 51]. Once vascularized, the tumor is free to grow and to metastasize to different regions of the body [53].

1.1.1.2. Interstitial Pressure

Chemotherapeutic drugs can penetrate healthy tissues by diffusion and convection [41]. While convection depends on a gradient of pressure between the blood vessel and the interstitial space, diffusion occurs due a concentration gradient within the tissue. In healthy tissue, the interstitial fluid is composed of an influx of nutrients and oxygen from blood vessels [43]. In the case of cancerous tissue, the interstitial fluid is poorly drained due to the lack of lymphatic vasculature [41], resulting in an increase in interstitial pressure. Also, cancer cells invade a healthy tissue by pressing and pushing the surrounding environment, creating an increase in pressure inside of the tumor and resulting in a large differential pressure between the tumor and the healthy tissue. This pressure gradient acts against the transport of nutrients and drugs from the blood vessels. Therefore, the drug penetration and distribution is limited to diffusion, decreasing the efficacy of systemic therapies [45].

1.2. Microfluidic Technology in Cancer Research

Microfluidic platforms have been recently emerging as powerful tools for recreating the complexities of the natural tissues and disease modelling [54, 55]. Due to the small dimensions, laminar flow is seen inside the channels and viscous forces dominate over inertial forces [27]. Mass transport of nutrients and gases inside microfluidic devices occurs by diffusion, which closer mimic the *in vivo* delivery of nutrients. Small dimensions of channels allow precise control of the system and low volume of reagents which, consequently, reduce equipment and sample costs. In addition, the small dimensions are comparable to the dimensions encountered inside the human body, allowing a better replication of human tissues *in vitro*. Microfabrication techniques are used in the development of microfluidic devices including soft lithography and replica molding, injection molding, and 3D printing [56]. Among different materials, poly(dimethylsiloxane) (PDMS) is the most common material used in microfabrication. PDMS is a transparent biocompatible silicon-based polymer that allows high gas permeability, providing enough oxygen permeation to cell culture systems [27]. Microfabrication techniques present sufficient flexibility to develop different designs of microfluidic devices. Therefore, the addition of chemical gradients generator combined to sensing technology and mechanical stimuli allows the development of predictive platforms of human physiology and disease for drug development [30]. **Table 1** lists the advantages of microfluidic devices of traditional 2D and *3D in vitro* cell culture models.

	Advantages	Disadvantages
2D Cell Culture 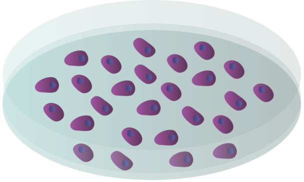	• Methodology well established • Simplicity to work with cell monolayer	• Static conditions • Uniform concentration of nutrients and drugs • Lack of 3D environment • Large reagent volumes
3D Cell Culture 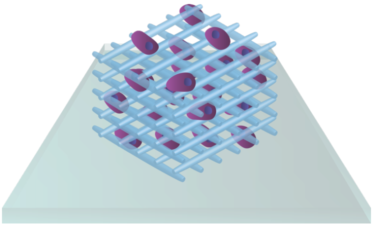	• Cell-cell and cell-ECM interactions • Sensitivity to cytotoxic agents similar to *in vivo*	• Fail to produce dynamic environment • Lack of fluid flow perfusion
Microfluidic Platforms 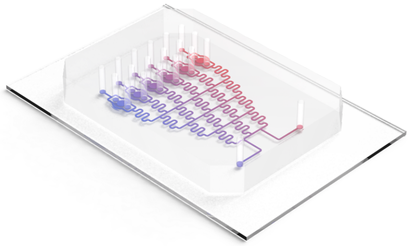	• Higher control of environment • Diffusion of nutrients and drugs • Cost-effective • Combination of CGG, biosensors and mechanical stimuli • High throughput assays	• Non-standardized protocols • PDMS may adsorb molecules • Perfusion of more than one growth medium can be challenging

Table 1. Advantages and disadvantages of *in vitro* cell culture models.

Microfluidic devices have been extensively used to cancer research. Due to the high flexibility of architectural design fabrication, different types of cancer models can be developed in microfluidic platforms. Most cancer-on-chip models are of breast, lung, and liver cancers due to their high incidence rates [57].

Breast cancer is still one of the most dangerous types of cancer, responsible for more than 40 thousand estimated deaths for US only in 2016 [57]. Therefore, great effort has been made to develop microfluidic-based breast cancer models and investigate the cancer progression and efficacy of different drugs. For instance, a multichannel microfluidic device was developed to investigate the crosstalk of breast cancer cells and immune cells [58]. In this study, MDA-MB-231 breast cancer cells were suspended in collagen and injected in two channels of the microfluidic device (**Figure 1.2A**). Macrophages were then suspended in Matrigel and injected in the central channel, between the two breast cancer collagen channels. The co-culture was incubated for over one week and no movement was seen in the breast cancer culture towards the Matrigel layer. The macrophages, on the other hand, migrated and invaded the collagen cancer cells on day 3. This invasive behavior was more extensively seen after 7 days, when macrophages also showed an increase in number due to the multiplication when in presence of MDA-MB-231 cells. The results of this study proved the ability of microfluidic platforms to mimic the crosstalk between the cancer cells and the immune cells.

Ductal carcinoma in situ (DCIS) is a type of non-invasive breast cancer that occurs inside of the milk duct. However, some of these cancer cells have the ability to migrate from the original duct region to the surrounding tissue (Invasive Ductal Carcinoma). A microfluidic platform to replicate DCIS in a 3D *in vitro* model was developed, composed of upper and lower channels separated by a collagen membrane (**Figure 1.2B**) [59]. The lower channel recreated the stromal tissue exist in the mammary duct by seeding cancer associated fibroblasts on a collagen coated membrane. Endothelial cells, on the other hand, were cultured in the presence of a mixture of Matrigel and fibronectin on top of the collagen membrane. The culture of different cell types was possible in the DCIS-on-a-chip model due to the presence of two chambers, where different types of growth medium were delivering nutrients to the cell cultures. DCIS spheroids were allowed to adhere to the epithelial layer on the top channel. Cytotoxic evaluation of anticancer drug paclitaxel (20 nM) was performed by injecting the drug on the lower channel (stromal-like culture) for 24 h in order to simulate an intravenous administration of the drug. Lactate dehydrogenase (LDH) levels released from the epithelial cells and fibroblast were used to assess drug cytotoxicity. The results indicated that production of LDH doubled at day 4 when DCIS spheroids were present in the upper channel. However, in the case of the control experiments performed in the chip in presence of a monolayer of epithelial cells, no change in cytotoxicity was seen. Spheroid sizes inside the microfluidic device in presence and in absence of the anticancer drug were compared and the results indicated the efficacy of paclitaxel. Untreated spheroids were nearly threefold the size of the treated spheroids. The results indicated the importance of developing a 3D architecture and microenvironment to assess cytotoxicity of cancer drugs.

Cancer can become even more complex to treat when it migrates from its original place to different tissues inside the body. Tumor extravasation is known as metastasis and it has been largely explored using microfluidic systems. The extravasation of breast cancer cells to bone was studied using a 3D microfluidic model [60]. The microfluidic platform was composed of eight gel channels and three media channels and it was previously used to investigate angiogenesis [61–63]. A tri-culture system was generated by the injection of human osteo-differentiated bone marrow-derived mesenchymal stem cells embedded in a collagen matrix in one of the channels, while endothelial cells were seeded in the central channel to create an endothelial cell barrier covering the lateral wall of the channels. Breast cancer MDA-MB-231 cells were introduced in the endothelial channel (**Figure 1.2C**). The results demonstrated that the cancer cells migrated trough the collagen layer by penetrating the endothelial barrier. This migration was also confirmed in the absence for osteo-differentiated bone cells. However, in presence of the osteo-cells, 77.5% of cells migrated to the bone matrix, compared to only 38% extravasation rate seen when pure collagen was present. To further study the role of the osteo-differentiated bone cells in the extravasation of breast cancer cells, the expression of chemokine CXCL5 was investigated in the bone compartment. This specific chemokine is known to be involved in cancer migration by expression of surface receptor CXCR2 [64]. The production of CXCL5 by the bone cells was confirmed and the expression of CXCR2 surface receptor was shown to be present in cancer cells. After blocking the CXCR2 receptor, the rate of cancer cell extravasation dropped from 77.5% to 45.8%. This study elucidated the use of microfluidic system to study cancer metastasis, where different cell lines could be cultured inside of a chip.

Lung cancer is one of the leading causes of death by cancer and is responsible for 27% of all deaths by cancer in 2016 in the United States [57]. The high mortality rate is due to the fact that symptoms of lung cancer are difficult to be distinguished from normal infections or disorders arise from the side effects of smoking. Therefore, the lung cancer is generally diagnosed in advanced stages. Lung cancer metastasis was studied in a multi-organ microfluidic device composed of a lung and three "distant organs": brain, bone and liver (**Figure 1.2D**) [65]. Lung cancer A549 cells cultured inside the microfluidic device formed a cancer mass, showing epithelial mesenchymal transition (EMT), whereas the level of EMT markers (E-cadherin, N-cadherin, Snail 1 and Snail 2) were used to evaluate the invasion of A549 cells to the "distant organs". In addition, the formation of a tumor mass in the brain, bone and liver was analyzed by mesenchymal-epithelial transition (MET) makers. The results indicated that the expression of the markers in the A549 cells found in the "distant organs" pointed out that the lung cancer cells had metastasized from its primary site to the different organs in the microfluidic device. This invasive capability was only possible to be analyzed due to the integration of multi-organs-on-chip, promoting the investigation of cell-cell interactions during the process of metastasis.

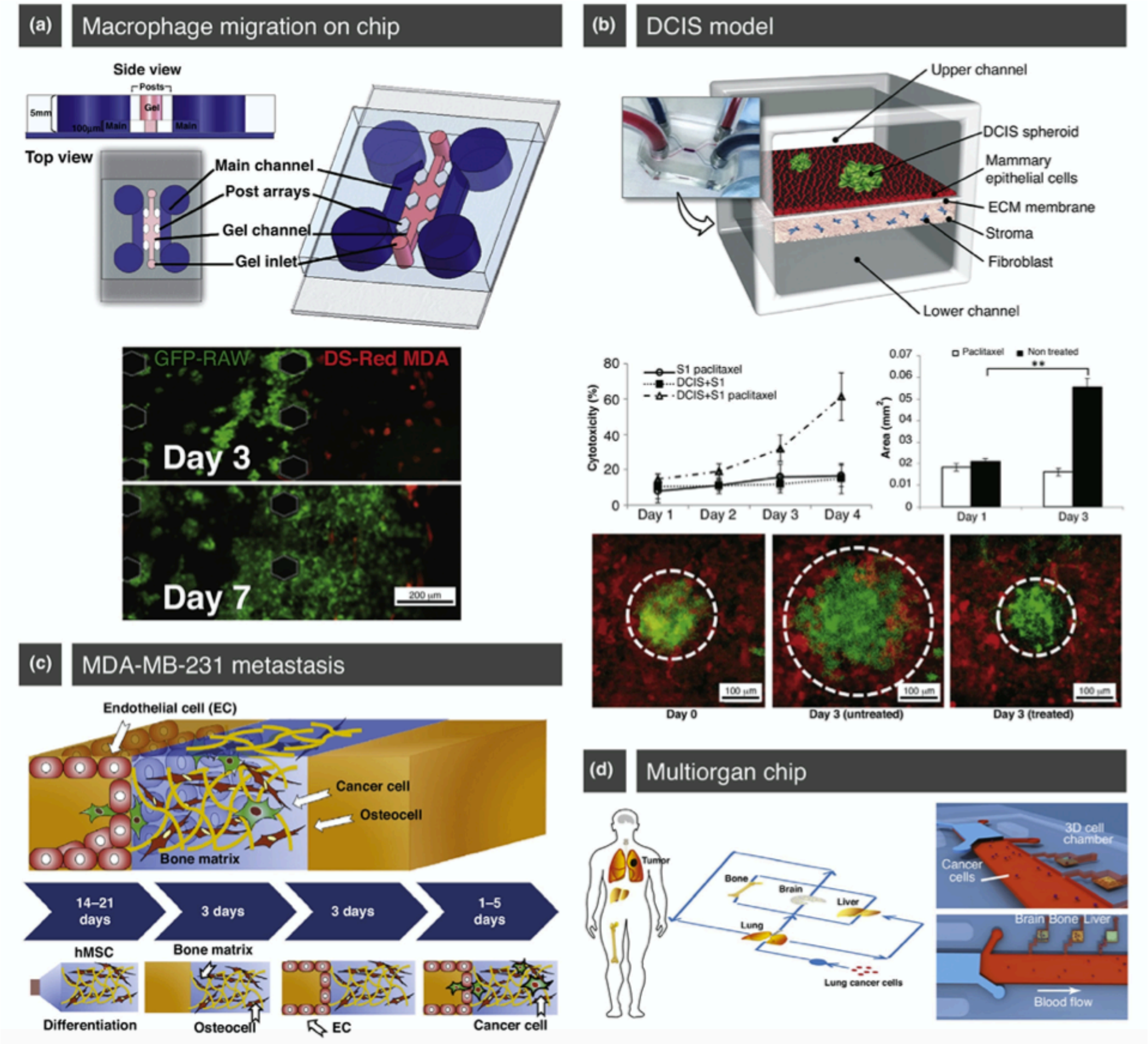

Figure 1.2 Biomimetic *in vitro* cancer models

(a) Microfluidic device for cell co-cultures in different matrices: design of the chip (top) and migration of macrophages (in green) toward tumor cells (in red) suspended in Matrigel (bottom). (b) Microfluidic platform to mimic the microarchitecture of ductal carcinoma in situ (top) composed of upper and lower cell channels separated by an extracellular matrix (ECM)-derived membrane. Cancer spheroids were embedded in the mammary epithelial layer on the upper channel, where a fibroblast-containing stromal layer was formed in the lower chamber. The effect of paclitaxel in the breast tumor- on-a-chip (bottom) is illustrated by fluorescence micrographs of the spheroid sizes (shown in green) in absence and in presence of the cytotoxic drug. (c) 3D microfluidic device for MDA-MB-231 breast cancer cell extravasation to bone: generation of the osteo-cell-conditioned microenvironment, where endothelial cells were cultured to create a barrier covering the lateral wall of the microchannels and breast cancer cells were seen to migrate toward the differentiated bone cells through the endothelial layer. (d) Biomimetic multiorgan microfluidic chip system composed of lung, brain, bone, and liver for the study of metastasis of lung cancer cells to ‘distant organs’ [37].

Microfluidic devices present many advantages over conventional 2D and 3D cell culture models, including high spatial and temporal control of the system, the use of low sample volumes and the ability to incorporate mechanical and chemical features in the platforms. However, there are still a few challenges to be overcome. For instance, most microfluidic devices are developed for very specific applications and, consequently, there is a lack of translation from one type of cancer to another using the same platform. In addition, the integration of different types of biochemical factors to recapitulate a more complex tumor microenvironment is still a challenge [66]. Limitations can also be seen in the extraction of data from microfluidic devices: most results can only be obtained using microscopy, whereas a large amount of information in terms of molecular level is lost [67].

1.3. Nanoparticle Technology in Cancer Research

Nanoparticles are materials with nanoscale dimensions, normally between 1 to 100 nm. Nanoparticles can have different material composition, depending on the application. In medical applications, semiconductor and magnetic nanoparticles have been used for imaging, providing considerable improvement in the quality of tissue and organ images [68].

Nanoparticles have also been extensively used as nanocarriers in nanomedicine in order to systemically deliver drug to cancerous tissues. The unique features seen in solid tumors, such as a leaky vasculature, leads to an increase of penetration and accumulation of nanoparticles around cancerous areas [69]. This process is known as enhanced permeation and retention (EPR) effect and happens in vascularized tumors. After reaching the tumor, nanoparticles can then release the drug to the cancer cells. While different strategies can be used to target the tumor areas [70], the particles need to exhibit the certain properties. First, since the leaky vasculatures present pore sizes around 400 nm, the nanoparticle dimensions must be below this cut-off size in order to perform an efficient extravasation [69, 70]. However, the kidneys and liver also have a big impact on nanoparticle size. Particles smaller than 10 nm undergo renal clearance, while the liver is capable of capturing particles above 100 nm [71, 72]. Therefore, the size of the nanoparticles should be in the range of 10-100 nm. Second, the transport of nanoparticles inside the body is also highly affected by their surface charge. Cationic and anionic particles have high propensity to stimulate phagocytosis and, therefore, are cleared from circulation faster than neutral particles [73]. A well-known strategy to create a neutral charge on the nanoparticle surface is to coat the particle with polyethylene glycol (PEG) [74]. PEG-coated nanoparticles have increased circulation time inside the body due to the reduction of interactions with protein and opsonins (molecules that enhance phagocytosis) [75]. Lastly, particle shape can also affect the biological response of the body to the nanoparticles. Black et al. [76] studied the impact of different gold-doped nanostructures, such as nanospheres, nanodisks and nanorods, in biodistribution tumor uptake and intratumoral distribution applied to a murine breast cancer models. The results showed that nanospheres circulated longer in the blood stream. In addition, nanospheres also showed least clearance by phagocytosis and resulted in better and higher accumulation in the tumor area.

The applications of nanoparticles in diagnosis and cancer treatment also extends to radiation therapy. Gold nanoparticles can be applied as radiotherapy enhancers due to the high atomic number (Z) of gold [77] . For instance, McQuaid et al. [78] saw an enhancement of 14 fold when MDA-MB-231 cells were cultured with 1.9 nm gold nanoparticles (500 μg/mL) and irradiated with 3 Gy. Kong et al. [79] used 15 nM of 10.8 nm gold nanoparticles to analyze the radiosensitization using MCF-7 cells. The results showed that after an X-ray dose of 10 Gy, the nanoparticles increased radiation cytotoxicity by 60%. Chattopadhyay et al. [80] developed a human epidermal growth factor receptor-2 (HER-2) targeted gold nanoparticles for enhanced X-ray treatment, using trastuzumab as a targeting agent. The ability to enhance the breakage of DNA strands in breast cancer cells (SK-BR-3) was evaluated after exposure of the cells ($6x10^4$ cells/well) to 0.3 nM of 30 nm gold nanoparticles (~$2x10^{11}$ particles/mL) and treated with up to 1 Gy of 300 kVp of X-radiation. An enhancement of 5.1-fold was obtained with the gold nanoparticles, compared to radiation alone. Starkewolf et al. [81] developed doxorubicin (DOX) conjugated to DNA strands attached to the surface of gold nanoparticles in order to trigger the release of DOX by X-ray. DOX-DNA-gold nanoparticles were incubated with breast cancer cells (MCF-7) for 12 hours before exposure to up to 10 Gy, where an enhancement in toxicity of 33 ± 21% for 10 Gy was seen, compared 1 ± 15% with 2 Gy.

1.4. *In vitro* Diffusion of Nanoparticles

As described in the previous section, most *in vitro* models used in nanoparticle studies are normally 2D cell culture models. Therefore, nanoparticles are directly deposited on top of the cells. This direct delivery of nanoparticles to cell monolayers does not mimic the highly complex delivery witnessed *in vivo*. Tumor microenvironment is complex and plays an important role in the growth, invasion and metastasis of cancers [34]. The environment of a normal tissue is extremely altered in presence of a tumor. The invasion and proliferation of cells in the tumor can reorganize the extracellular matrix of the tissue, increase interstitial pressure, and create hypoxic regions within the cells [35]. The ECM is mainly composed of biomolecules such as proteins, polysaccharides and water and it is responsible for providing a physical scaffold for cells, containing biochemical and biomechanical cues that can direct cellular differentiation and homeostasis [36].

A strategy to mimic the ECM *in vitro* is to use hydrogels for cell encapsulation. When cells are encapsulated in a hydrogel matrix, the delivery of drugs/nanoparticles happens chiefly by diffusion [82, 83]. Quignard et al. [84] investigated the diffusion of fluorescent silica nanoparticles in collagen hydrogels. A 2 mm thick collagen layer with entrapped fibroblasts was created in order to mimic the dermis. Nanoparticles were deposited on top of the thick hydrogel film and diffusion of the particles was analyzed by measuring the fluorescence from collected samples at the bottom of the hydrogel layer (**Figure 1.3**). The results indicated the impact of collagen concentration in the diffusion of 60 nm silica particles: when the collagen concentration was high (5 mg/mL), the particles diffused much slower than at low concentrations of collagen (1.5 mg/mL), where diffusion coefficients of 2 x 10^{-7} cm^2/s and 11 x 10^{-7} cm^2/s were obtained, respectively. Interesting, when the diffusion of the 60 nm particles was evaluated in collagen containing fibroblasts, no significant difference was seen, where a diffusion coefficient of 3 x 10^{-7} cm^2/s was obtained for a collagen concentration of 3 mg/mL and 4 x 10^{-7} cm^2/s was obtained in absence of fibroblasts.

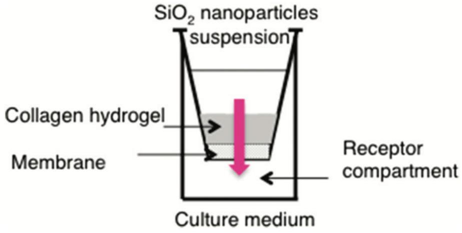

Figure 1.3 Set-up for diffusion studies of silica nanoparticles through collagen hydrogel [45]**.**

Tomasetti et al. [85] studied the impact of PEGylation on nanoparticle mobility in two different ECM models: Collagen I and Matrigel. Collagen I is a neutrally charged gel, while Matrigel is a basement membrane with strong negative charge. The final collagen I concentration of 5 mg/mL formed a gel with median pore size of ~470 nm, while 7.4 mg/mL Matrigel samples showed a median pore size of 140 nm. The diffusion of 120 nm silica nanoparticles was investigated by Fluorescence Recovery After Photobleaching (FRAP) measurements of regions of interest in the ECM-like gels with encapsulated nanoparticles. The results showed that the reduction of particle surface charge with PEG resulted in mobility improvements in both matrices. However, the results also demonstrated that diffusion coefficients were ten times higher in collagen I than in Matrigel, whereas diffusion coefficients of 4 x 10^{-8} cm^2/s and 0.4 x 10^{-8} cm^2/s were obtained for collagen I and Matrigel, respectively.

1.4.1. Integration of Nanoparticles with Microfluidic Systems

Currently, the major focus in cancer medicine is the transport of nanoparticles/nanocarriers to cells and tissues [86]. However, most *in vitro* studies are restricted to 2D transport, chiefly due to ease of fabrication. The integration of nanoparticles in microfluidic systems allows the study of diffusion in a 3D *in vitro* model that more closely mimics the reality seen *in vivo*. Raeesi et al. [87] investigated the effect of near-infrared light stimulation of PEGylated gold nanorods in a 7 mg/mL collagen I matrix inside a microfluidic device. The microfluidic device consisted of a rectangular channel with one inlet and one outlet. The central channel was filled with collagen I gel and nanorod solution was injected in the inlet reservoir. A near-infrared laser (785 nm) was used to excite the nanorods, causing an increase in temperature up to 55 ºC (photo-thermal effect) (**Figure 1.4**). The increase in temperature created an irreversible denaturation of the collagen I matrix. The change in the collagen matrix was evaluated in terms of diffusion of 50 and 120 nm AlexaFluor labeled-gold nanoparticles throughout the central channel of the microfluidic device. Without photo-thermal effect, the fluorescence seen in the central channel was low, indicating low diffusion of the nanoparticles. After irradiation with the laser, higher average fluorescence intensity was seen inside the chip, showing an increased penetration by the nanoparticles in the collagen I matrix. The photo-thermal effect resulted in an increased diffusivity of 50 nm and 120 nm by ~14-fold and ~21-fold, respectively. In addition, it was evaluated that 120 nm nanoparticles were 4.5 times slower than the 50 nm particles, with effective diffusivity of 7.22 x 10^{-8} cm^2/s and 2.36 x 10^{-7} cm^2/s, respectively.

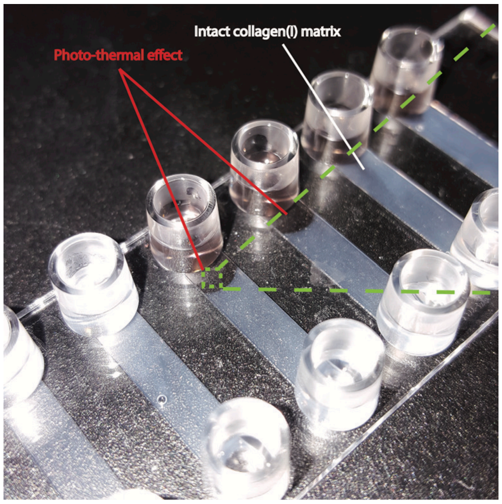

Figure 1.4 Effect of photo-thermal GNRs on collagen I matrix [47]**.**

Albanese et al. [88] developed a tumor-on-a-chip platform to investigate the diffusion of fluorescently labelled PEGylated gold nanoparticles in breast cancer spheroids (**Figure 1.5**). Gold nanoparticles with different hydrodynamic diameters, ranging from 40 nm to 150 nm, were injected inside the chip at 50 µL/h and the accumulation of the particles was verified in the MDA-MB-432 tumor spheroid. The results indicated that 40 and 70 nm nanoparticles could be seen inside the interstitial space of the spheroid within 10 minutes of flow. However, in the case of 110 and 150 nm particles, the accumulation of those particle was much less, showing the effect of size on the delivery of nanoparticles.

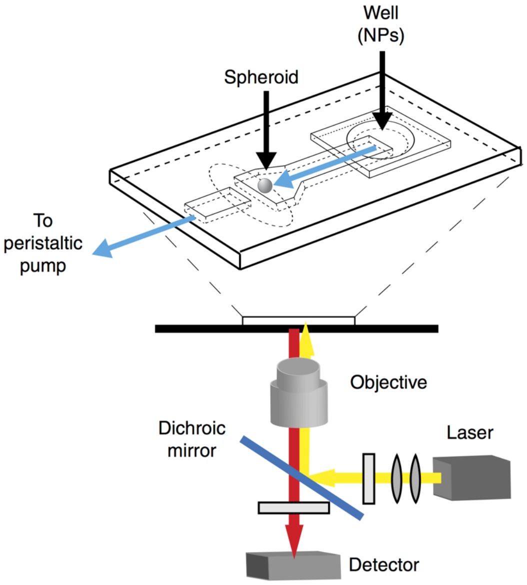

Figure 1.5 Schematic of the PDMS microfluidic device on a microscope stage for investigation of diffusion in spheroids [48]

In a more complex study, Kwak et al. [89] investigated the diffusion of fluorescent polystyrene nanoparticles inside a tumor-microenvironment-on-chip system. The chip was composed of two layers, separated by a polycarbonate membrane. The top layer was composed of a channel that simulated the capillary vessel of a tumor. The bottom layer, on the other hand, contained an interstitial channel, where breast cancer cells (MCF-7) encapsulated in collagen were injected and two lateral channels, mimicking the lymphatic vessels. In order to create a functional endothelium, the polycarbonate membrane was coated with Matrigel and seeded with endothelial cells. The cell culture channel was pressurized to 20 mmHg, while the pressures in the capillary channel and in the lymphatic chambers were 20 mmHg and 5 mmHg, respectively (**Figure 1.6**). The diffusion of 100, 200 and 500 nm fluorescent nanoparticles (10^{11} particles/mL) from the capillary channel through the tumor channel was detected by time-lapse fluorescence images. Since the pore size of the polycarbonate membrane was 400 nm, the diffusion of 500 nm particles was not detected as the particles were unable to cross the membrane. In the case of 100 nm and

200 nm particles, effective diffusivity values of 3.3 x 10^{-8} cm^2/s and 4.4 x 10^{-8} cm^2/s were obtained, respectively, when 3 mg/mL collagen I matrix was used. The effect of tissue microstructure was also investigated by increasing the collagen concentration from 3 mg/mL to 6 mg/mL in order to develop a denser matrix. For the case of 100 nm particles, the effective diffusivity value decreased from 3.3 x 10^{-8} cm^2/s to 1.7 x 10^{-8} cm^2/s, emphasizing the effect of ECM composition on transport of particles. Therefore, the tumor-microenvironment-on-chip was capable of providing information about nanoparticle transport and behavior in a breast tumor-like environment.

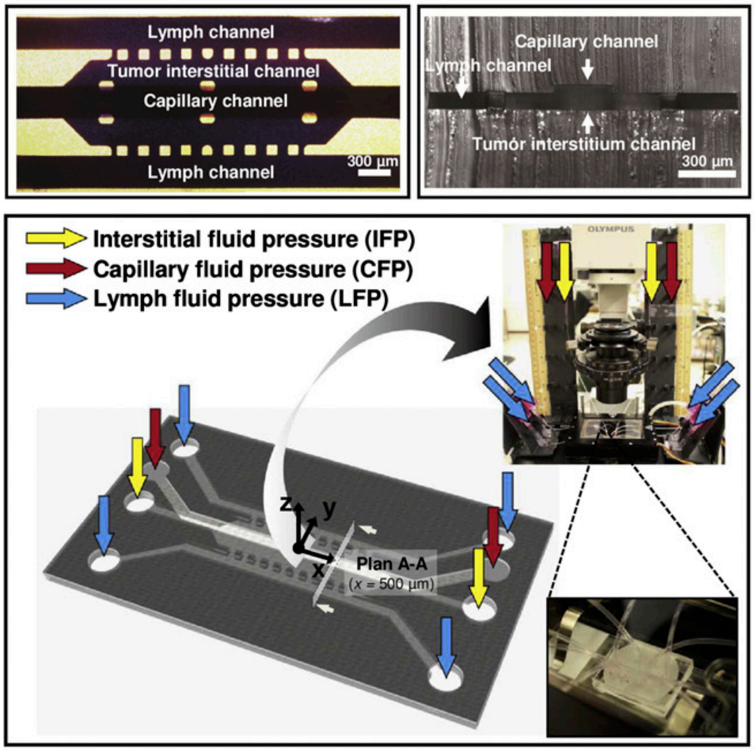

Figure 1.6 Schematic of the tumor-microenvironment-on-chip
(A) Conceptual design: A minimal functional unit of a solid tumor, i.e., a pair of capillary and lymphatic vessels, is mimicked into a 3D microfluidic platform with a 3D structure. The top channel (red arrow) simulates the capillary with endothelium (monolayer of endothelial cells on a nanoporous membrane). Nanoparticles can be introduced along this capillary channel. The bottom layer has a center channel (blue arrow) mimicking a 3D tumor microstructure (i.e., cells in 3D matrix) and two side channels simulating the lymphatics (green). The tumor channel was pressurized to establish the elevated interstitial fluid pressure (IFP) [89].

1.5. Drug Delivery Systems in Cancer Research

Nanomaterials are increasingly used as drug delivery systems for cancer therapy. The use of nanocarriers (preferable in the range of 5-200 nm) displays advantages over conventional drug administration since parameters such as drug efficacy, toxicity, solubility and stability are improved [90]. Extravasation of nanocarriers from the vasculature due to the EPR effect in solid tumors results in targeted delivery of these particles to the tumor area [91]. Although it has been recently shown that nanoparticles are able to extravasate to the tumor area by trans-endothelial pathways (active route), passive extravasation (gaps through endothelial cells) happens with 25% of 100 nm gold nanoparticles [92].

In addition to the formation of a leaky vasculature system, the decrease in pH in the tumor microenvironment is another area explored in tumor-target delivery. Yu et al. [93] explored the resistance of breast cancer to doxorubicin by developing pH-sensitive polymeric microspheres that contained the drug at their core. Microspheres formed by polyethylene glycol-block-poly[2-(diisopropylamino)ethyl methacrylate] and D-a-tocopheryl polyethylene glycol 1000 succinate. Although microspheres were stable under physiological pH, after cellular uptake, doxorubicin was released by pH-triggered dissociation of the particles. Similarly, Lee et al [94] designed pH-responsive microspheres containing aspartic acid imidazole as the hydrophobic group, and ethylene glycol as the hydrophobic group. The microspheres were able to hold up to 28% of doxorubicin. Under acid conditions (below pH 7), the microspheres released gold by protonation and degradation, displaying an increase cell cytotoxicity.

Hydrogel nanoparticles, also known as nanogels, can also be pH-triggered depending on its functional groups. Nanogels present unique advantages such as biocompatibility and reversible deformation [95]. Cai et al [96] designed 250 nm amphiphilic hyaluronan- based conjugates loaded with organoiridium(III) complex. Under reducing environment, the micelles showed rapid dissociation. *In vitro* results demonstrated that iridium(III)-loaded nanogels displayed higher cytotoxicity than the free anticancer drug. *In vivo* results showed accumulation of micelles in the tumor, suggesting a great potential to delivery iridium(III). Raza et al. [97] focused on the development of a pH-responsive FER-8 peptide hydrogel loaded with paclitaxel. In addition to a sustained release of paclitaxel at pH 5.5 for almost one week, intratumoral injection of the nanohydrogel in mice showed a retention of 96 h in the liver tumor site. The growth of the tumor was inhibited at 12 days post-treatment, after a single weekly injection. In addition, no obvious inflammation was seen at the injection site.

Xu et al. [98], on the other hand, encapsulated doxorubicin in nanoparticles composed of polyacrylic acid and amorphous calcium carbonate (inorganic-organic system). Although amorphous calcium carbonate displays high drug loading ability and biocompatibility, when used by itself, it quickly dissolves. The nanogels displayed a size around 60 nm and a drug encapsulation efficiency of 80%. *In vitro* studies demonstrated degradation of the particles at pH 6.6, while in vivo results showed major accumulation of the particles in mouse xenograft models at 24 h, while displaying sustainable cell-killing efficiency at hepatocarcinoma tumors.

Metallic nanoparticles are currently being applied as contrast agents and nanocarriers in cancer treatment [99]. The fabrication of core-shell structured nanoparticles can be applied to the targeted delivery of metallic particles to the tumor area in order to reduce metal toxicity. Han et al. [100] developed a complex 50 nm pH-responsive core-shell nanoparticles displaying a mesoporous silica core (modified with polyethylene glycol) loaded with doxorubicin. The anionic shell of the nanoparticles was composed of a hepatocarcinoma-targeting polymer (galactose-modified poly(allylamine hydrochloride)-citraconic anhydride). At acidic environment (pH 6.5), polyethelyene glycol detached due to acidic hydrolysis, exposing the galactose ligand and, consequently, resulting in high uptake by the hepatocarcinoma cells. Since the endosomes and lysosomes display pH of 5.0, the anionic shell was converted into positive charges, resulting in disassembly and delivery of the drug.

Ellis et al. [101] explored the fabrication of 46 nm gold nanoparticles with multilayer shell of copolymers (poly(oligo(ethylene glycol)methyl ether methacrylate), poly(2-(diisopropyl amino)ethyl methacrylate), and poly(2-(methacryloyloxy)ethyl phosphorylcholine)). Doxorubicin was loaded close to the gold core and, due to the pH-responsive nature of the nanoparticle shell, doxorubicin was then released at pH 6. In a similar approach, Yilmaz et al. [102] developed a 100 nm pH-responsive drug-conjugated glycopolymer-coated gold nanoparticles that were loaded with doxorubicin. The 55 nm gold nanoparticles were tagged with D-mannose methacrylate glycomonomer, responsible for the pH-sensitive response at pH 5.3 and release of doxorubicin in 72 h. The effect of the drug in terms of cell viability was evaluated in four different cell lines (HeLa, A549, SH-SY5Y and Vero cells). Cellular internalization resulted on a display of higher toxicity to cancer cell lines than to the Vero healthy cell line.

1.6. Relevant components

1.6.1. Role of ECM in Breast Cancer

The mammary epithelium is composed of two layers, an inner layer of luminal epithelial cells (apical layer) and an outer layer of myoepithelial cells (basal layer). These two layers are encapsulated with a basement membrane rich in laminin. More than 80% of the breast volume is mammary stroma, which consists of fat tissue, blood vessels, interstitial dense connective tissue and intralobular loose connective tissue [103, 104]. Stromal cells are in contact not just with the basement membrane, but also with the stromal extracellular matrix. The stromal ECM is a dense meshwork composed of collagen types I and III, fibrillar glycoproteins, hyaluronic acid and proteoglycans [105].

Cancer progression in breast tissue is accompanied by ECM remodeling, where an increased deposition of proteoglycans, collagen, and fibronectin, and increased levels of lysyl oxidase-dependent matrix crosslinking are seen [38]. This leads to an increase in stiffness in breast cancer, where the elastic modulus of the tissue ramps from 150 – 400 Pa to ~ 4 kPa [38, 106, 107].

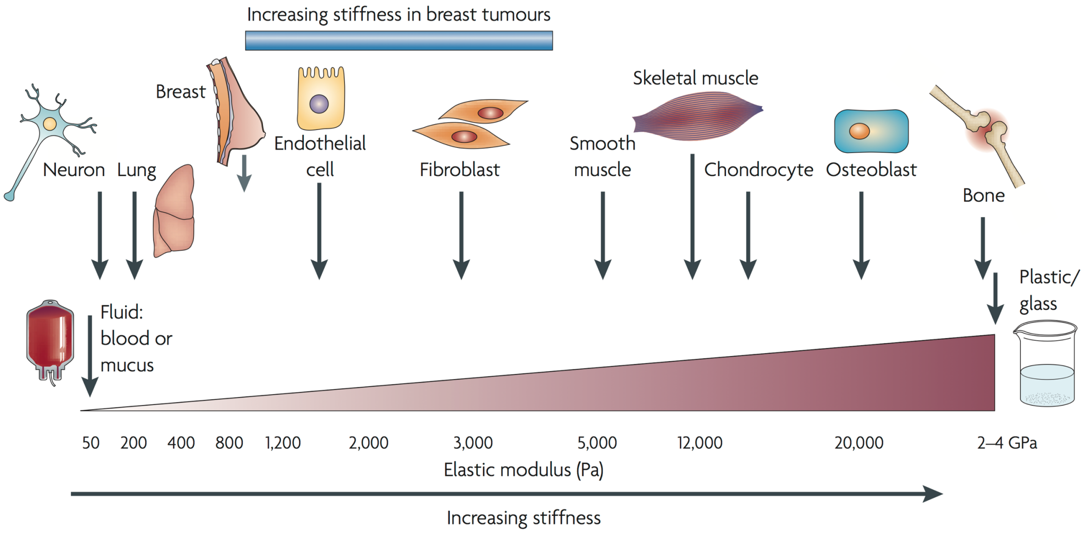

Figure 1.7 Elastic Modulus (Pa) different matrices [58]**.**

1.6.2. Gelatin Methacryloyl

Gelatin Methacryloyl is a gelatin derivative polymer. This hydrogel is usually produced by the reaction of gelatin with methacrylic anhydride [108]. This results in a polymer that contains a large quantity of methacrylamide groups and a small amount of methacrylate groups [109]. Due to the presence of different functional groups in the gelatin backbone, the degree of functionalization of this polymer can be changed based on reactions conditions, such as pH and amount of methacrylate (methacrylic anhydride and glycidyl methacrylate) [110].

GelMA form covalently crosslinked hydrogels by photoinitiated radical polymerization under UV light. The degree of functionalization (or substitution) of GelMA affects its mechanical properties. GelMA hydrogels with high degree of functionalization display high elastic moduli values and low swelling [111]. This illustrates the tunable mechanical properties of this hydrogel. In addition, the presence of the peptide sequence arginine-glycine-aspartic acid (RGD) from its gelatin backbone enhances cell adhesion and proliferation, and a degradation sequence matrix metalloproteinase (MMP) which promotes enzymatic degradation [112]. This hydrogel has shown numerous biomedical applications, ranging from tissue engineering to drug delivery systems and bio-sensing [113–115].

1.6.3. Collagen Type I

Collagen is one of the most abundant proteins found in ECM *in vivo* [116]. Collagen type I is composed of acid-soluble molecules and can be polymerized by changing pH and temperature. Polymerization of collagen happens in two phases: 1) nucleation phase, in which molecular assembly happens and 2) a rapid growth phase, in which cross-linking occurs. The thickness of the fibers formed during polymerization can be increased by decreasing the pH and temperature, and, consequently, prolonging the nucleation phase [116]. Collagen I present low values of Young's modulus (100-300 Pa). In addition, high pore sizes (400 nm to 4.4 µm) can be obtained by tuning the concentration and thickness of the collagen fibers [85, 116].

1.6.4. Microfluidic Devices

Microfluidic devices can be applied in the fabrication of microspheres and nanogels. In the case of microspheres, flow focusing microfluidic devices are used. In these devices, microspheres are produced by using a minimum of two immiscible fluid phases (dispersed phase and continuous) that flow in a cross-junction channel [117]. In the case of water-in-oil systems, the dispersed phase is composed of an aqueous solution, while the continuous phase is composed of an oil solution. The formation of microspheres is created when the shear stress of the oil phase overcomes interfacial tension that keeps the droplets attached to the aqueous region, breaking off from the aqueous phase into droplets [118]. The fabrication of the droplets and their size are dependent on parameters such as flow rate of the two phases, geometry of the microfluidic device, and fluid properties of the continuous and dispersed phases [119]. Two nondimensional numbers (Capillary number and Weber number) govern the droplet formation inside flow focusing devices.

The relationship between interfacial tension and inertial forces is described by the Weber number, according to [118]:

$$We = \frac{\rho U^2 D_h}{\sigma} \tag{1}$$

where ρ, U, D_h correspond to the density of the aqueous solution, velocity of the aqueous solution, and channel hydraulic diameter, respectively. The interfacial tension between the two immiscible fluids is represented by σ.

The Capillary number, on the other hand, shows the ratio between viscous and interfacial tension forces, according to [118]:

$$Ca = \frac{\mu U}{\sigma} \tag{2}$$

where μ and U represent the continuous phase viscosity and mean velocity, respectively.

Three regimes are known to occur during droplet generation: squeezing, dripping, and jetting [120]. The squeezing regime (**Figure 1.8**) occurs when the flow rate and viscosity of the fluids is low (We << 1 and Ca << 1). Droplets are formed due to a build-up in pressure at the cross-junction, in which an aqueous neck is seemed to form in order to minimize surface energy. In the case of the dripping regime (**Figure 1.9**), viscosity of the oil phase is higher than the viscosity of the aqueous phase. A spherical shape is also formed in this case in order to minimize the surface tension. A neck is created by the continuous phase, dragging the aqueous phase to the channel opening. Droplets are created due to Rayleigh-Plateau instability [121], when the viscosity of the oil phase is higher than the interfacial force of the aqueous phase [123]. Lastly, the jetting regime (**Figure 1.10**) occurs when a high flow rate is being used for the aqueous phase (We ~ 1 or greater), and, consequently, inertial forces dominate interfacial tension forces [118]. In this case, a stream of the dispersed phase is created and droplets are formed due to Rayleigh-Plateau instability [121]. The jetting regime also occurs when the flow rate of the continuous phase is high (Ca ~ 1 or greater), resulting on pulling of the aqueous phase by the oil phase due to viscous drag forces (aqueous flow rate is not high enough to overcome interfacial tension forces) [118, 122].

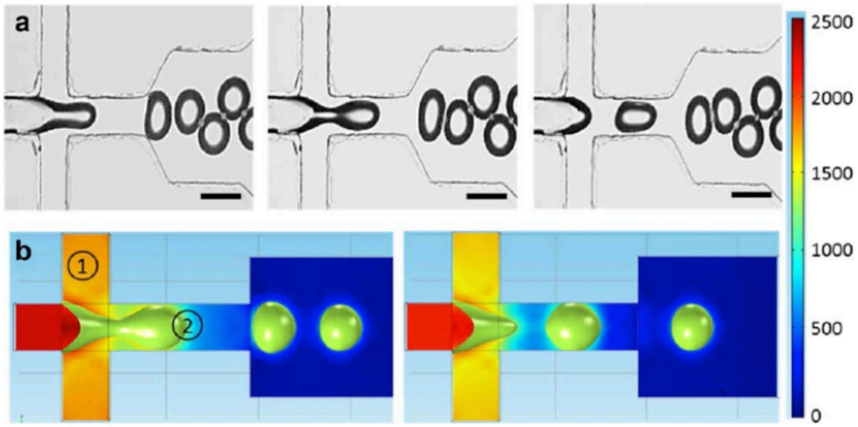

Figure 1.8 Droplet formation by the squeezing regime [122]**.**
Point 1 indicates upstream hydrostatic pressure and point 2 shows pressure after the cross-junction.

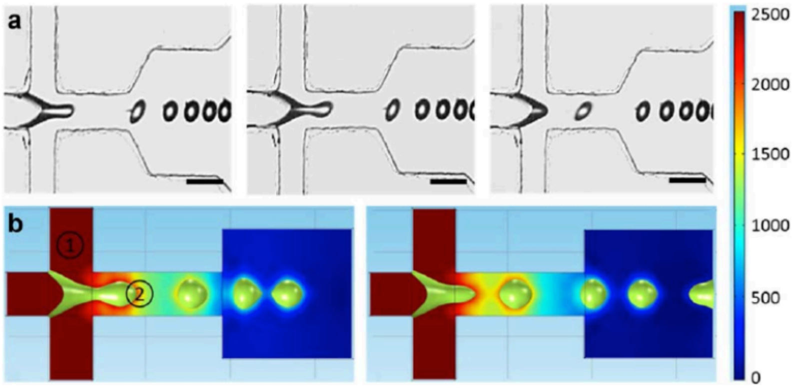

Figure 1.9 Droplet formation by the dripping regime [122].
Point 1 indicates upstream hydrostatic pressure and point 2 shows pressure after the cross-junction.

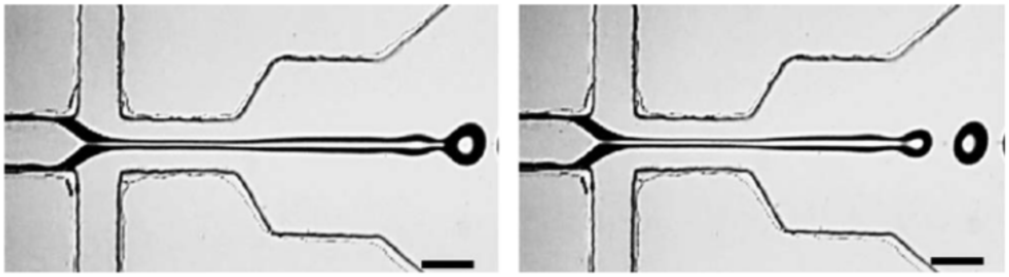

Figure 1.10 Droplet formation by the jetting regime [122].

Flow focusing microfluidic devices can also be used in the production of nanogels. Nanogels are fabricated due to the nanoprecipitation process. At low flow rate of the aqueous phase (solvent in the case of nanogels), this fluid is pressed by the oil phase (nonsolvent in the case of nanogels) until a narrow stream is formed. The nanoprecipitation of the polymeric particles is induced by the interfacial diffusion between the two phases.

1.6.5. Gold Nanoparticles as Radiotherapy Enhancers

Radiation therapy is used in cancer treatment by bombarding the cancer region with ionizing radiation, causing damage in the DNA of the cells. The DNA damage can also be caused by free radicals, generated by the ionization of water and oxygen molecules, and secondary electrons [123, 124]. The disadvantage of this type of treatment relies on the fact that it is non-selective: unwanted damage is also created in the healthy tissue surrounding the tumor.

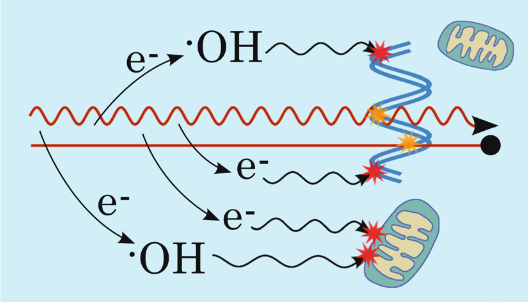

Figure 1.11 Illustration of mechanism of radiation damage.
Both photons (red oscillatory line) and ion radiation (straight line) may directly damage cell DNA or other parts of the cell, such as mitochondria, as well as ionise the medium, thereby producing radicals and other reactive specieis (OH) also as secondary electrons. Secondary electrons can cause direct damage after diffusion (red stars). Secondary electrons may also react with the medium to further increase the number of radicals [124].

Photon-based radiotherapy, such as gamma and X-ray, use photons to effectively ionize biological matter. The drawback of this technique is due to the exponential dose deposition with tissue depth [124]. This means that a significant dose of radiation is delivered to the healthy tissue that is located above the targeted area [125]. Therefore, normally lower-energy radiation delivered from multiple angles around the cancerous area is used, where an overlap of beams focuses in the cancerous tissue [126].

Radiosensitizers can be used to enhance the effect of radiation in tumors by amplifying the radiation dose in the tumor area. When X-rays hit a molecule, several emissions can occur, including scattered photons, photoelectrons, Compton electrons, fluorescence photons and Auger electrons.

When radiation reaches a soft tissue, the photons lose their energy by the Compton effect, where the photon is scattered by an electron losing energy due to the ejection of the electron from the atom [127]. The photoelectric effect, on the other hand, occurs when the radiation wave hits an electron from the inner shell of the atom, ejecting this electron from its orbital with a certain kinetic energy [128]. This process varies with *(Z/E)*^{3}, where *E* is the energy of the incident photon and *Z* is the atomic number of the targeted molecule. The position of the missing electron is occupied by an outer-shell electron, releasing energy as fluorescent photons or Auger electrons [129].

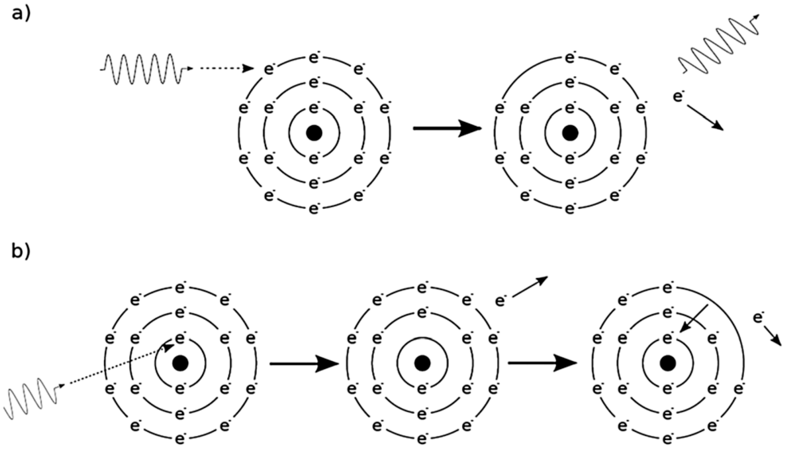

Figure 1.12 Schematic illustration of ionization caused by Compton and Photoelectric Effect a) Compton effect and b) Photoelectric effect [127].

The enhancement of radiation therapy can be achieved by introducing materials with high atomic number. The high atomic number of gold (*Z*=79) compared to soft tissues (*Z*=7.4) can produce an enhancement of 1217 ($79^3/7.4^3$), as illustrated by **Figure 1.13**. The interaction of X-ray radiation with gold nanoparticles is illustrated by **Figure 1.14**.

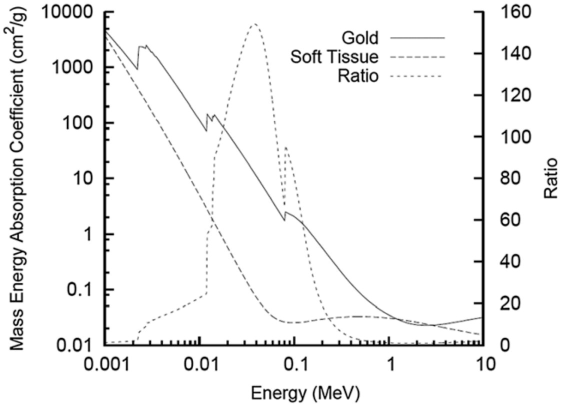

Figure 1.13 Comparison of photon mass energy absorption coefficients for gold and tissue. The ratio of the mass energy absorption coefficients is shown as a function of photon energy [127].

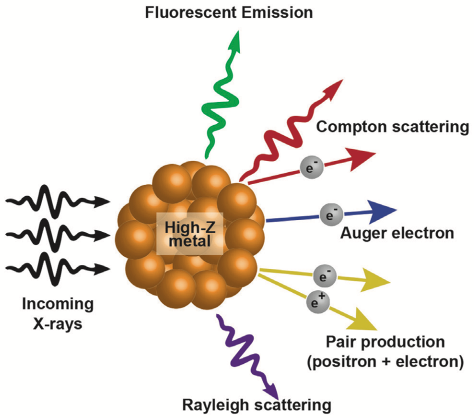

Figure 1.14 Interaction of X-rays with high-Z material nanoparticles [129].

1.7. Thesis Research Objectives

The overall objective of the thesis research is to apply microfluidic devices and biomaterials in the study of cancer. To this end, the objectives can be grouped along four distinct projects.

1.7.1. Research Objective 1

Research Statement: Considering that hydrogels mimicking ECM components have not shown an integration with the tissue mechanical properties, such as stiffness, a hydrogel composite was developed to mimic cancerous and healthy breast tissues. In addition, the impact of stiffness and interstitial pressure on the diffusion of a dye (fluorescein) and 10 nm gold nanoparticles was evaluated.

Methodology: In Chapter 2, a microfluidic device containing three channels was created. The central channel simulated the tumor area, while lateral channels mimicked capillary vessels. A hydrogel composite was developed by combining GelMA and Collagen type I. By changing the ratio of these two materials, hydrogels with tunable stiffness were produced. The hydrogel composite was injected in the central channel of the microfluidic device, while fluorescein sodium salt and fluorescently labeled gold nanoparticles were introduced to the lateral channels. The movement of the dye and the gold particles through the hydrogel layer was tracked by fluorescence in a Laser Scanning Microscope (LSM). Additionally, pressurization was introduced to the central channel in order to mimic interstitial pressure.

Expected Outcome: The results are expected to clarify the impact of interstitial pressure and stiffness on the transport of fluorescein dye (simulating a chemotherapy drug) and gold nanoparticles in a hydrogel composite. This was done by quantification of the diffusion coefficients of the species. This is a new contribution to the state of the art, and it is crucial for the understanding of the delivery of species in a 3D environment.

1.7.2. Research Objective 2

Research Statement: The investigation of the impact of surface charge of gold nanoparticles on the diffusion and cellular uptake of an ECM-mimicking hydrogel composite was performed. Considering that many studies have shown that positive gold nanoparticles display the highest cellular uptake, it was decided to investigate their diffusion in a microfluidic device. In addition, diffusion of neutral and negative particles was also investigated to demonstrate that cellular uptake should not be the only parameter analyzed in drug delivery.

Methodology: In Chapter 3, the same microfluidic device (described in Chapter 2) was used in the tracking of diffusion of gold nanoparticles with different surface charges (neutral, positive, and negative). Gold nanoparticles moved from the lateral channel of the microfluidic device, through the hydrogel layer. It was observed that neutral particles diffused faster than negative and positive particles. In addition, cellular uptake of these particles was investigated in a 3D *in vitro* breast cancer model created by encapsulating breast cancer cells in the hydrogel composite developed previously. Quantitative cellular uptake measurements were performed by inductively coupled plasma mass spectrometry (ICP-MS).

Expected Outcome: The goal is to detect a correlation between diffusion and cellular uptake. This is the first time that these two parameters are analyzed together. In addition, the effect of these two parameters are quantified. While numerous studies in the literature have investigated the cellular uptake of gold nanoparticles with different charges and sizes, diffusion had not been yet taken into account.

1.7.3. Research Objective 3

Research Statement: The development of pH-responsive hydrogels to be applied as drug delivery systems to cancer was carried out. Considering that Gelatin Methacryloyl has shown excellent biocompatibility due to its gelatin backbone, two types of uniform microspheres of pH-responsive GelMA hydrogels were created using a flow focusing microfluidic device.

Methodology: In Chapter 4, two synthetic routes were taken to create two pH-responsive GelMA (polymers A and B). Microspheres (40 μm) were fabricated using a flow focusing microfluidic device. Investigation of swelling behavior of particles was performed to illustrate and quantify their pH-responsive property.

Expected Outcome: GelMA has been extensively used as a biomaterial. However, the advantage of being a gelatin derivative in terms of functional groups has not yet been explored. In this work, the synthesis of GelMA hydrogels was tuned towards pH-responsive polymers, opening a new line of applications for this hydrogel as drug-delivery systems.

1.7.4. Research Objective 4

Research Statement: The acidic pH-responsive hydrogel (from Chapter 4) was applied in the fabrication of nanogels loaded with gold nanoparticles in a flow focusing microfluidic device and to demonstrate good loading of gold inside the nanogels for future applications in cancer extravasation.

Methodology: In Chapter 5, GNP@GelMA nanogels (~70 nm) from polymer A were produced using a flow focusing microfluidic device, displaying a considerable amount of gold in the nanogels. Gold nanoparticles were mixed in the hydrogel solution prior to the injection in the microfluidic device.

Expected Outcome: While encapsulation of individual nanoparticles in hydrogels has been presented in the literature, here the sizes of the particles are proposed to be explored differently. The size of GelMA nanogels is tuned towards efficient extravasation, while the size of the GNPs was selected in order to enhance diffusion. Therefore, this system of GNP@GelMA nanogels is expected to show promising applications in the field of targeted delivery.

Finally, chapter 6 presents a discussion and conclusions for each chapter, as well as potential research avenues for future work. Chapter 7 summarizes the dissemination of results and other academic activities performed such as research presentations, review papers, and papers from collaborations. Appendices A and B present the supplementary information of Chapter 2 and 3, respectively.

Chapter 2 Collagen type I-Gelatin Methacryloyl Composites: Mimicking the Tumor Microenvironment in a Microfluidic Device [b]

Karolina P. Valente [1], Sapanbir S. Thind [2], Mohsen Akbari [1], Afzal Suleman [1], Alexandre Brolo [2*]

[1] Department of Mechanical Engineering, University of Victoria, Victoria, BC, Canada.
[2] Department of Chemistry, University of Victoria, Victoria, BC, Canada.

Key words:

Tumor Microenvironment, Microfluidics, Hydrogel, Breast Cancer, Gold Nanoparticles.

Author contributions

Karolina P. Valente performed most of experimental work, design, analysis, and wrote the manuscript draft. Sapanbir S. Thind. helped to perform Scanning Electron Microscopy images. Mohsen Akbari provided feedback on the manuscript. Afzal Suleman and Alexandre. Brolo provided feedback on the experimental analysis and edited the manuscript.

---

[b] The following chapter is from: Karolina P. Valente, Sapanbir S. Thind, Mohsen Akbari, Afzal Suleman, Alexandre Brolo. **Collagen Type I-Gelatin Methacryloyl Composites: Mimicking the Tumor Microenvironment.** *ACS Biomater. Sci. Eng.*, 2019, 5, 2887-2898.

2.1. Abstract

Therapeutic drugs can penetrate tissues by diffusion and advection. In a healthy tissue, the interstitial fluid is composed of an influx of nutrients and oxygen from blood vessels. In the case of cancerous tissue, the interstitial fluid is poorly drained due to the lack of lymphatic vasculature, resulting in an increase in interstitial pressure. Furthermore, cancer cells invade a healthy tissue by pressing and pushing the surrounding environment, creating an increase in pressure inside the tumor area. This results in a large differential pressure between the tumor and the healthy tissue, leading to an increase of extracellular matrix (ECM) stiffness. Due to high interstitial pressure in addition to matrix stiffening, penetration and distribution of systemic therapies are limited to diffusion, decreasing the efficacy of cancer treatment. This work reports on the development of a microfluidic system that mimics *in vitro* healthy and cancerous microenvironments using collagen I and gelatin methacryloyl composite hydrogels. The microfluidic device developed here contains a simplistic design with a central chamber and two lateral channels. In the central chamber, hydrogel composites were used to mimic the ECM, while lateral channels simulated capillary vessels. The transport of fluorescein sodium salt and fluorescently labeled gold nanoparticles from capillary-mimicking channels through the ECM-mimicking hydrogel was explored by tracking fluorescence. By tuning the hydrogel composition and concentration, the impact of the tumor microenvironment properties on the transport of those species was evaluated. In addition, breast cancer MCF-7 cells were embedded in the hydrogel composites, displaying the formation of 3D clusters with high viability and, consequently, the development of an *in vitro* tumor model.

2.2. Introduction

The growth of cancerous cells alters the tissue microenvironment, inducing extracellular matrix remodeling [36]. While uncontrollable cell growth is known as one of the primary manifestations of cancer, tumor growth also displays other hallmarks, such as angiogenesis, high interstitial pressure, ECM stiffening, and metastasis [130–132]. As illustrated in **Figure 2.1**, the development of cancer results in an increase of intratumoral pressure caused by the proliferation of cancer cells inside a confined healthy tissue space that presses normal cells, ECM and capillary vessels [43]. This ‘stressful’ environment leads to an increase in colloidal osmotic pressure in the tumor interstitium, resulting in a net outward pressure from the tumor area to the surroundings (up to 18 mmHg) [46]. Rapid cancer proliferation, combined with a disorganized vascularization system and an increased fluid pressure, results in a build-up of toxins and waste products. It also initiates the formation of hypoxic regions, where the lack of oxygenation results on a shift from metabolic oxidative pathways to glycolysis and, consequently, acidification of the medium [48]. Cancer progression is also accompanied by ECM remodeling and stiffening. For example, in the case of breast cancer, an increased deposition of proteoglycans, collagen, fibronectin and high levels lysyl oxidase-dependent matrix crosslinking is related to a ramping of tissue elastic modulus from 150-400 Pa to values higher than 4 kPa [106, 107].

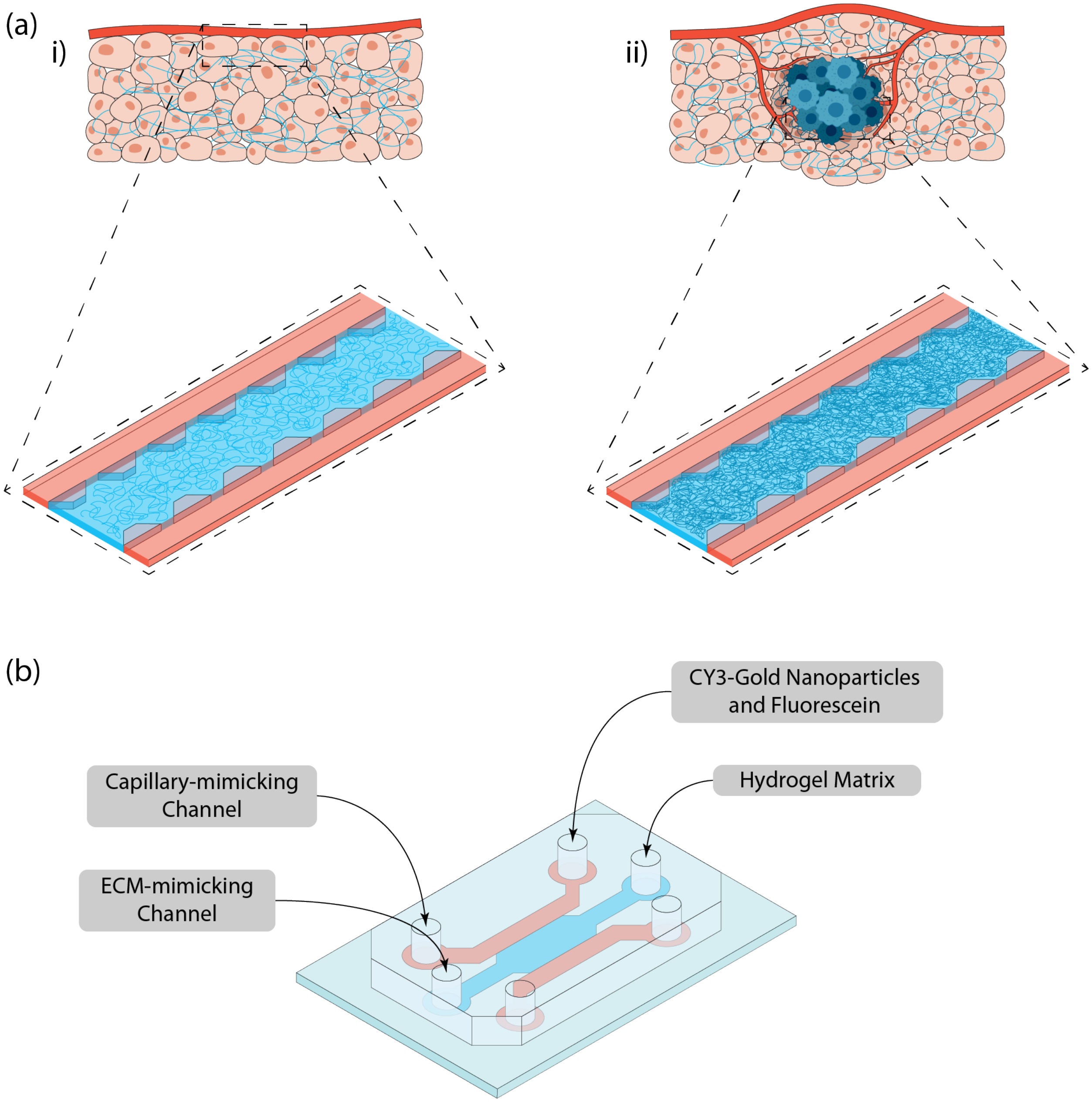

Figure 2.1 Mimicking ECM i*n vitro* using a microfluidic device
Healthy tissue displays organized internal structure and soft ECM (represented by loosely packed fibers on i), while tumor region exhibits disorganized vessel network and ECM stiffening (represented by closely packed fibers on ii) (a). Healthy and cancerous environments were simulated inside a microfluidic device with the aid of hydrogel composites containing Collagen I and Gelatin Methacryloyl. The microfluidic device consisted of a central ECM-mimicking channel, where hydrogel mixtures were injected, and two capillary-mimicking lateral channels (b). A solution containing CY3-GNP and fluorescein sodium salt was injected in the lateral channels in order to study species transport within hydrogel matrix.

Chemotherapy presents one of the most common ways to treat cancer. However, systemic delivery of chemotherapeutic drugs is hindered by the tumor microenvironment [41]. The contribution of advection to the penetration of the therapeutic drug becomes minimal due to elevated interstitial fluid pressure within the tumor region [45]. Consequently, diffusive transport dominates therapeutic drug delivery [133]. Radiation therapy is another well-used method in the treatment of cancer (around 50% of the cases), in which the cancer is bombarded with ionizing radiation which causes DNA damage [124]. Radiosensitizers, such as gold nanoparticles (GNP), can be used to enhance radiation effect in tumors based on the contrast between the electronic properties of gold and soft tissues [127]. The synthetic versatility of GNP permits their fabrication in different sizes, shapes and morphologies [134–136]. Surface modification allows the conjugation of GNP with cytotoxic drugs, extending the application of these particles to drug delivery [137–139].

Although different therapeutic cancer treatments are available, only around 5% of drugs and drug delivery agents can actually be delivered to the tumor area after systemic administration due to factors such as the tumor microenvironment [140, 141]. Moreover, despite the fact that the leaky vasculature seen in solid tumors can help nanoparticles to move from capillary vessels towards the cancerous area through the gap between the endothelial cells, further movement between ECM and dense interstitial space is diffusion-dominated [69, 142].

The study of the transport of molecules and particles in a system that recreates the key features of the tumor microenvironment is then important for the development of novel drug-delivery platforms. While most *in vitro* studies involving GNP transport have been performed in cancer cell monolayers, the integration of nanoparticles in a microfluidic system allows the study of diffusion in a 3D *in vitro* model. The micrometer dimensions of microfluidic channels limit the amount of reagents, reducing equipment and sample costs. In addition, small dimensions combined with a precise spatial and temporal control of nutrients allows the replication of human tissues *in vitro* [37]. Therefore, an architectural microfluidic design combined with the structural environment provided by hydrogels should allow the investigation of fluid transport in a model that resembles more closely the tumor microenvironment than a cancer cell monolayer.

In this study, a simplistic microfluidic device was developed. The device, shown in **Figure 2.1**, contained three channels: an ECM-mimicking central channel and two capillary-mimicking lateral channels. The influence of key features of tissue-mimicking microenvironments (healthy and cancerous), such as interstitial pressure and ECM stiffness, in the transport of molecules and gold nanoparticles were assessed. *In vitro* ECM was mimicked by tuning the composition of a hydrogel composite formed by collagen type I and gelatin methacryloyl. To the best of our knowledge, this is the first example of healthy and cancerous tissues simulation (using a collagen I-GelMA tunable composite) in a simplistic microfluidic device that assessed the impact of the tissue microenvironment in the delivery of nanoparticles and small molecules. In addition, we also investigated the viability and morphology of tumorigenic human breast cancer MCF-7 cells encapsulated in the hydrogel composites, allowing the creation of *in vitro* microtumors.

2.3. Materials and Methods

2.3.1. Materials

Gelatin Methacryloyl (Bloom 300, ≥80% degree of substitution), Gelatin from Porcine Skin (Bloom 300), 2-Hydroxy-4′-(2-hydroxyethoxy)-2-methylpropiophenone (Irgacure 2959) (98%), Glutaraldehyde solution (grade I, 70% in water), (3-Aminopropyl)triethoxysilane (APTES), 3-(trimethoxysilyl)propyl methacrylate (98%) (TMSPMA), Fluorescein sodium salt, 2,4,6,-Trinitrobenzenesulfonic acid solution 5% (w/v) in water (TNBS), Phosphate Buffered Saline (PBS) and hexamethyldisilazane (HMDS) (≥ 99%) were purchased from Sigma-Aldrich. CULTREX® 3D Culture Matrix Rat Collagen I was purchased from Trevigen at a concentration of 5 mg mL^{-1}. Sodium dodecyl sulfate, sodium bicarbonate and glycine were purchased from Bio Basic Canada Inc. Stainless steel 440c (SS) and silicon nitride (Si_3N_4) indenters were purchased from Bearings Canada. Fluorescent Polystyrene (PS) particles (100 nm, aqueous suspension of 2.5% (w/v)) containing a red fluorescent emission were purchased from Magsphere Inc., while 10 nm CY3-labeled gold nanoparticles (CY3-GNP) were obtained from Nanocs (concentration 0.05% (w/v) based on gold). P-type boron silicon wafers measurement 76.2 mm of diameter were purchased from Silicon Materials Inc. Permanent Epoxy Resist SU-8 100 and SU-8 Developer were purchased from MicroChem Corporation. Sylgard 184 Silicone Elastomer kit was obtained from Dow Corning Corporation. Coverslip metallic cell chamber for live-cell microscopy was purchased from Aireka Cells. Collagenase type II was obtained from Worthington Biochemical Corporation at a concentration of 230 U mg^{-1}. MCF-7 cells (HTB-22) were obtained from Facility of Biomolecular Sample Preparation at University of Victoria. Dulbecco's modified eagle's medium (DMEM), fetal bovine serum (FBS), penicillin-streptomycin, 10X PrestoBlue cell viability reagent and LIVE/DEAD™ viability/cytotoxicity kit for mammalian cells were purchased from ThermoFisher Scientific. DAPI staining solution and phalloidin-iFluor 488 reagent were obtained from Abcam.

2.3.2. Hydrogel Preparation

A solution containing 15% (w/v) GelMA was prepared in 1% (w/v) Irgacure 2959 in 1x PBS. Additionally, a solution of 4.0 mg mL^{-1} of Collagen Type I CULTREX® was prepared using the required amounts of 1M NaOH, 10x PBS and deionized water.

In order to simulate the healthy ECM conditions, 25% (v/v) of GelMA solution was mixed with 75% (v/v) Collagen I to a final concentration of 3.0 mg mL^{-1} Collagen I and 3.75% GelMA (3 Coll I-3.75 GelMA) for soft ECM. For the case of cancerous-mimicking ECM, 75% (v/v) of GelMA solution was mixed with 25% (v/v) Collagen I sample to a final concentration of 1.0 mg mL^{-1} Collagen I and 11.25% GelMA (1 Coll I-11.25 GelMA). The volumes of each respective component were mixed to form a homogeneous hydrogel mixture and the final pH was adjusted to 7 by adding required amounts of 1M NaOH.

A volume of 10 μL of the hydrogel samples were pipetted in spacer created by two glass slides (thickness of 400 μm) attached to the cover of a petri dish. A modified coverslip was then deposited on top of the gel, supported by the glass slides. TMSPMA-modified and APTES-modified cover slips were used during the fabrication of stiff and soft hydrogel composites, respectively, and detailed information can be found in Appendix A. Collagen I-GelMA composite hydrogels were initially crosslinked under UV light (365 nm and 6.3 mW cm^{-2}) for 4 min and, consecutively, moved to an incubator at 37 ˚C for 30 min, in order to polymerize collagen I.

2.3.3. Hydrogel Characterization

Hydrogel morphology, porosity, and surface charge were all characterized using standard methods (scanning electron microscopy, gravimetric methods and zeta potential measurements). The details of these techniques are provided as Appendix A.

Characterization of swelling ratio was performed by producing a hydrogel pellet, as described previously, and removing the excess of PBS from the surface of the hydrogel using a paper tissue. After recording the mass of the swollen hydrogel, the samples were then frozen at -80 ˚C, followed by lyophilization. The mass of the lyophilized hydrogels was measured and compared with swollen masses. The swelling ratio was calculated as the ratio of swollen hydrogel mass to the mass of lyophilized hydrogel. Five samples were prepared for each hydrogel composition.

Enzymatic degradation properties of the different hydrogels were determined by incubating hydrogel samples in DPBS containing 2.5 U mL^{-1} of collagenase type II at 37 ˚C. At predetermined time points, samples were removed from collagenase type II solution, washed with deionized water, frozen at -80 ˚C and lyophilized. The percentage of degradation (D%) was obtained by relating the mass of the samples at each time (W_t) with the mass at time zero (initial dry weight = W_0) according to the following equation:

$$D(\%) = \left(\frac{W_0 - W_t}{W_0}\right) \times 100\% \qquad (3)$$

The elastic modulus of each hydrogel pellet was determined by indentation method [143, 144]. Hydrogel pellets with 400 µm of height were prepared on the surface-modified cover slips, as described previously. After polymerization, hydrogel pellets were stained for 1 h with a 50 µM fluorescein sodium salt solution prepared in 1x PBS. After staining, the pellets were rinsed three times with deionized water and inserted on a metallic cell chamber. On this chamber, 2 mL of a solution containing fluorescent PS particles diluted in 1x PBS were deposited on top of the hydrogel pellets. The assembly was then moved to the laser scanning microscope (LSM 880 Zeiss) and left undisturbed for 3 h, to allow deposition of fluorescent particles to the hydrogel surface.

The deposition of the PS particles on the surface of the hydrogel was verified on the LSM. Before addition of the indenter to the surface of the hydrogel, the heights of the hydrogel samples were measured under the microscope. For these measurements, Z-stack images (layer thickness of 2 µm) were obtained using 10x objective lens (EC Plan-Neofluar 10x/0.30 M27) and two excitation sources (488 nm and 543 nm). The 488 nm Argon laser was used to excite fluorescein molecules embedded in the hydrogel layer (emission 490-540 nm), while 543 nm Helium-Neon laser excited fluorescent PS particles (emission 550-700 nm). Z-step displacement of the focal plane was corrected using refractive index of water. The determination of the hydrogel height was performed by calculating the derivative of fluorescence intensity profile for each sample measurement [145].

After height (h) determination, an indenter was carefully positioned on top of the hydrogel pellet. Two different types of indenters were used during the measurements. For stiff hydrogel, a 3/16" spherical SS 440C indenter was used. For soft gels, a 1/32" spherical Si_3N_4 indenter was used. The deformation caused by the indenter in the surface of the hydrogel was measured by capturing images in the Z-stack mode (layer thickness of 2 μm) on LSM, in a similar way as described previously for height determination. In the case of the stainless-steel indenter, tile scan mode was used in addition to z-stack in order to capture the entire deformation on top of the hydrogel. Experiments were repeated five times for each type of hydrogel composition using newly prepared pellets. All measurements were performed at room temperature (25 ± 2 °C).

To determine the indentation depth (δ) performed by the indenter in the surface of each gel, Zen 2.3 (Blue edition) software was used, where cross-section images (XZ and YZ) were obtained in the axis of symmetry of the gel indented surface. Details on the calculation of elastic modulus can be found in Appendix A.

2.3.4. Breast cancer cells encapsulated in hydrogel composites

MCF-7 cells were maintained in Dulbecco's modified Eagle's medium (DMEM) supplemented with 10% fetal bovine serum and 1% penicillin-streptomycin in a 5% CO_2 incubator at 37 °C. Media was changed every 2 days and cells were passaged when 80% confluent.

Cell encapsulation in the hydrogel samples were prepared by adding breast cancer cells to the hydrogel mixture prior crosslinking, at a final concentration of 1 x 10^4 cells per hydrogel pellet (10 µL sample). Characterization of cell viability in the hydrogel samples was performed using PrestoBlue assay. A 1X solution of PrestoBlue was prepared by diluting PrestoBlue with DMEM and added to each well containing cell encapsulated hydrogel samples. Samples were incubated for 1 h at 37 ˚C. After incubation 200 µL of the supernatant was obtained to measure fluorescence signal at 560 nm of excitation and 590 nm emission using a plate reader, according to the manufacturer's instructions. Fluorescence signal of culture medium containing PrestoBlue in absence of cells was also measured to be used as background control. Five samples were prepared for each hydrogel concentration.

In order to visualize cell viability, hydrogel samples were stained with LIVE/DEAD™ at a concentration of 2 µM for calcein-AM and 4 µM for ethidium homodimer-1. LIVE/DEAD™ solution was prepared in PBS and incubated with hydrogel samples for 1 h at 37 ˚C. Fluorescent confocal images were obtained using LSM Zeiss 880 at 488 nm excitation and 515-540 nm emission for calcein-AM, and at 543 nm excitation and 560-650 nm emission for ethidium homodimer-1. To visualize cell nuclei and actin filaments, DAPI and phalloidin-iFluor 488 staining solutions were used. DAPI was excited at 360 nm and fluorescence signal was collected at 400-500 nm. Labelling of actin filaments was imaged at excitation of 488 nm and emission of 500-600 nm.

2.3.5. Fabrication of a tumor microenvironment-on-a-chip

A microfluidic device was fabricated using standard photolithography (see Appendix A for details) to allow transport measurements in a mimic ECM environment. The microfluidic design, shown in **Figure 2.1**, was composed of two identical lateral channels (width of 1000 µm) and a central channel (width in the range of 600 – 800 μm and length of 2.5 mm). Lateral channels with width of 1000 μm were selected in order to guarantee a constant concentration of GNP and dye during the diffusion process. Although the defined width of lateral channels was larger than actual capillary vessels, the selection of this dimension allowed the determination of diffusion coefficients for the species while using Fick's second law as a fitting model.

Hydrogel composites with tunable stiffness were injected in the central channel of the microfluidic device. After hydrogel crosslinking, the solution in the central channel became a gel. Consequently, the lateral channels were used during injection of a solution containing gold nanoparticles and fluorescein, and transport of the species was analyzed from the lateral channels through the hydrogel contained in the central channel. Trapezoidal posts between the central and lateral channels were created with 100 μm gaps (Appendix A), allowing the contact between the solution in the lateral channel and the hydrogel, while avoiding leakage of the gel from the central chamber towards the capillary-mimicking channels.

2.3.6. Transport of GNP on the microfluidic device

Hydrogel mixtures were injected inside the central channel, as illustrated in **Figure 2.1**, followed by polymerization by UV-light and incubation at 37 °C. After incubation, the microfluidic device was moved to the LSM and positioned correctly. The same excitation and emission wavelengths described previously for the indentation measurements were used. A confocal image was collected before the addition of any solution in the capillary-mimicking channels, in order to verify the presence of a black background from the hydrogel (no emission).

For the diffusion experiments, 10 μL of a solution containing CY3-GNP and 10 μM aqueous solution of fluorescein sodium salt was injected in the capillary channel. Timer was started immediately after injection of this solution in the lateral channel. Confocal images were taken using line scan mode, where each frame 1470 µm x 1470 µm took 3 s to be collected (1024 x 1024 pixels). Images were taken every 3 min for 60 min in total. A humidity chamber was adapted on top of the LSM platform, in order to keep samples from drying. For pressure-driven experiments, hydrostatic pressures of 3 mmHg and 18 mmHg were added to the inlet and outlet ports of the lateral and central channels, respectively. When hydrostatic pressure was added to the inlet and outlet ports of the central channel containing hydrogel-mimicking ECM, pressure was allowed to normalize throughout the hydrogel matrix for 30 minutes, prior to the injection of CY3-GNP and fluorescein dye in the lateral channel. All experiments were performed at room temperature. Information regarding fitting of experimental data to obtain diffusion coefficients can be found in Appendix A.

2.4. Results and Discussion

2.4.1. Hydrogel composite characterization

Hydrogels are three-dimensional polymeric networks that display hydrophilic character and, consequently have the ability to absorb a considerable amount of water [146]. Due to this swelling behavior, hydrogels resembles *in vivo* tissues and have been used to simulate *in vitro* ECM [147]. Here, we aimed to compare the applicability of Collagen type I (Coll I) and Gelatin Methacryloyl hydrogels in the mimicking of healthy and cancerous *in vitro* ECM. Two Coll I-GelMA composites were developed: 3 Coll I-3.75 GelMA (concentrations of Coll I and GelMA were 3.0 mg mL^{-1} and 3.75% (w/v), respectively), and 1 Coll I-11.25 GelMA (concentrations of Coll I and GelMA 1 mg mL^{-1} and 11.25% (w/v), respectively).

GelMA is a light-activated crosslinked hydrogel originated from gelatin. This semi-synthetic hydrogel is composed of a gelatin backbone with methacrylamide and methacrylate groups. GelMA can be easily synthesized at low cost and presents excellent biocompatibility due to abundant presence of arginine-glycine-aspartic acid (RGD) sequences in gelatin [148, 149]. Its porous morphology is illustrated in **Figure 2.2** that presents scanning electron micrographs of the hydrogels used in this work. Substitution of amino groups by methacryloyl can be quantified by TNBS assay. TNBS assay determines the degree of substitution of GelMA hydrogels by quantifying the amount of free amino groups in gelatin, GelMA and glycine samples. Detailed information regarding this assay can be found in Appendix A. GelMA demonstrated a high degree of substitution of 85.7 ± 1.3%.

Collagen is one of the most abundant proteins found in ECM, consisting of one-third of the total protein amount present in the body. Therefore, the combination of this hydrogel with GelMA allows a more realistic *in vitro* ECM [150]. Although there are many types of collagen, types I, II and III correspond to 80-90% of the total *in vivo* collagen [151]. Collagen type I is composed of acid-soluble collagen molecules that undergo polymerization under neutral pH and temperature of 37 °C. Collagen polymerization is accompanied by two phases: nucleation (molecular assembly) and rapid growth (crosslinking phase), resulting on fibrils, as illustrated in **Figure 2.2** [116].

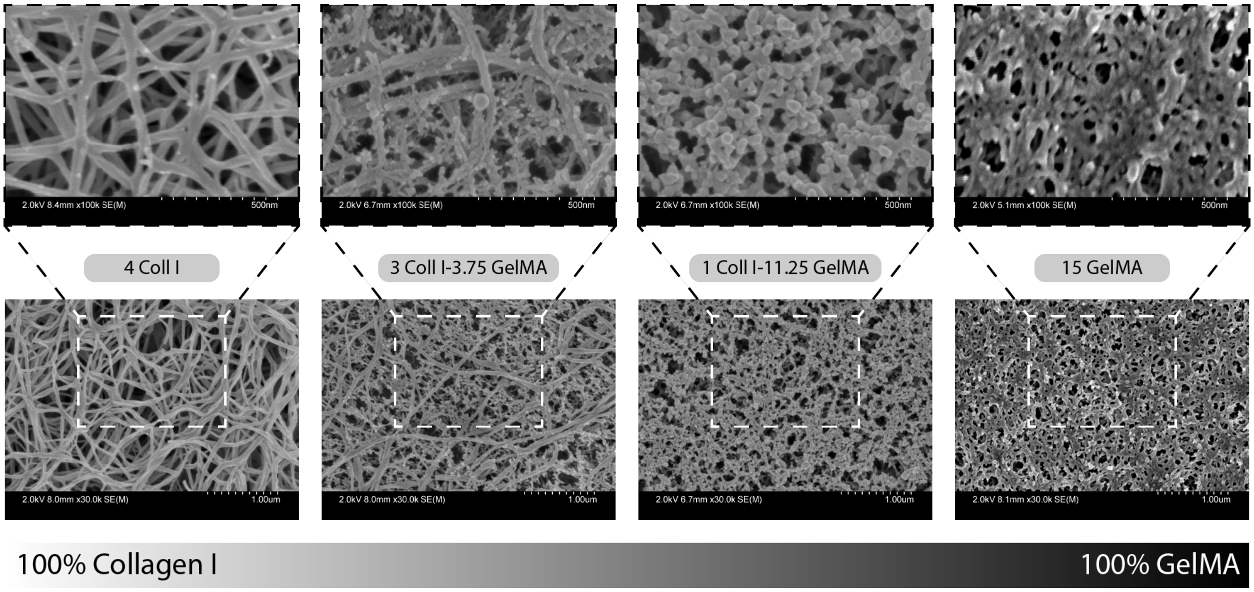

Figure 2.2 SEM images of Hydrogel Samples
4.0 mg mL^{-1} Collagen I (4 Coll I) was mixed 15% (w/v) Gelatin Methacryloyl (15 GelMA) in order to produce two hydrogel composites. Properties of the composites indicated suitability of 3.0 mg mL^{-1} Collagen I and 3.75% (w/v) GelMA (3 Coll I-3.75 GelMA) to mimic healthy ECM, while 1.0 mg mL^{-1} Collagen I and 11.25% (w/v) GelMA (1 Coll I-11.25 GelMA) simulated cancerous ECM. Scale bars of 1.0 μm for bottom images and 500 nm for top images were used.

When GelMA and collagen I were combined, it resulted in composites with different morphologies. **Figure 2.2** shows that while 3 Coll I-3.75 GelMA samples is a composite with both fibrous and porous morphology, 1 Coll I-11.25 GelMA exhibited only a porous morphology which was similar to the structure seen for pure GelMA (15% (w/v)). Hydrogel composites were also characterized according to their swelling behavior (see experimental details in Appendix A), in order to confirm the formation of gel samples and to verify the effect of composition on hydrogel swelling. **Figure 2.3(a)** shows that the composites (3 Coll I-3.75 GelMA and 1 Coll I-11.25 GelMA) present decreased swelling behavior relative to pure GelMA. A high degree of substitution of amine groups by methacryloyl combined with high concentrations of GelMA and photoinitiator resulted in dense hydrogels. A dense meshwork decreases the capability of the polymer to absorb water [152]. The addition of collagen I to the GelMA samples resulted in a decrease of swelling ratio (22.33 ± 0.33 for 3 Coll I-3.75 GelMA and 8.86 ± 0.14 for 1 Coll I-11.25 GelMA). Since collagen type I samples display no swelling behavior, the addition of this component to GelMA produced a more rigid composite than pure GelMA, resulting in a decrease in swelling ratio [153].

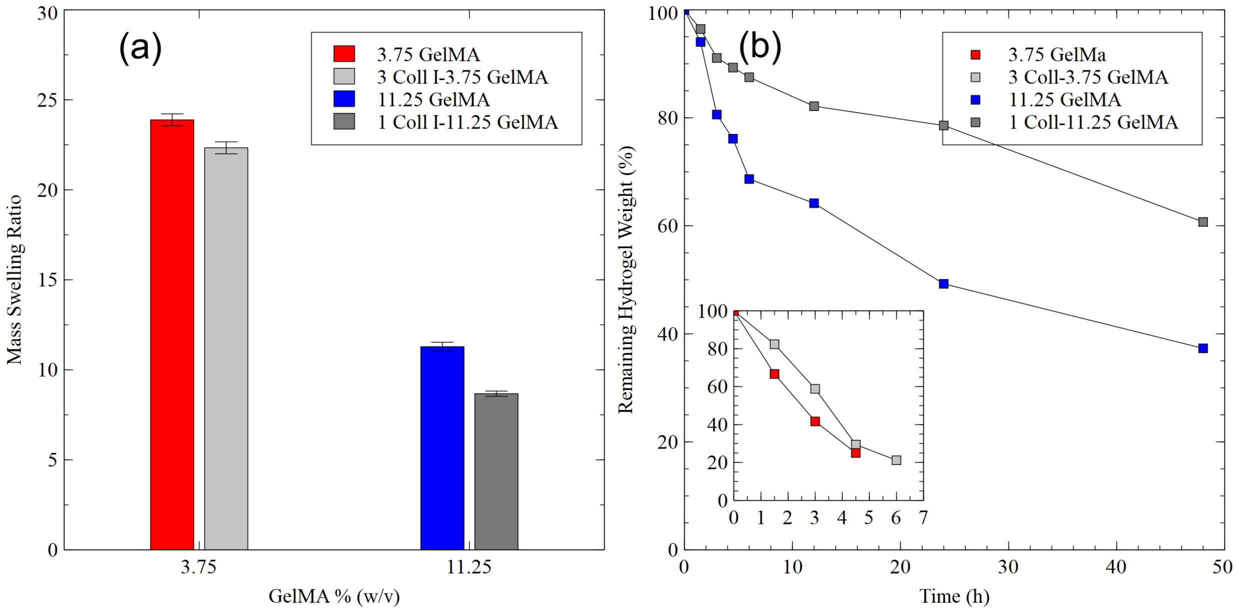

Figure 2.3 Characterization of Hydrogel Composites
(a) Mass swelling ratio of GelMA samples and hydrogel composites. GelMA hydrogels (red and blue bars) exhibited higher swelling behavior compared to hydrogel composites (light and dark grey bars). Five samples were analyzed for each hydrogel concentration. Scale bars represent one standard deviation. (b) Degradation of hydrogels in presence of collagenase type II. Addition of collagen type I slowed the degradation of hydrogel composites. Three samples were analyzed for each hydrogel concentration in each time step.

Degradation tests assess the long-term stability of the hydrogel samples and evaluate the suitability of the hydrogel in cell culture applications. To evaluate degradation, hydrogel samples were incubated in 2.5 U mL^{-1} collagenase type II solution. As illustrated by **Figure 2.3(b)**, the degradation rate decreased with the increase of GelMA concentration in the samples. Furthermore, the addition of collagen I to the GelMA samples resulted in a slower degradation of the hydrogel composites.

ECM components, such as hyaluronic acid and proteoglycans, are negatively charged molecules responsible for attracting counter-ions and water molecules [154]. On the other hand, collagen fibers display positive charge at neutral pH [155]. Since the diffusion of particles in ECM-mimicking hydrogels can be influenced by the matrix charge, zeta potential measurements were performed for all hydrogel samples and CY3-GNP and the results are presented in **Table 2** [85]. While collagen I displayed a positive surface charge (6.6 ± 0.3 mV), hydrogel composites and CY3-GNP were negatively charged (-6.0 ± 0.3 mV for 3 Coll I-3.75 GelMA, -10.7 ± 0.4 mV for 1 Coll I-11.25 GelMA, and -29.8 ± 1.4 mV for CY3-GNP). In order to mimic ECM, a matrix has to be composed of both negatively and positively charged parts with a net negative charge [156]. In addition, fluorescein sodium salt displays negative charge after dissociation in solution. Since the combination of collagen I and GelMA resulted in a negatively charged composite, the interactions between CY3-GNP and the hydrogel mixtures was minimized. Consequently, the effect of surface charges hindering the transport of the particles through the hydrogel matrix is not significant.

Sample	Zeta Potential / mV
Gold Nanoparticles	-29.80 ± 1.42
GelMA	-12.6 ± 0.5
Collagen I	6.6 ± 0.3
3 Coll I-3.75 GelMA	-6.0 ± 0.3
1 Coll I-11.25 GelMA	-10.7 ± 0.4

Table 2. Zeta Potential Measurements of Gold Nanoparticles and Hydrogels Samples.

During cancer progression, altered tumor microenvironment results in ECM remodeling and stiffening, indicating cancer aggression [157]. Investigation of human breast tumor biopsy samples has shown that normal and non-invasive stroma display elastic moduli up to 400 Pa, while elevated stromal stiffness (>5 kPa) was demonstrated for invasive breast cancer [158]. Indentation experiments were performed on the LSM in order to obtain the stiffness of the hydrogel samples.

As illustrated in **Figure 2.4**, hydrogel samples were stained with fluorescein (excitation at 488 nm and emission at 490-540 nm) and red fluorescent polystyrene particles (excitation at 543 nm and emission at 550-700 nm) were deposited on the surface of the samples. The indentation depth (δ) caused by the indenters was tracked by XZ- and YZ- cross section images of the pellets after Z-stack imaging acquisitions. **Figure 2.4** shows a typical result obtained in those indentation experiments.

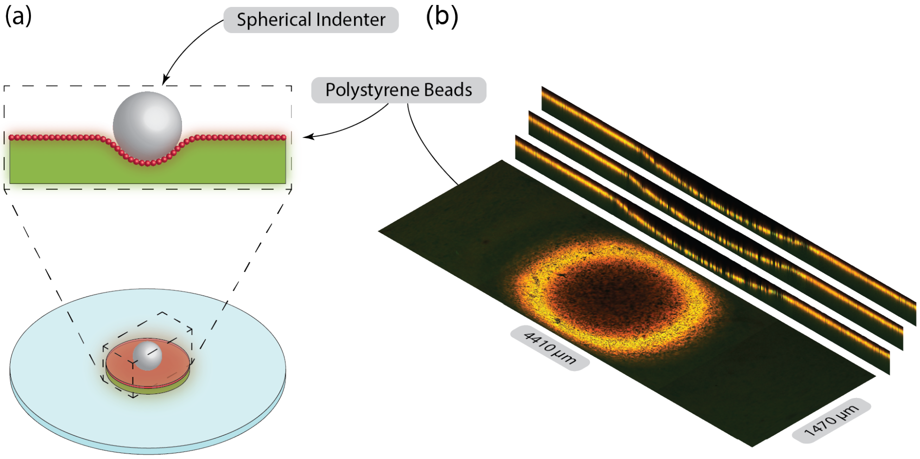

Figure 2.4 Indentation Experimental Set-up
(a) Hydrogel pellets were fluorescently labeled with fluorescein sodium salt (green), followed by deposition of red fluorescent polystyrene particles on the surface of the gels. Spherical indenters (Silicon Nitride and Stainless Steel) were carefully positioned in the hydrogel surface, causing a deformation on the gel samples. (b) Indentation depths were visualized on the laser scanning microscope, where XZ- and YZ- cross section images of the hydrogel samples were obtained.

Measurements of elastic moduli of 4.0 mg mL^{-1} collagen I samples (4 Coll I) were performed using a 1/32” spherical Si_3N_4 indenter (density of 3.184 g cm^{-3}). **Figure 2.5(inset)** shows that pure collagen samples demonstrated low stiffness values (54 ± 2 Pa). However, stiffness enhancement was obtained when collagen I was combined with GelMA to a final concentration of 3.0 mg mL^{-1}. For this 3 Coll I-3.75 GelMA composite, the elastic modulus increased from 139 ± 5 Pa to 183 ± 10 Pa. Since this enhanced elastic modulus value is within the range of normal tissue stiffness as seen in **Table 3**, the 3 Coll I-3.75 GelMA composite was selected to mimic regular ECM *in vitro*.

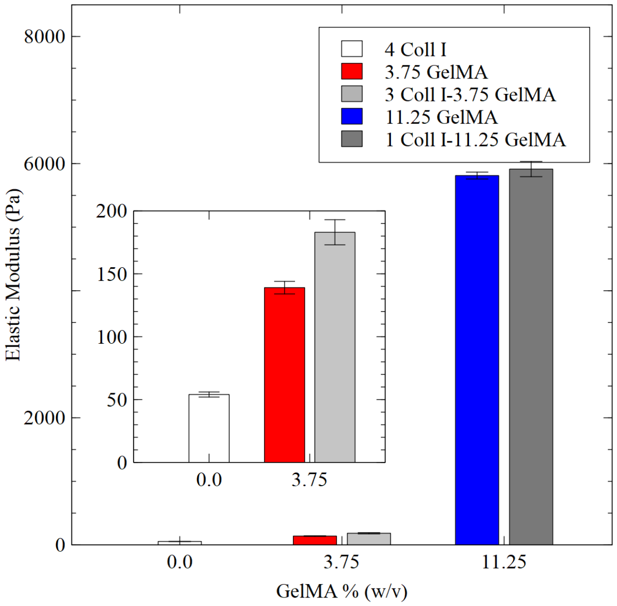

Figure 2.5 Elastic Moduli of Hydrogel Samples
Stiffness values obtained by indentation measurements. Hydrogel composites (light grey and dark grey) displayed stiffness enhancement when compared to GelMA samples (red and blue) and 4.0 mg mL^{-1} Collagen I (white). Three samples were analyzed for each hydrogel concentration in five different spots. Scale bars represent one standard deviation.

Since no significant deformation was obtained when Si_3N_4 indenter was deposited on the surface of 11.25% (w/v) GelMA samples, a 3/16” SS was selected for samples with high concentrations of GelMA. As presented in **Figure 2.5**, elastic moduli values displayed small stiffness enhancement on the 1 Coll I-11.25 GelMA composites (5914 ± 120 Pa) compared to pure 11.25% (w/v) GelMA samples (5812 ± 54 Pa). This can be explained due to low stiffness behavior of collagen I fibers, especially in low concentration. The elastic modulus obtained for the 1 Coll I-11.25 GelMA composites was 30 times higher than values obtained for 3 Coll I-3.75 GelMA composites (see **Figure 2.5**). In addition, since stiffness of 5914 ± 120 Pa can be found within the range of values for tumor tissues shown in **Table 3**, the 1 Coll I-11.25 GelMA composite was selected to mimic irregular (cancerous) ECM *in vitro*.

	Healthy Tissue Elastic Modulus (Pa)	Tumor Elastic Modulus (kPa)	References
Brain	100	0.17 - 16	[159–161]
Breast	150 - 400	3 - 8	[107, 158]
Colorectal	300 – 3,000	4 - 20	[162–164]
Liver	400 - 600	7 - 26	[165–167]
Lung	500 – 5,000	4 - 30	[168–171]

Table 3. Elastic Moduli of Soft Tissues and Related Cancers.

2.4.2. Evaluation of transport of fluorescein and CY3-GNP in microfluidic device

The massive growth of cancer cells inside of a tissue deforms and stiffens the ECM, leading to an increase in interstitial pressure in the tumor area. Consequently, the transport of nutrients and therapeutic drugs is limited to diffusion from capillary vessels toward the tumor area [71]. In addition, the increased interstitial pressure also contributes to a drainage of tissue lymphatics. Without efficient lymphatic drainage, nanomedicine, such as gold particles, can accumulate surrounding the tissue and slowly diffuse to reach the core of the tumor [172]. Diffusion of 10 nm CY3-GNP and fluorescein sodium salt through hydrogel composites was evaluated using the microfluidic device illustrated in **Figure 2.1**. Hydrogel composites were injected in the central channel in order to mimic normal (healthy and soft - 3 Coll I-3.75 GelMA) and irregular (cancerous and stiff - 1 Coll I-11.25 GelMA) ECM. Microfluidic chips were illuminated with UV light, followed by incubation at 37 °C, to allow polymerization of the hydrogels. After polymerization, a solution containing CY3-GNP (excitation at 543 nm and emission at 550-700 nm) and fluorescein sodium salt (excitation at 488 nm and emission at 490-540 nm) was injected in the lateral channel. The small sample volume required, and set-up practicality of the microfluidic device allowed the study of three transport conditions: 1) Diffusion-driven transport, i.e., no pressure gradient between lateral and central channels, 2) Diffusion and advection transport, with favorable pressure gradient by an increase in pressure in capillary-mimicking lateral channel, and 3) Diffusion and advection transport, with adverse pressure gradient by an increase in pressure in ECM-mimicking central channel.

The size of the GNP (10 nm) was defined based on the distribution of nanocarriers within the body and enhanced permeation through the tumor microenvironment. Since leaky vasculatures present pore sizes around 400 nm, nanoparticle dimensions must be below this cut-off size in order to perform efficient extravasation [69, 70]. The kidneys and liver also play an important role in selecting the optimal nanoparticle size. Particles smaller than 10 nm undergo renal clearance, while the liver is capable of capturing particles above 100 nm [71, 72]. Lastly, collagen display mesh size in the range of 20 to 40 nm in solid tumors [173]. While particles with dimensions smaller than 20 nm are able to move through the collagen mesh, larger particles will have hindered transport [174]. In addition, smaller particles show faster diffusion in tissue than large nanocarriers [175].

Addition of fluorescein sodium salt to CY3-GNP solution served four important purposes. First, fluorescein sodium salt displays a molecular weight (MW = 376.3 g/mol) similar to the MW of anti-cancer drugs such as Carboplatin (371.2 g/mol), and Capecitabine (359.3 g/mol) and, consequently, similar transport responses may be expected of fluorescein compared to these drugs. Second, the size of fluorescein dye (~ 1 nm) is similar to the size of cell nutrients, such as glucose and amino acids. Third, fluorescein provided an excellent fluorescence collection window when combined with CY3-GNP and, since both components were negatively charged, the effect of surface charge on transport was not significant. Fourth, tracking transport of fluorescein dye combined with CY3-GNP confirmed that the fluorescence signal obtained from 10 nm CY3-GNP was coming from CY3 molecules attached to the surface of the particles, instead of dissolved in solution.

2.4.3. Diffusion-driven transport: no pressure gradient between microchannels

In the case of diffusion-only, inlets and outlets of central and lateral channels were kept open and only atmospheric pressure was being exerted on top of the microfluidic device. After injection of a solution containing 10 nm CY3-GNP and fluorescein, diffusion of these components was tracked by fluorescence under the LSM, as presented in **Figure 2.6**.

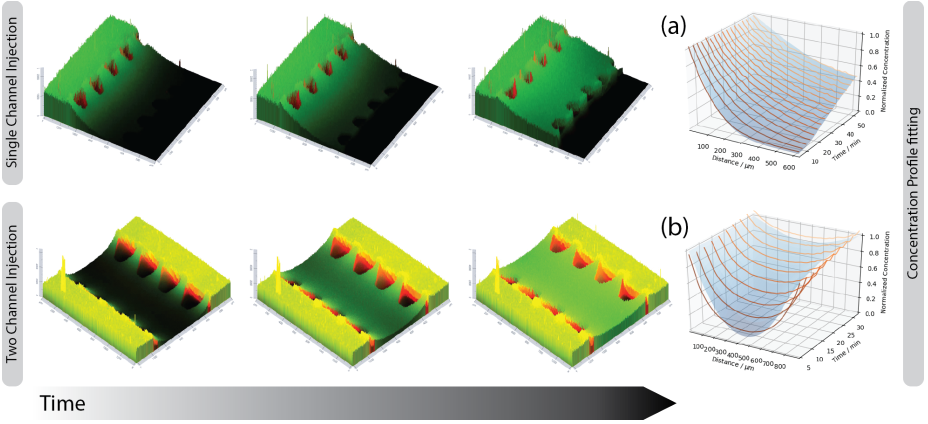

Figure 2.6 Diffusion Concentration Profiles
Fluorescent images obtained in the LSM of diffusion of CY3-GNP (red) and fluorescein sodium salt (green) inside microfluidic device. Experimental data obtained from LSM was fitted using the appropriate transport equation. (a) For single capillary channel injection, diffusion fitting of CY3-GNP and fluorescein resulted on a decaying profile. (b) When the species were injected in both lateral channels, diffusion fitting of the species displayed a parabolic-shaped concentration profile.

In order to determine diffusion coefficient values for the different species, fluorescence intensity signal tracked inside the microfluidic device at different time steps was fitted using the transport equations described in the Appendix A. **Figure 2.7** and **Table 4** summarize the diffusion coefficients obtained for different experiments. Fluorescein dye displayed diffusion coefficients of (1.63 ± 0.13) × 10^{-6} cm^2 s^{-1} and (7.78 ± 0.08) × 10^{-7} cm^2 s^{-1} in 3 Coll I-3.75 GelMA and 1 Coll

I-11.25 GelMA, respectively. In the case of CY3-GNP, diffusion coefficients of (1.07 ± 0.03) × 10^{-6} cm^2 s^{-1} and (4.42 ± 0.15) × 10^{-7} cm^2 s^{-1} in 3 Coll I-3.75 GelMA and 1 Coll I-11.25 GelMA were obtained, respectively. As the size of fluorescein sodium salt molecules (~1 nm) is 10 times smaller compared to the GNPs (~10 nm), it was expected to diffuse faster. However, a 60% decrease in diffusion was demonstrated for GNP when comparing results obtain in soft and stiff composite hydrogels. In the case of fluorescein, dye particles displayed a 50% decrease in diffusion when their transport from both hydrogels were compared. The decrease in diffusion resulted from a decrease in porosity of the hydrogel composites, in which 3 Coll I-3.75 GelMA displayed (71.9 ± 3.8)% while 1 Coll I-11.25 GelMA showed a porosity of (45.5 ± 4.5)%, as illustrated by **Figure A.3**. This decrease in porosity resulted in a smaller media volume available for diffusion of the species within the stiff hydrogel samples. In addition, the change in morphologies observed in the stiff hydrogel composites (1 Coll I-11.25 GelMA) may have induced a difference in tortuosity, resulting in a decrease in diffusive transport.

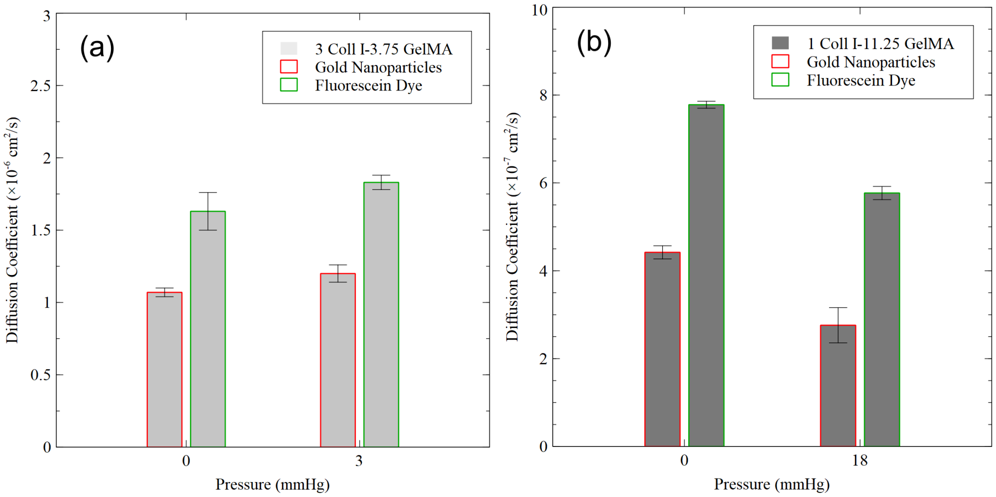

Figure 2.7 Diffusion Coefficients in Hydrogel Composites
Determination of diffusion coefficients for CY3-GNP (red) and fluorescein (green) was performed in both hydrogel composites, (a) 3 Coll I-3.75 GelMA, and (b) 1 Coll I-11.25 GelMA. Three samples were analyzed for each hydrogel concentration and each pressure condition. Scale bars represent one standard deviation.

Hydrogel Composite	Pressure (mmHg)	CY3-GNP Diffusion Coefficient ($cm^2\ s^{-1}$)	R^2	Fluorescein Diffusion Coefficient ($cm^2\ s^{-1}$)	R^2
3 Coll I-3.75 GelMA	0	$(1.07 \pm 0.03) \times 10^{-6}$	0.92±0.05	$(1.63 \pm 0.13) \times 10^{-6}$	0.89±0.07
	3	$(1.20 \pm 0.06) \times 10^{-6}$	0.86±0.06	$(1.83 \pm 0.05) \times 10^{-6}$	0.90±0.05
1 Coll I-11.25 GelMA	0	$(4.42 \pm 0.15) \times 10^{-7}$	0.96±0.02	$(7.78 \pm 0.08) \times 10^{-7}$	0.97±0.01
	18	$(2.76 \pm 0.40) \times 10^{-7}$	0.93±0.05	$(5.77 \pm 0.15) \times 10^{-7}$	0.95±0.04

Table 4. Diffusion Coefficient Values for CY3-GNP and Fluorescein in Hydrogel Composites.

2.4.4. Diffusion and advection transport: increased pressure in capillary-mimicking channel

Within normal conditions (non-cancer tissue environment), a net outward pressure in a range of 1 to 3 mmHg from capillary channels towards the surrounding tissue drives transport of nutrients [46]. Hence, to simulate regular tissue conditions inside the microfluidic device, the soft composite mixture (3 Coll I-3.75 GelMA) was injected in the central microchannel and, after hydrogel polymerization, a liquid column containing CY3-GNP and fluorescein sodium salt solution was added to the inlets and outlets of the lateral channel, to a final hydrostatic pressure of 3 mmHg. Transports of CY3-GNP and fluorescein dye were tracked, as described previously, by fluorescence imaging.

The results, summarized in **Figure 2.7**, indicated that the increase of pressure in the lateral channel contributed to the transport of both GNP and dye molecules through the hydrogel composite, marginally increasing the diffusion coefficients. The diffusion coefficients of both CY3-GNP and fluorescein displayed obtained by applying the additional pressure ($(1.20 \pm 0.06) \times 10^{-6}$ $cm^2\ s^{-1}$ and $(1.83 \pm 0.05) \times 10^{-6}$ $cm^2\ s^{-1}$, respectively) increased by 12% when compared to the values obtained in absence of the pressure gradient.

2.4.5. Diffusion and advection transport: increased pressure in ECM-mimicking microchannel

The accelerated cancer cell growth within a confined space causes an increase in the interstitial pressure within the tumor area and, consequently, a net outward pressure in a range of 2 to 18 mmHg is observed from the cancer area to the surrounding tissue [46]. Accordingly, in order to mimic the tumor microenvironment within the microfluidic device, injection of stiff hydrogel composite mixture (1 Coll I-11.25 GelMA) was performed in the central channel. After polymerization, a water column with hydrostatic pressure equivalent to 18 mmHg was added to the inlets and outlets of the ECM-mimicking central channel. The pressurization of the entire central channel containing the hydrogel was performed in order to evaluate the effect of tumor interstitial pressure on the transport of species. Once this channel was pressurized, a solution containing CY3-GNP and fluorescein sodium salt was injected in the lateral channels. Change in fluorescence signal within time and distance was tracked inside the microfluidic device.

In the presence of an adverse pressure gradient, CY3-GNP and fluorescein displayed a decrease in the diffusion coefficient. **Figure 2.7** presents the diffusion coefficients in hydrogel composites and the diffusion values of $(2.76 \pm 0.40) \times 10^{-7}$ cm^2 s^{-1} and $(5.77 \pm 0.15) \times 10^{-7}$ cm^2 s^{-1} were obtained for CY3-GNP and fluorescein, respectively. Comparing diffusion results obtained in the absence and in the presence of an adverse pressure gradient, a 37.5% decrease was seen for CY3-GNP, while fluorescein displayed a 25% decrease. These values indicated that the effect of adverse pressure is higher in CY3-GNP than in fluorescein dye molecules, due to a difference in size of the species. These results indicate that the properties of the tumor microenvironment play a significant role on the transport of species. High interstitial pressure in the tumor area is responsible for hindering diffusion and, consequently, decreasing effective delivery of anti-cancer treatment to the target areas.

The transport of Immunoglobulin G (IgG) has been previously studied in a murine mammary carcinoma, displaying diffusion coefficients of $(1.24 - 3.12) \times 10^{-7}$ cm^2 s^{-1} [176, 177]. Due to the similar dimensions of this antibody (14.5 nm × 8.5 nm × 4.0 nm) compared to the GNP used in this study, the diffusion coefficient value of $(2.76 \pm 0.40) \times 10^{-7}$ cm^2 s^{-1} obtained for CY3-GNP highlighted the feasibility of application of Collagen I-GelMA composites in the creation of mimic *in vitro* ECM.

2.4.6. MCF-7 cells encapsulated in hydrogel composites

Assessment of cell viability is essential for the application of the hydrogel as an *in vitro* tissue-mimicking biomaterial. Viability of MCF-7 cells was evaluated by using PrestoBlue cell viability assay. After 1h of incubation at 37°C, the 1X resazurin-based PrestoBlue reagent was modified by the reducing environment of the cells, turning into a fluorescent solution. Fluorescence was measured using a plate reader on days 1, 3, 5 and 7 after hydrogel preparation, at 560 nm excitation and 590 nm emission. Fluorescence values obtained for blank samples of 1X PrestoBlue on days 1, 3, 5 and 7 were subtracted from the fluorescence intensity obtained for all hydrogel samples in each respective day. Increasing fluorescence intensity in all hydrogel samples, as illustrated by **Figure 2.8**, indicates increase in cell viability and proliferation. Addition of collagen type I to the GelMA samples resulted in increase of fluorescence intensity, and, consequently, provided a better matrix for the MCF-7 cells. Higher cell viability was verified in the stiffer hydrogel composite, 1 Coll-11.25 GelMA, displaying the impact of matrix composition and stiffness on cell proliferation. Control samples were also incubated with PrestoBlue for 1h. High fluorescence signal obtained for the control samples is related to the direct contact by the cells with PrestoBlue. For cells encapsulated in the hydrogel samples, PrestoBlue had to diffuse through the matrix in order to reach the cells.

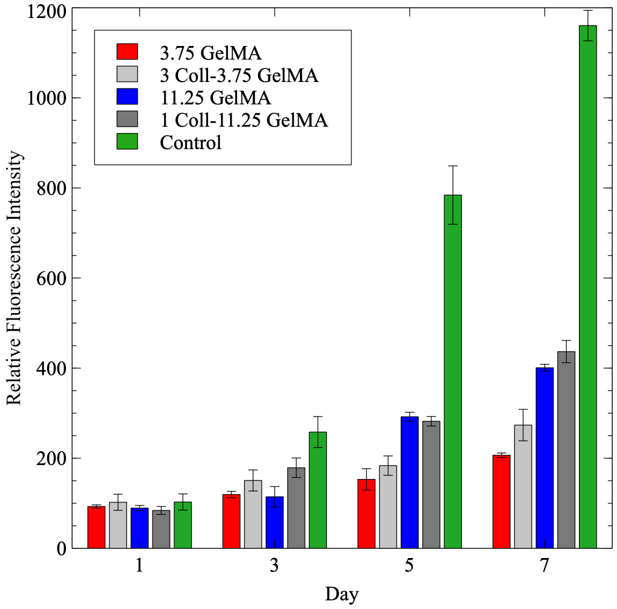

Figure 2.8 Quantification of Metabolic Activity by PrestoBlue
Higher fluorescence signal was obtained in composite hydrogels (light and dark grey bars) compared with GelMA hydrogels (red and blue bars). Control samples are labeled in green. Five samples were analyzed for each hydrogel concentration and for each control. Scale bars represent one standard deviation.

Live/dead staining demonstrated that the MCF-7 cells were viable and mostly alive (green fluorescent cells), with little evidence of dead cells (red fluorescent cells) over cell monolayer and all hydrogel samples at day 7, as illustrated by **Figure 2.9(a, b, c, d and e)**. In addition, no significant differences in cell morphology were observed in the different hydrogel samples, as indicated by the Appendix A. Staining of DNA and actin filaments of MCF-7 cells encapsulated in hydrogel composites revealed the formation of cell colonies, as shown in **Figure 2.9(f and g)**., in which cell clusters were developed with disorganized nuclei, as previously seen [178].

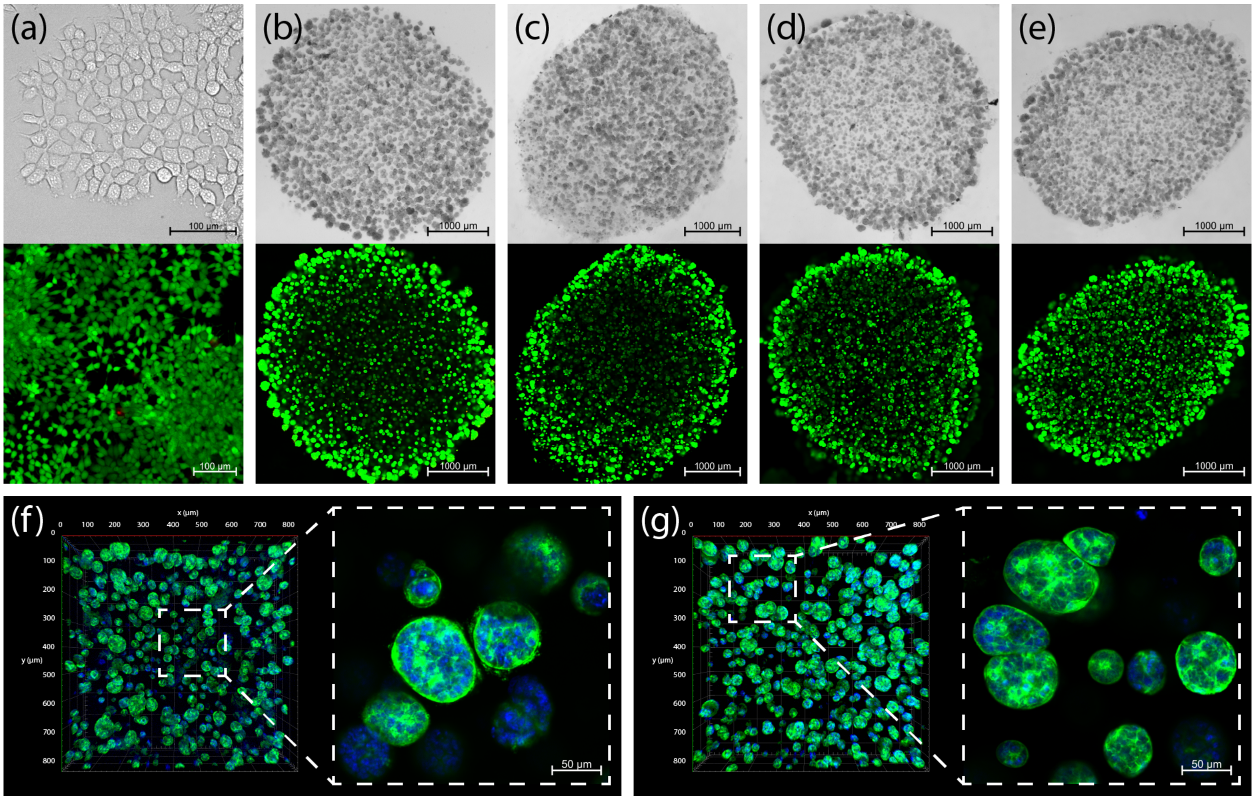

Figure 2.9 MCF-7 Cell Images
Bright field (top), live/dead (middle) and DAPI/Phalloidin (bottom) images of MCF-7 cells: a) Cells cultured in well plate displayed a flat morphology, while cells cultured in hydrogel samples (b) 3.75 GelMA, c) 3 Coll I-3.75 GelMA, c) 11.25 GelMA , d) 1 Coll I-11.25 GelMA) developed 3D cell cluster formation. DAPI/Phalloidin staining of MCF-7 cells encapsulated in f) 3 Coll I-3.75 GelMA and g) 1 Coll I-11.25 GelMA exposed the formation of cell colonies with disorganized nuclei. Scale bars of 100 µm and 1000 µm were used for bright field and live/dead images of 2D and 3D cell cultures, respectively. DAPI/Phalloidin images contain 50 µm scale bars.

2.5. Conclusion

The use of nanoparticles in cancer treatment extends from drug delivery systems to radiation therapy. However, while blood vasculature displays enhanced permeation during cancer progression, further movement towards the tumor is guided by advection and diffusion. The increase in interstitial fluid pressure within the tumor hinders fluid movement, resulting in diffusive transport as the main delivering method of drug and particles to the tumor area. Consequently, it is important to understand the impact of characteristics of the tumor microenvironment, such as matrix stiffening and high pressure, on the transport of species. In this work, transport of CY3-GNP and fluorescein sodium salt molecules through ECM-mimicking hydrogel composites was investigated inside of a microfluidic device. Tuning the collagen type I-gelatin methacryloyl hydrogel composition allowed the simulation of *in vitro* healthy ECM (soft) and cancerous ECM (stiff) in terms of elastic moduli. Hydrogel composites displayed elastic moduli of 183 ± 10 Pa 5914 ± 120 Pa for 3 Coll I-3.75 GelMA and for 1 Coll I-11.25 GelMA, respectively, similar to elastic modulus values displayed by healthy and cancerous breast ECM. Therefore, while CY3-GNP demonstrated negative zeta potential the combination of collagen I and GelMA resulted in a negatively charged composite, minimizing charge interaction between CY3-GNP and ECM-mimicking hydrogels. Comparing healthy properties (favorable pressure gradient of 3 mmHg and 3 Coll I-3.75 GelMA) with cancerous conditions (unfavorable pressure gradient of 18 mmHg and 1 Coll I-11.25 GelMA), decreases of 77% and 68% in the diffusion coefficient were obtained for CY3-GNP and fluorescein, respectively. These results indicated that with the opposing advection, adverse pressure gradient also hindered diffusion. In addition, in absence of pressure gradient, hydrogel matrix properties demonstrated to have a considerable impact on decreasing diffusion transport of species, resulting in a 60% and 50% decrease for CY3-GNP and dye, respectively. The decrease in diffusive transport demonstrated the impact of the tumor microenvironment on transport of species and highlighted the importance of using more realistic ECM-mimicking hydrogels. Therefore, this study was able to investigate the influence of tumor microenvironment on the transport of species using a collagen type I-GelMA composite. The combination of a more realistic ECM in terms of mechanical properties with a pressure gradient inside of a microfluidic device allowed the determination of diffusion for cancerous and healthy conditions. The proximity of elastic moduli and diffusion coefficient values with literature values obtained in real tumors emphasizes the ability of our system to mimic *in vitro* ECM using a relatively simple chip design and a two-component hydrogel composite.

In order to resemble a real tissue *in vitro*, hydrogels need to provide not only similar mechanical properties and microarchitecture to the native tissue, but also should allow cell adhesion and proliferation. While collagen type I is a native extracellular matrix component, the mechanical properties of this material limits its applications due to its low elastic modulus. GelMA, on the other hand, can have its mechanical properties tuned according to its concentration. In addition, the presence of cell binding motifs, such as binding sequence (RGD), enhances cell adhesion to GelMA. Therefore, collagen type I-GelMA composites were able not just to mimic mechanical and chemical properties of native ECM, but also provided high cell viability and the formation of 3D cancer clusters, allowing the use of these composites not just in the creation of *in vitro* tumors, but also as an *in vitro* platform to study drug delivery mechanisms.

Chapter 3 Exploring Diffusion and Cellular Uptake: Charged Gold Nanoparticles in an *in vitro* Breast Cancer Model*

Karolina P. Valente [1], Afzal Suleman [1], Alexandre G. Brolo [2]

[1] Department of Mechanical Engineering, University of Victoria, Victoria, BC, Canada.
[2] Department of Chemistry, University of Victoria, Victoria, BC, Canada.

*Manuscript to be submitted to Biomaterials Science (RSC).

Key words:

Gold Nanoparticles; Breast Cancer; Cellular Uptake; Diffusion; Microfluidics

Author contribution:

Karolina P. Valente designed, set-up, performed experiments and data analysis, wrote, reviewed, and edited manuscript. Afzal Suleman and Alexandre G. Brolo provided feedback on the experimental analysis and edited the manuscript.

3.1. Abstract

Gold nanoparticles have emerged as a prominent tool in nanomedicine, particularly for applications in cancer diagnostic and treatment. One of the challenges for the successful implementation of gold nanoparticles in cancer therapy is their delivery to the specific cancer area within the tumor microenvironment. The presence of cancer enables a poorly organized vascularization system, increasing the pressure with the microenvironment, limiting the uptake of particles. Physicochemical properties of the gold nanoparticles (size, shape, and surface charge) also play a significant effect on diffusion to the tumor site and cellular uptake. In this work, we analyzed the transport of 10 nm gold nanoparticles with different surface charges (neutral, negative and positive) through a hydrogel composite. 3D *in vitro* models composed of breast cancer cells loaded in the hydrogel composite were used for qualitative and quantitative evaluation of cellular uptake of the gold nanoparticles. Surprisingly, an inverse correlation between the diffusion coefficients of the nanoparticles and cellular uptake was demonstrated. Positively charged gold nanoparticles displayed high cellular uptake, although their diffusion coefficient indicated slow transport through the hydrogel matrix. Neutral particles, on the other hand, displayed fast diffusion and but the lowest cellular uptake. The results obtained indicate that nanoparticle diffusion and cellular uptake should be studied together in realistic *in vitro* models for a true evaluation of transport in tumor microenvironments.

3.2. Introduction

Gold nanoparticles have been extensively studied and applied in biomedicine [179]. The strong localized surface plasmon resonances in GNPs are explored in a variety of nanomedicine applications, such as in photothermal therapy and in biological imaging [180, 181]. GNPs can also be used as radiotherapy enhancers, due to the high atomic number of gold [127]. However, the enhanced dose deposition can damage normal tissues [77], and the success of GNPs-enhanced radiotherapy relies on the degree of penetration of the particles inside the tumor area.

Physicochemical parameters such as shape, size, and surface charge, play a role in the transport of GNPs in tissue environment [182]. Although GNPs can be produced in different shapes, it has been demonstrated that spherical particles present higher uptake efficiency than other shapes, such as nanostars [183, 184]. A size dependent study of spherical GNPs, with particles sizes ranging from 14 to 100 nm, concluded that 50 nm nanoparticles displayed the highest cellular uptake efficiency in mammalian cells [185]. Surface chemistry can also influence the interaction between cells and nanoparticles. Positively charged nanoparticles have been shown to display higher cellular uptake than negatively or neutrally charged particles [186, 187]. This is due to the favorable electrostatic interaction between the positively charged GNPs and the negatively charged cell membrane [188].

Although the effect of physicochemical parameters of GNPs has been extensively studied in two-dimensional cell cultures, these 2D models are unable to replicate the cell-cell and cell-extracellular matrix signaling of complex three-dimensional tissues [7]. 3D cell culture models should provide a more realistic system to study the delivery of nanomedicine to tumor sites, bridging the experimental gap between *in vivo* and *in vitro* models. In addition, the tumor microenvironment also impacts the delivery of nanoparticles to cancerous areas. The unique features seen in solid tumors, such as leaky vasculature, can lead to an accumulation of nanoparticles around the tumor area [69]. However, uncontrollable growth of cancer cells results in an increase in interstitial pressure, limiting the delivery of nanomedicine to a diffusion transport mechanism [189]. Furthermore, the complex and dense acts as a barrier, retarding the diffusion of particles in the tumor interstitium [190].

While there are many studies on the cellular uptake of GNPs [191–194] that explore the effects of size, shape, and charge, the comparison between diffusion and cellular uptake in 3D *in vitro* models has been barely explored. Recently [195], we introduced a tumor microenvironment-on-a-chip model to explore the effects of the diffusion of GNPs. The ECM-mimicking model consisted of hydrogel composite matrices formed by different concentrations of Gelatin Methacryloyl and Collagen type I. The value of the elastic modulus from the ECM-mimicking matrix composed of 11.25% (w/v) GelMA and 1.0 mg/mL Collagen I was in agreement to the recorded for breast cancer tissues. Our results showed a 77% decrease in diffusion of 10 nm GNP when ECM stiffening and interstitial pressure were simulated inside a microfluidic device (as described in Chapter 2).

In this study, the use of GNPs was explored in two ways, by diffusion and cellular uptake, as illustrated in **Figure 3.1**. Diffusion was investigated by examining the effect of surface charge on the transport of GNPs on a cancerous-mimicking ECM using a microfluidic device. In addition, quantitative and qualitative analysis on cellular uptake of the charged GNPs in 3D *in vitro* models of breast cancer cells (MCF-7 and MDA-MB-231) was also performed.

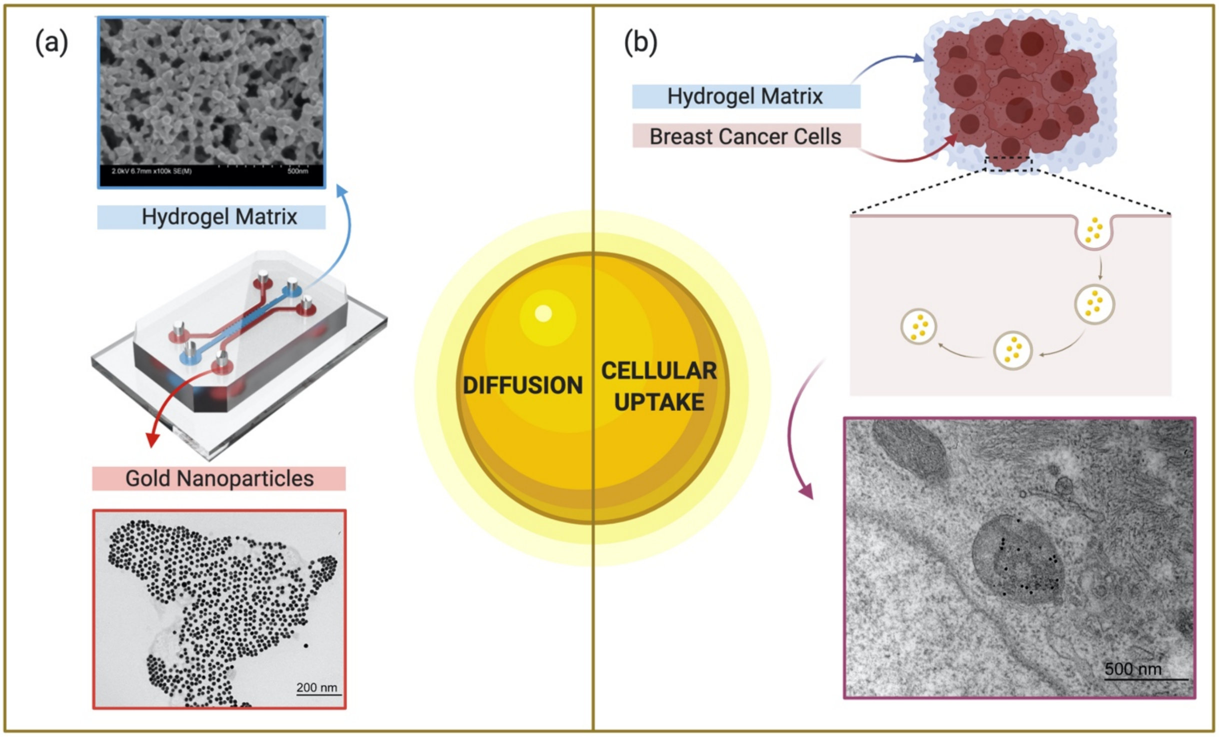

Figure 3.1 Study of Diffusion and Cellular Uptake
(a) Diffusion of gold nanoparticles from the lateral channels (labeled in red) of the microfluidic device to the central channel (labeled in blue). Macroscopic movement of the particles was detected on a Laser Scanning Microscope by tracking fluorescence. (b) Cellular uptake of gold nanoparticles was investigated by allowing particles to be in contact with breast cancer cells encapsulated in hydrogel matrix for 48 h. Detection of particles inside the cells was performed by sectioning hydrogel pellets and visualizing the sections under Transmission Electron Microscope.

3.3. Materials and Methods

3.3.1. Materials

Gelatin methacryloyl (Bloom 300, ≥ 80% degree of substitution), gelatin from porcine skin (Bloom 300), 2-hydroxy-4′-(2-hydroxyethoxy)-2-methylpropiophenone (Irgacure 2959) (98%), glutaraldehyde solution 25 wt% in water, 3-(trimethoxysilyl)propyl methacrylate (98%) (TMSPMA), phosphate buffered saline (PBS), sodium cacodylate trihydrate, osmium tetroxide 4% in water solution, propylene oxide, and Epoxy embedding medium (Epon) were purchased from Sigma-Aldrich. CULTREX 3D Culture Matrix Rat Collagen I was purchased from Trevigen at a concentration of 5 mg/mL. Sodium dodecyl sulfate, sodium bicarbonate, and glycine were purchased from Bio Basic Canada Inc. P-type boron silicon wafers measurement 76.2 mm of diameter were purchased from Silicon Materials Inc. Permanent Epoxy Resist SU-8 100 and SU-8 Developer were purchased from MicroChem Corporation. Sylgard 184 silicone elastomer kit was obtained from Dow Corning Corporation. MCF-7 (HTB-22) and MDA-MB-231 (HTB-26) cells were obtained from Facility for Biomolecular Sample Preparation at University of Victoria. Dulbecco's Modified Eagle's Medium (DMEM), fetal bovine serum (FBS), penicillin-streptomycin, 10X PrestoBlue cell viability reagent, and LIVE/DEAD viability/ cytotoxicity kit for mammalian cells, and Pierce^{TM} 16% Formaldehyde (w/v) methanol-free were purchased from ThermoFisher Scientific. DAPI staining solution and phalloidin-iFluor 488 reagent were obtained from Abcam. Eagle's Minimum Essential Medium (EMEM) was obtained from ATCC. Fluorescent spherical 10 nm gold nanoparticles were obtained from Nanopartz with three different surface charges: neutral (CY3-Zero-GNP), positive (DY633-Positive-GNP) and negative (FITC-Negative-GNP).

3.3.2. Fabrication of Microfluidic Device

The microfluidic device was fabricated by photolithography, as described previously [195]. Briefly, a 400 μm thick SU-8 100 film was spin coated on top of a silicon wafer. The wafer was soft baked for 30 min at 65 °C and 90 min at 95 °C. Using a photolithography mask, the defined design was patterned on top of the SU-8 layer after exposure to UV light for 7 seconds. The assembly was then post baked at 95°C for 90 min, prior to the development step. The wafers were developed using SU-8 developer solution and rinsed with isopropanol. Polydimethylsiloxane (PDMS) was prepared by 10:1 mixture of silicone elastomer base and elastomer curing agent. After degassing in a vacuum chamber, the PDMS was then deposited on top of the SU-8 patterned silicon wafer. The assembly was baked at 150 °C for 3 h in order to allow PDMS polymerization. The PDMS layer was then peeled off from the wafer and inlet and outlet ports were punched using biopsy punchers. The PDMS layer was permanently bonded to a glass slide using plasma cleaning.

The microfluidic design consisted of an ECM-mimicking central channel (700 μm width and 2.5 mm length), in which the hydrogel composite was located, and two identical capillary-mimicking lateral channels (1000 μm width), in which GNP solutions were injected. The larger width of lateral channels compared to the central channel ensured constant wall concentration of the gold solution, allowing the determination of the diffusion coefficient by Fick's second law.

3.3.3. Hydrogel Preparation

Collagen type I-Gelatin Methacryloyl composite was prepared as described previously [195]. A solution at a concentration of 15% (w/v) of GelMA was prepared in PBS containing 1% (w/v) Irgacure 2959. In addition, a solution of Collagen type I CULTREX was prepared to a final concentration of 4.0 mg/mL. In order to create a cancerous-mimicking ECM, Collagen I and GelMA were mixed to a final concentration of 1.0 mg/mL and 11.25% (w/v), respectively. The final pH of the composite mixture was adjusted to 7 using a 1M solution of NaOH.

This hydrogel mixture was injected in the central channel of the microfluidic device and the assembly was initially crosslinked under UV light (365 nm at 5.7 mW/cm^2) for 4 minutes and 20 seconds, followed by incubation at 37 °C for 30 minutes.

3.3.4. Transport of Gold Nanoparticles

The transport of 10 nm fluorescently labeled GNPs was evaluated by tracking the diffusional movement of the particles from the lateral channel of the microfluidic device through the hydrogel composite layer (located in the central channel). Gold nanoparticles displaying neutral, positive, and negative zeta potential values were used in this study. The electrical charge of the gold nanoparticles was determined by zeta potential measurements using a Particle Analyzer Litesizer 500 from Anton Paar. A volume of 10 µL of each particle sample was added to 1 mL of deionized water (pH 7) and transferred to a zeta potential omega cuvette. Refractive index, relative permeability, and viscosity values of 1.33, 73.368, and 8.9 x 10^{-4} Pa.s, respectively, were assumed to be the same as for water.

A volume of 10 µL of one of the gold nanoparticle solutions was injected in the lateral channel (capillary mimicking channel). Fluorescent confocal images were taken using a Laser Scanning Microscope (LSM) Zeiss 880 at an excitation and emission of 543 nm (Helium-Neon laser) and 570-700 nm for neutral particles, 633 nm (Helium-Neon laser) and 650-750 nm for positive particles, and 488 nm (Argon laser) and 500-650 nm for negative particles. Fluorescent images were taken using the line scan mode at 1024 x 1024 pixels, with an averaging of 2 images, with a pixel time of 0.77 µs, a frame time of 1.89 s, for every 3 minutes at room temperature to a total of 90 minutes. To prevent hydrogel dehydration, a humidity chamber was adapted on top of the LSM platform.

Zeiss Zen 2.3 software was used to obtain the intensity profiles for gold nanoparticles inside the microfluidic device at each point in time. After correlation of intensity values with concentration, the profiles were fitted using a one-dimensional transient diffusion medium solution for Fick's second law of diffusion [196], in which the diffusion coefficient D was obtained. Three samples were analyzed for each charge of GNP.

3.3.5. Breast Cancer Cells Encapsulated in Hydrogel Composite

Two breast cancer cell lines, MCF-7 and MDA-MB-231, were used in this study. MCF-7 cells were maintained in Dulbecco's Modified Eagle's Medium (DMEM), while MDA-MB-231 were kept in Eagle's Minimal Essential Medium (EMEM). Both media were supplemented with 10% fetal bovine serum and 1% penicillin-streptomycin. Cells were kept inside an incubator at 37 °C and 5% CO_2. Media was exchanged every 2 days and cells were passaged when 80% confluent.

Encapsulation of each breast cancer cell in the hydrogel composite mixture was achieved by adding a final concentration of 1×10^4 cells per 10 µL of hydrogel mixture, prior to crosslinking. A spacer was created by attaching two coverslips (400 µm total thickness) to the surface of a petri dish. The mixture containing the hydrogel composite and cells was pipetted in this spacer and a TMSPMA-modified coverslip was deposited at the surface of the sample (Appendix B). The assembly was then exposed to UV light (365 nm at 6.3 mW/cm^2) for 4 minutes in order to crosslink the GelMA, followed by incubation at 37 °C to polymerize the Collagen I. After polymerization, 3D hydrogel samples were created attached to the coverslip and these 3D samples were moved to well plates and incubated with 2 mL of fresh cell media.

Cancer cells were allowed to grow inside of the hydrogel matrix for 7 days. Characterization of cell viability in the pellets was performed using PrestoBlue assay (Appendix B) on days 1, 4, 7 (prior to exposure to GNPs), and 9 (after exposure to GNPs). Cell viability was also visualized by staining hydrogel pellets with LIVE/DEAD at final concentrations of 2 µM and 4 µM for calcein-AM and ethidium homodimer-1, respectively. Incubation was performed for 1 h at 37 °C. Fluorescence images were obtained in the LSM at an excitation of 488 nm and emission of 515-540 nm for calcein-AM. For ethidium homodimer-1, an excitation of 543 nm and an emission of 560-650 nm was used. Nuclei and actin filaments of the breast cancer cells encapsulated in the hydrogel matrices were also visualized by fluorescence imaging using DAPI and phalloidin-iFluor 488 staining solutions. Excitations and emissions of 360 nm and 400-500 nm were used for DAPI, while 488 nm and 500-600 nm were selected for phalloidin-iFluor 488.

3.3.6. Cell Uptake of Gold Nanoparticles

Breast cancer cells encapsulated in hydrogel matrices (3D hydrogel samples) were allowed to grow for 7 days. On day 7, after assessing cell viability, a cell media solution containing a final concentration of 1 x 10^{12} GNPs/mL was put in contact with hydrogel samples for 48 h inside of the incubator at 37 °C. After 48 h, the solution containing gold nanoparticles was removed from the wells, and the hydrogel pellets were washed three times with PBS. Some of these samples were chosen to assess cell viability using PrestoBlue (Appendix B). The remaining samples, after the PBS washing procedure, were fixed with Karnovsky's Cacodylate Buffered Glutaraldehyde-Formaldehyde (3% glutaraldehyde and 3% formaldehyde in 0.1 M cacodylate buffer) solution for 30 min.

For each charge (positive, negative, and neutral) of gold nanoparticles, 12 3D hydrogel samples were prepared for each cell line, for a total of 72 samples. From the 72 samples, 24 were used to assess cell viability, while 48 were used in the uptake of gold nanoparticles (24 samples for ICP-MS and 24 samples for TEM).

3.3.7. Transmission Electron Microscopy (TEM) Sectioning and Imaging

For qualitative analysis, 3D hydrogel samples were analyzed by TEM. After the fixation step of the hydrogel samples, a dehydration procedure was performed. The fixative solution was removed from hydrogel pellets and samples were washed three times in PBS. Samples were then fixed with a 1% osmium tetroxide solution prepared in PBS. The fixation step lasted for 1 h. After fixation, the 3D hydrogel samples were detached from coverslips and transferred to small vials. The dehydration procedure was performed according to the solvent replacement method [197, 198], in which solutions with increasing concentration of ethanol (50%, 70%, 80%, 90%, 95%, and 100%) were added to the hydrogel pellets. After the removal of 100% ethanol solution from sample vials, a solution of 100% propylene oxide was incubated for 10 minutes with the hydrogel pellets. This step was repeated twice, followed by incubation of samples with ratios of propylene oxide and epon of 3:1 (w/w) for 60 min, 1:1 (w/w) for 12 h, and 1:3 (w/w) for 180 min. After that, samples were incubated in pure epon for 4 h, followed by incubation in fresh epon solution for 12 h. After 12 h, samples were placed into fresh epon solutions and polymerized at 60 °C for 48 h. Sectioning of TEM samples was performed in the Electron Microscope Laboratory Facility at University of Victoria. Sections were stained for 10 min in uranyl acetate, followed by 4 min staining in lead citrate. Multiple sections were made for each hydrogel pellet.

TEM images of cell-loaded 3D hydrogel samples were taken using a Joel 1011 Transmission Electron Microscope. Multiple images were taken from each hydrogel pellet sample in order to assess the presence of gold nanoparticles.

3.3.8. Inductively Coupled Plasma-Mass Spectrometry

For quantitative analysis, the 3D hydrogel samples were analyzed by ICP-MS. After the fixation step of the hydrogel samples, samples were detached from coverslips and their masses were recorded. Samples were then moved to falcon tubes and digested using 250 µL of aqua regia (3:1 ratio $HCl:HNO_3$) for 1 h in a mineral oil bath at 200 °C. After digestion, samples were then diluted to 4% (v/v) acid content with deionized water and submitted to ICP-MS (Agilent 8800).

Control samples were prepared using 3D hydrogel samples containing cells in the absence of GNPs, and hydrogel samples in the presence of GNPs without cells. For each type of control, 5 samples were used, for a total of 20 samples for both cell lines. In addition, 4 samples of 4% (v/v) aqua regia with deionized water were also processed by ICP-MS.

The concentration of gold per gram of 3D hydrogel samples and of controls were obtained by using the gold amount in ppb obtained by ICP-MS and diving it by the recorded mass of the

3D hydrogel sample. The concentration of gold in the control samples were subtracted from the respective 3D hydrogel sample with the same charge of GNPs. Gold concentrations in the control samples are illustrated in Appendix B.

3.4. Results and Discussion

3.4.1. Evaluation of Transport of Gold Nanoparticles in the Microfluidic Device

The growth of cancer cells within healthy tissue causes reorganization of the ECM, resulting in a change of the tissue microenvironment. The proliferation of the cancer cells creates an increase in the interstitial pressure in the surrounding tissue and the ECM [43]. In addition to pressure build up, waste products accumulate in the cancer area, resulting in the formation of hypoxic regions that affects the local pH [45]. Protein deposition, such as collagen and fibronectin, is also a consequence of cancer growth, resulting in ECM stiffening [38]. A disorganized vascular network, combined with an increase in interstitial pressure inhibits the distribution of therapies to the cancer area by convection, limiting their delivery to diffusion [37].

In order to analyze the diffusion of GNPs in cancerous ECM-mimicking hydrogel, a concentration of 11.25% (w/v) of GelMA and 1.0 mg/ml of Collagen type I was injected in the central channel of the microfluidic device shown in **Figure 3.2**. This hydrogel composite displayed an elastic modulus of 5914 ± 120 Pa [195], showing stiffness within the range of elastic moduli values for breast tumor (3-8 kPa) [107, 158]. After polymerization of the hydrogel composite, fluorescently labeled 10 nm gold nanoparticles were injected in one of the lateral channels of the microfluidic device and their fluorescence intensity signal was tracked at different time steps under the LSM.

In order to analyze the diffusion of gold nanoparticles in cancerous ECM-mimicking hydrogel, a concentration of 11.25% (w/v) of GelMA and 1.0 mg/ml of Collagen type I was injected in the central channel of the microfluidic device. As we have shown previously [195], this hydrogel composite displayed an elastic modulus of 5914 ± 120 Pa, showing similar stiffness within the range of elastic moduli values for breast tumor (3-8 kPa) [107, 158]. After polymerization of the hydrogel composite, fluorescently labeled 10 nm gold nanoparticles were injected in one of the lateral channels of the microfluidic device and their fluorescence intensity signal was tracked at different time steps under the LSM.

The size of the GNP was selected based on the potential pathways for nanocarriers within the body. Cancer cells in hypoxia secrete angiogenic factors such as vascular endothelial growth factors, in order to induce growth of endothelial cells and stimulate proliferation of blood vessels [50]. Sprouting of new blood vessels to feed the tumor results in the creation of a disorganized vessel network, displaying a leaky vasculature with pore sizes below 400 nm [70]. In addition, particles smaller than 10 nm can undergo renal clearance, while particles above 100 nm are captured by the liver [199, 200]. Therefore, efficient delivery of nanocarriers to the tumor area requires nanoparticles with diameters in the range between 10 and 100 nm. However, considering that convection in the tumor microenvironment is limited, and the penetration of the nanoparticles is driven by diffusion, smaller nanoparticles will diffuse faster towards the core of the tumor. Large nanoparticles, on the other hand, are unable to penetrate the tumor interstitial matrix [201]. In addition, nanoparticles with diameters larger than 20 nm are unable to move through a collagen mesh with average mesh size ranging from 20 nm to 40 nm [173, 174]. Considering all the above, 10 nm gold nanoparticles were selected for this study.

The surface charges of the gold nanoparticles and hydrogel composite were analyzed, and the zeta potential measurements are presented in **Table 5**. As indicated in **Table 5**, neutral nanoparticles displayed a zeta potential value of -9.8 ± 0.4 mV, while positive and negative particles showed zeta potentials equal to 31.6 ± 1.5 mV and -34.5 ± 1.7 mV, respectively. GNPs were injected in the capillary-mimicking lateral channel of the microfluidic device. **Figure 3.2** presents an image obtained in the LSM that illustrates the diffusion of fluorescently labeled GNPs through the hydrogel composite. **Table 6** shows the diffusion coefficients for neutral, positively and negatively charged GNPs obtained using the fluorescence method summarized in **Figure 3.2**. Diffusion coefficient values for the GNPs through the cancerous ECM-mimicking hydrogel composite showed that the transport of neutral nanoparticles was faster ((6.45 ± 0.27) x10 $^{-7}$ cm^2/s), compared to the movement of positively and negatively charged GNPs. In addition, positively charged GNPs displayed the slowest diffusion through the hydrogel matrix, with a diffusion coefficient of (2.49 ± 0.18) x10 $^{-7}$ cm^2/s, compared to a value of (4.15 ± 0.16) x10 $^{-7}$ cm^2/s obtained by negative particles (**Table 6**). The diffusion coefficient of the negatively charged GNPs in **Table 6** is in agreement with our previous results ((4.42 ± 0.15) x10 $^{-7}$ cm^2/s) [195].

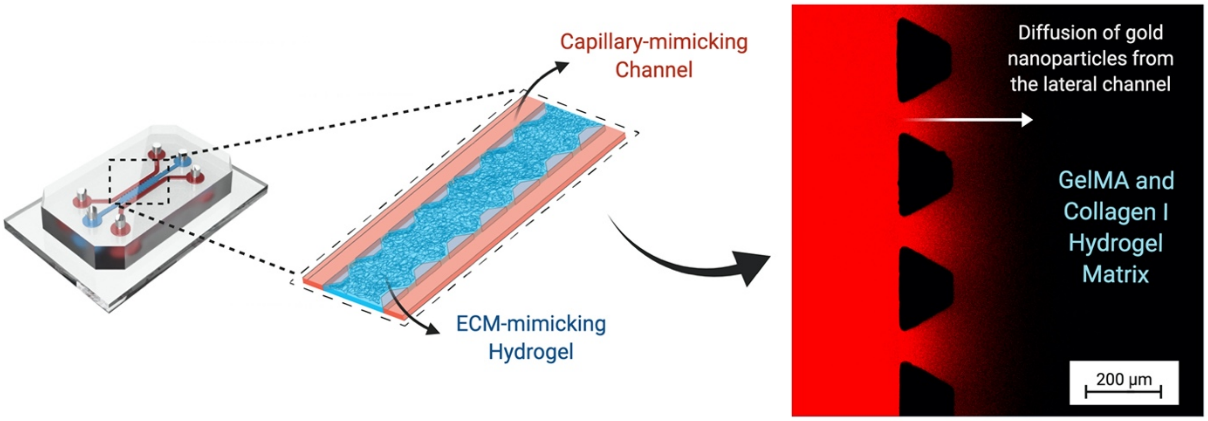

Figure 3.2 Diffusion of Gold Nanoparticles
Gold nanoparticles were injected in the lateral channels (capillary-mimicking channel, labeled in red) of the microfluidic device and diffusion through the hydrogel matrix located in the central channel (ECM-mimicking channel, labeled in blue) was tracked by fluorescence. Due to the lack of fluorescence, hydrogel matrix provided a black background to the movement of the fluorescently labeled gold nanoparticles. Diffusion coefficient values were obtained by fitting fluorescence intensity profiles with one dimensional transient diffusion in a semi-infinite medium solution for Fick's second law.

Sample	Zeta Potential / mV
CY3-Zero-GNP	-9.8 ± 0.4
DY633-Positive-GNP	31.6 ± 1.5
FITC-Negative-GNP	-34.5 ± 1.7
Hydrogel Composite	-10.7 ± 0.4

Table 5. Zeta Potential measurements performed of fluorescently labeled gold nanoparticles and hydrogel composite matrix located in the central channel of the microfluidic device.

Sample	Diffusion Coefficient / cm^2s^{-1}	R^2
CY3-Zero-GNP	$(6.45 \pm 0.27) \times 10^{-7}$	0.96 ± 0.02
DY633-Positive-GNP	$(2.49 \pm 0.18) \times 10^{-7}$	0.91 ± 0.07
FITC-Negative-GNP	$(4.15 \pm 0.16) \times 10^{-7}$	0.93 ± 0.02

Table 6. Diffusion coefficient values obtained for gold nanoparticle diffusion through hydrogel composite matrix located in the central channel of the microfluidic device.

Nanoparticle diffusion through a charged polymeric network should depend strongly on the charges at the surface of the nanoparticle [156]. The hydrogel matrix displayed a zeta potential value of -10.7 ± 0.4 mV (**Table 5**), due to the combination of negatively charged GelMA [152] and slightly positively charged Collagen type I [195, 202]. Therefore, the negatively charged GNP was expected to diffuse faster through the overall negatively charged hydrogel composite matrix, due to electrostatic repulsion. However, the presence of collagen in the composite created positive domains in the matrix that slowed down the diffusion of negatively charged GNP. Positively charged GNPs, on the other hand, interacted considerably with GelMA (the major component of the composite), resulting in a small diffusion coefficient. In the case of neutral particles, their interaction with the collagen network was small, leading to fast diffusion through the hydrogel matrix.

3.4.2. Encapsulation of Breast Cancer Cells in Hydrogel Composite

In 2D models, cells are cultured in flat plates, forming a monolayer. While 2D systems have been used extensively, the translation of *in vitro* results of nanoparticle transport obtained in 2D model systems to 3D real tumors is not promising [37]. In a 2D model, cells are exposed to a uniform concentration of GNPs, allowing for fast uptake. On the other hand, 3D models where cells are encapsulated in a hydrogel matrix mimics more closely the 3D architecture of an *in vivo* tumor. In addition, delivery of GNPs in 3D *in vitro* models relies on diffusion, showing a closer resemblance to *in vivo* transport. **Figure 3.3** shows 3D models created using two different breast cancer cell lines, estrogen-receptor-positive MCF-7 and triple-negative MDA-MB-231, encapsulated in the hydrogel composite matrix.

Cell viability was assessed by PrestoBlue assay on days 1, 4, 7, and 9. The cell viability measurement performed on day 7 was prior to the incubation of the hydrogel pellets with GNP solution. The measurement performed on day 9 was after incubation with GNP. The selected samples used for the performance of cell viability on day 9 were not used for TEM or ICP-MS. Increase in cell viability and proliferation was observed for both cell lines (Appendix B).

LIVE/DEAD assays were performed on day 7, in order to guarantee that the cells encapsulated in the hydrogel matrix (3D model) were viable. Both cell lines, MCF-7 (**Figure 3.3(a)**). and MDA-MB-231 (**Figure 3.3(b)**), displayed the formation of clusters containing viable cells and mostly alive. Staining of actin filament and DNA illustrated the formation of round clusters with disorganized nuclei for MCF-7 cells, while MDA-MB-231 displayed the formation of stellate projections, as seen previously [178].

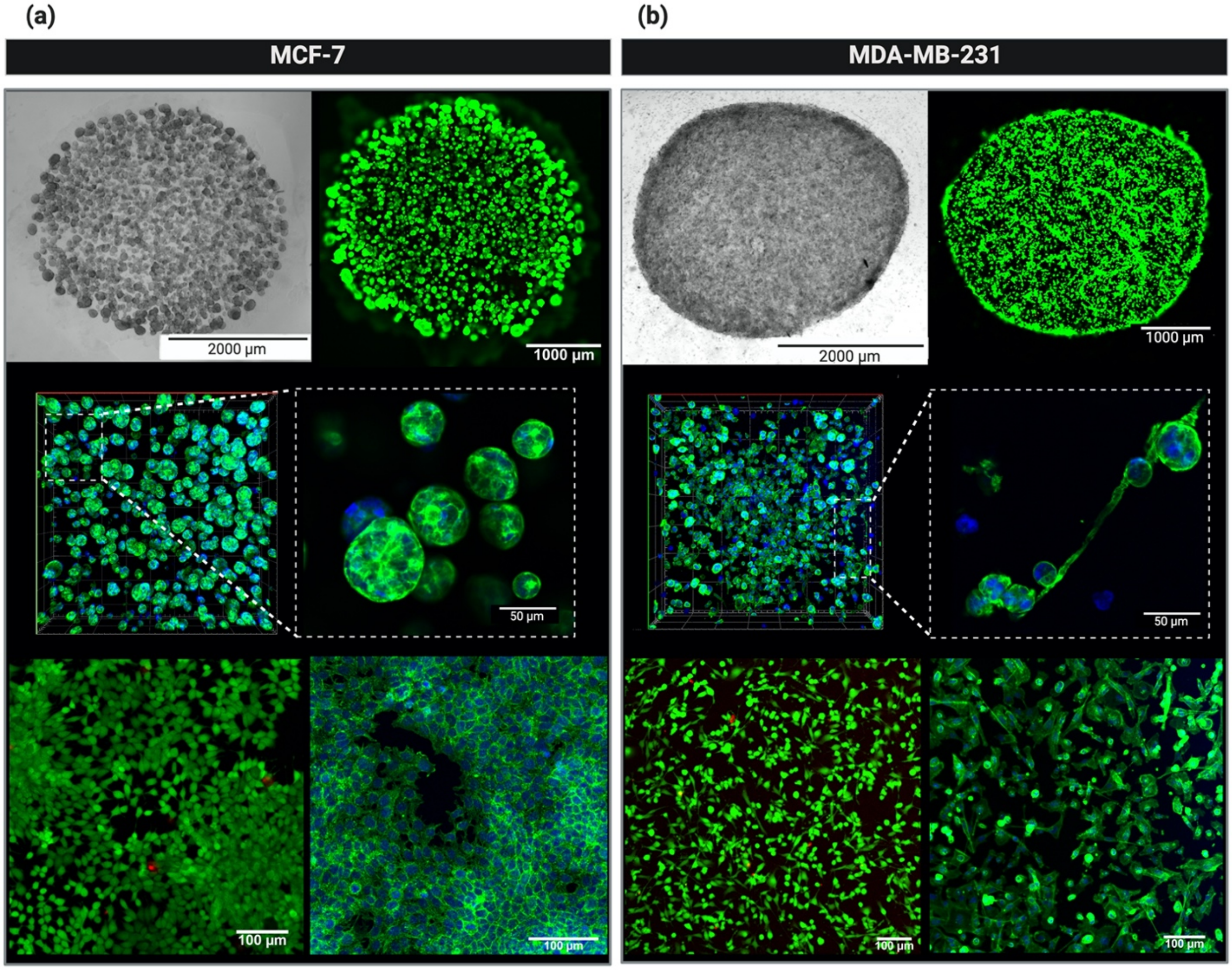

Figure 3.3 Breast Cancer Cells Encapsulated in Hydrogel Matrix
MCF-7 (a) and MDA-MB-231 (b) breast cancer cells were encapsulated in a hydrogel composite matrix composed of 1 mg/mL Collagen type I and 11.25% (w/v) Gelatin Methacryloyl. Pellets of hydrogel loaded with cells were formed by dispensing 10 µL of hydrogel/cell mixture and exposing it to 365 nm UV light for 4 minutes. Cells were allowed to grow in the hydrogel for 1 week, forming clusters within matrix Bright field images (top left, (a) and (b)) illustrate the growth and cluster formation of cells, while fluorescent images (top right, (a) and (b)) display live cells in green and dead cells in red, after staining with Calcein AM and Ethidium Homodimer-1. Fluorescent labeling of F-actin and nuclei (middle (a) and (b) images) with Alexa Fluor 488 and DAPI, respectively, illustrates the morphology and cluster formation of the breast cancer cells. Cell monolayers images (bottom (a) and (b) images) illustrate the morphology of breast cancer cell lines in 2D models.

3.4.3. Gold Nanoparticles Uptake: Qualitative Investigation

Cells encapsulated in hydrogel pellets were allowed to grow for 7 days. On day 7, the 3D hydrogel samples were immersed in 2 mL of a cell media solution containing 1x10^{12} GNP/mL and incubated for 48 h. As illustrated in **Figure 3.4**, after 48 h, the cell-loaded hydrogels were fixed and processed for qualitative (TEM) and quantitative (ICP-MS) evaluation of the uptake of GNPs.

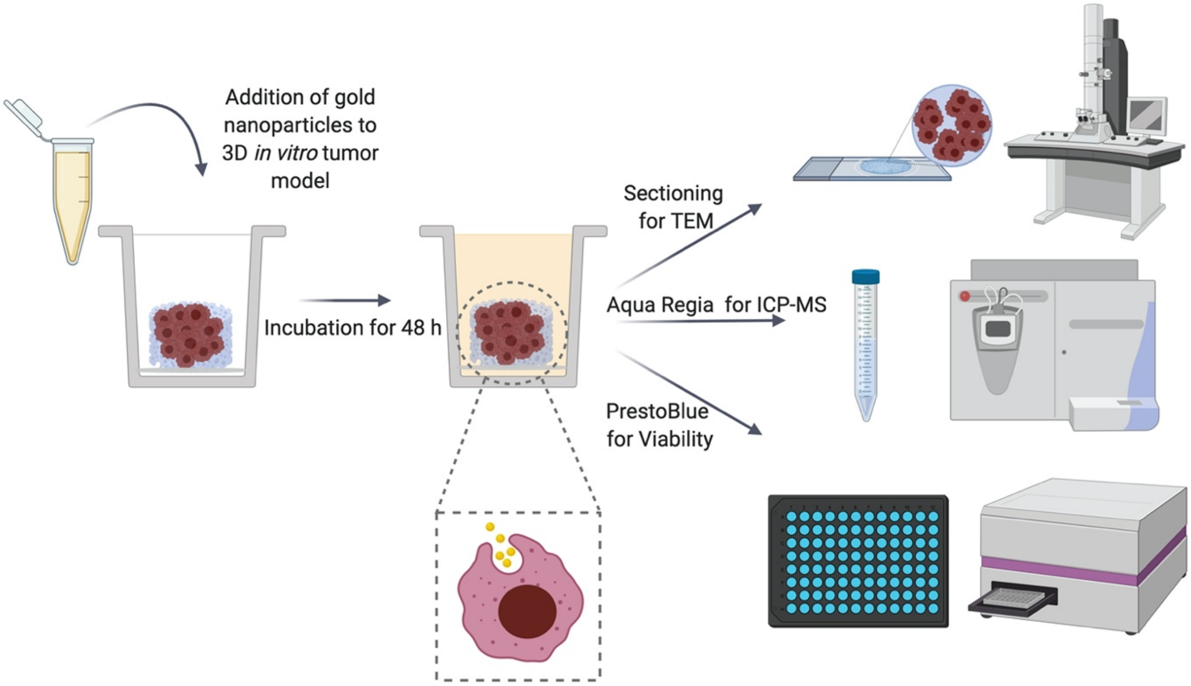

Figure 3.4 Qualitative and Quantitative Analysis of Cellular Uptake of Gold Nanoparticles A solution of gold nanoparticles with different surface charges was added to the 3D breast cancer *in vitro* models, followed by 48 h incubation at 37 °C. After 48 h, a third of the *in vitro* models were prepared for TEM sectioning (qualitative data), while another third was digested by aqua regia and analyzed by ICP-MS (quantitative data), and the last third was used for assessing cell viability.

Figure 3.5 shows TEM images of the sections obtained from each hydrogel samples were used to observe the presence of GNP. A small number of particles were seen for both cell lines when in contact with neutral GNP (**Figure 3.5(a)**). In the case of negatively and positively charged particles, a higher number of these GNPs was observed in both cell lines. Although a higher cellular uptake of positive particles is in agreement with previous studies [203, 204], quantitative information cannot be assessed from TEM images.

3.4.4. Gold Nanoparticles Uptake: Quantitative Investigation

Quantitative analysis of amount of gold (Au) present in the cell-loaded hydrogel pellets was performed by ICP-MS. Cell-loaded hydrogel samples were incubated with GNP at a final concentration of 1 x 10^{12} particles/mL for 48 h. After 48 h, samples were fixed and detached from the coverslips. The masses of the 3D hydrogel samples were recorded, followed by digestion in aqua regia.

Digested 3D hydrogel samples were submitted to ICP-MS and the results were obtained in parts per billion (ppb) of Au. Two types of controls were used for this experiment: 3D hydrogel samples incubated with GNP in the absence of cancer cells and hydrogel samples in the presence of cancer cells but no GNP. The former control provided information regarding particles trapped in the hydrogel matrix without cellular uptake. The later provided the background value for the samples. In addition, 4% (v/v) aqua regia with deionized water were also analyzed in order to account for any impurities in the samples.

The concentration of gold per gram of hydrogel was obtained by dividing the gold amount in ppb obtained by ICP-MS by the mass of the 3D cell-loaded hydrogel sample incubated with GNPs, as described in Section 2.8. In addition, values in ppb/g for controls were subtracted from the specific 3D cell-loaded hydrogel sample, depending on the charge of the GNP (Appendix B). **Figure 3.5(b)** summarizes the results for GNP uptake for all different surface charges and for the two different cell lines investigated (MCF-7 and MDA-MB-231). A similar trend for cellular uptake of GNP was observed for both cell lines. In both MCF-7 and MDA-MB-231 cell lines, the concentration of positively charged GNP was much higher than the values observed for negative and neutral particles.

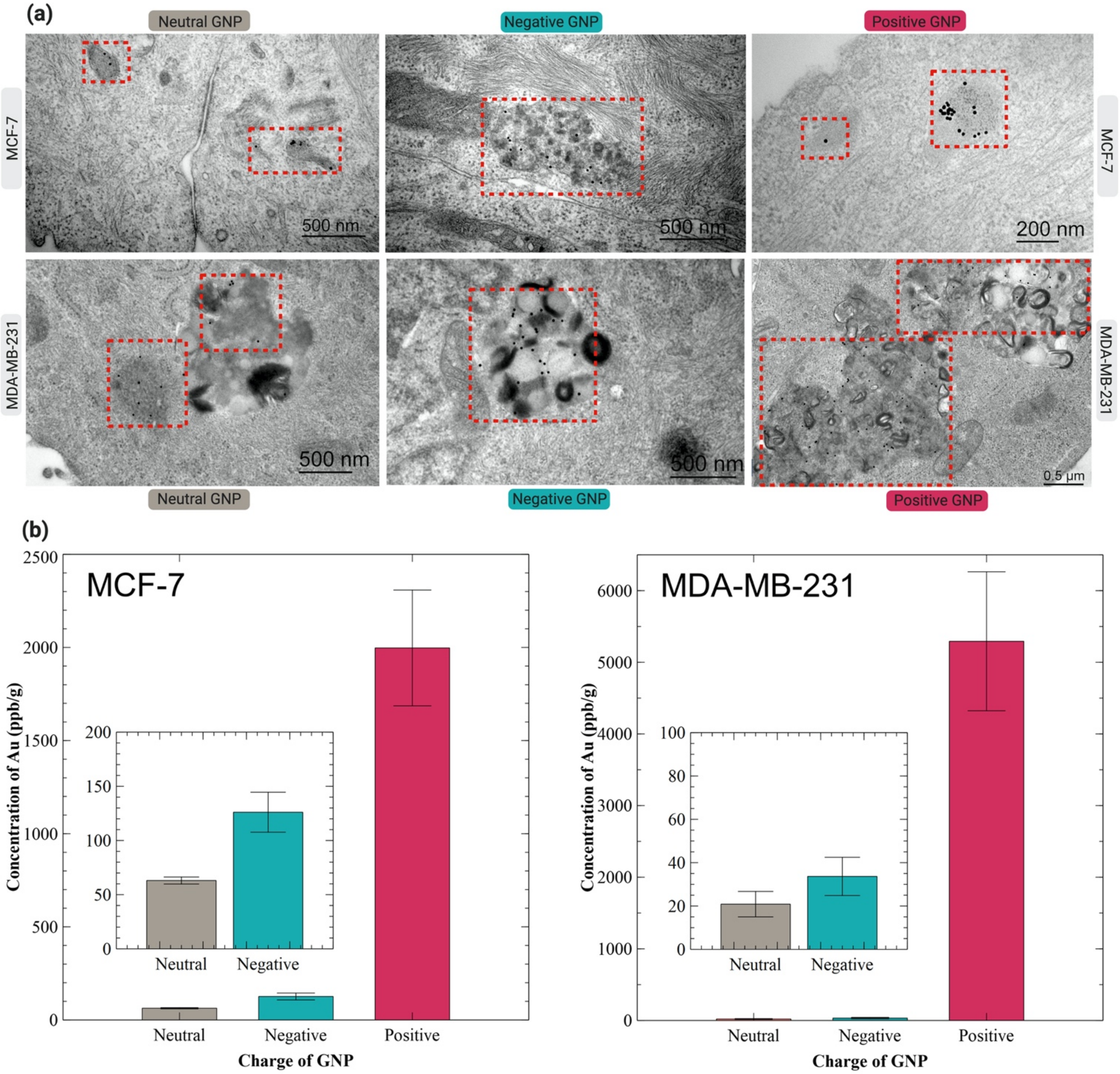

Figure 3.5 Cellular Uptake of Gold Nanoparticles
(a) TEM images of *in vitro* tumor model section containing neutral (left column), negative (middle column), and positive (right column) gold nanoparticles. Dashed red rectangles display the locations of the gold nanoparticles within the cells. (b) Concentration of GNP (ppb/g of *in vitro* tissue model) for neutral (gray), negative (green), and positive (red) gold nanoparticles contained in MCF- 7 (left) and MDA-MB-231 (right) *in vitro* model obtained by ICP-MS.

For MCF-7 cells, GNP concentrations of 63.07 ± 3.24 ppb/g, 126.09 ± 18.45 ppb/g, and 1997.28 ± 310.69 ppb/g were obtained for neutral, negative and positive particles, respectively. In the case of MDA-MB-231 cells, GNP concentration values of 20.86 ± 5.87 ppb/g, 33.66 ± 8.82 ppb/g, and 5293.34 ± 969.86 ppb/g were obtained for neutral, negative and positive GNP, respectively. High cellular uptake of positively charged particles was expected due to the electrostatic interaction with negatively charged cell membrane [205, 206]. Interestingly, a relatively higher cellular uptake was seen for negative particles than neutral, especially in the case of MCF-7 cells. This same trend was seen previously [207] for polymer-coated GNPs. Due to the complexity of the cell membrane [208], negative particles may interact with molecules such as proteins located at the surface of the cell membrane, facilitating their uptake [207, 209].

3.5. Conclusion

Gold nanoparticles show promising applications in cancer therapy, such as drug delivery carriers, photothermal agents and radiation sensitizers. Successful delivery of gold nanoparticles to the tumor area depends not just on the size, shape, and surface charge of the particles, but also on the tumor microenvironment. A poorly organized vascularization system resulted from accelerate growth of cancer cells within healthy tissue creates an increase in interstitial pressure, limiting the transport of therapies to diffusion. While large particles may be able to reach the tumor area, due to their size, penetration through the ECM and tightly packed cells will be hindered, locating the particles at the periphery of the tumor [173, 210]. Small nanoparticles, on the other hand, can diffuse through the tumor microenvironment, permeating the ECM, and reaching the deeply into the tumor [211, 212].

In this study, we analyzed the transport and cellular uptake of small GNPs (10 nm) in a 3D *in vitro* model. GNPs with three different surface charges, neutral, negative, and positive were used. While the relationship between surface charge of GNPs and cellular uptake has been extensively studied in the literature, to our knowledge, the integration of quantitative diffusion in a 3D *in vitro* breast cancer model has not been done.

We have shown previously that our hydrogel composite composed of GelMA and Collagen type I displayed similar properties to real *in vivo* breast tumors [195]. In addition, diffusion studies previously obtained in our model showed similar coefficients to *in vivo* transport of Immunoglobulin G in murine mammary carcinoma [177, 195], illustrating the potential of the microfluidic platform and hydrogel composite as an alternative to *in vivo* models. Here, diffusion experiments were performed by injecting GNP samples in the lateral channels (capillary-mimicking) of the microfluidic device. Results of GNP diffusion through the hydrogel composite showed faster diffusion for neutral particles, followed by negative, and lastly positive GNPs. The decrease in diffusion coefficient from neutral particles compared with positive GPNs was around 61%.

Analysis of cellular uptake of GNPs was performed by TEM and ICP-MS. Breast cancer cells were encapsulated in the hydrogel composite, displaying the formation of spheroids. After 7 days of growth, 3D models were incubated with 1 x 10^{12} GNPs/mL for 48 h. After 48 h, samples were processed for ICP-MS and TEM. While no quantitative information was obtained from TEM, ICP-MS results showed very high cellular uptake of positive particles for both cell lines, in agreement with the literature. However, considering that the cell membrane is negatively charged, higher uptake of neutral particles was expected. Furthermore, it is possible that an interaction between surface proteins at the cell membrane and neutral particles may be happening.

Nevertheless, the comparison between diffusion data and cellular uptake analysis showed interesting results. While positively charged particles displayed the slowest diffusion, the highest cellular uptake was obtained for these GNPs. In the case of neutral particles, lowest cellular uptake was obtained for these GNPs, while they displayed fastest diffusion. These results elucidate the need for complex 3D models, with appropriated charged ECM-mimicking biomaterial. In addition, the study of cellular uptake in 2D cell models does not display a realistic concentration gradient for mass transfer as seen in real tissue [213].

Chapter 4 Synthesis and Fabrication of pH-Responsive Gelatin Methacryloyl Microspheres*

Karolina P. Valente [1], Cameron Polglase [2], Roman G. Belli [3], Elaina Bourque [3], Afzal Suleman [1], Alexandre G. Brolo [3]

[1] Department of Mechanical Engineering, University of Victoria, Victoria, BC, Canada.
[2] Department of Biomedical Engineering, University of Victoria, Victoria, BC, Canada
[3] Department of Chemistry, University of Victoria, Victoria, BC, Canada.

*Manuscript to be submitted to Nanoscale (RSC).

Keywords:

pH-Responsive Hydrogel, Gelatin Methacryloyl, Hydrogel Microspheres, Flow focusing Microfluidic Device, Drug Delivery Systems

Author contribution:

Karolina P. Valente designed, set-up and performed most of the experimental procedures, analysis and preparation of manuscript. Cameron Polglase performed some of the experiments and edited the manuscript. Roman G. Belli analyzed ^{1}H NMR data. Elaina Bourque performed some of the experiments. Afzal Suleman and Alexandre G. Brolo provided feedback on the experimental analysis and edited the manuscript.

4.1. Abstract

pH-Responsive hydrogels have numerous applications in tissue engineering, drug delivery systems, and diagnostics. Gelatin Methacryloyl is a biocompatible, semi-synthetic hydrogel prepared from gelatin. Due to the presence of different functional groups (amine, hydroxyl, and carboxyl), GelMA can be produced with different degrees of substitution. Although GelMA has extensive applications in biomedical engineering, the synthesis of this polymer has never been tuned towards producing a pH-responsive hydrogel. In this work, we have explored two different synthetic routes in order to produce two GelMA-based hydrogels: polymer A and polymer B. Polymers A and B were used to fabricate GelMA microspheres in a flow-focusing microfluidic device. At neutral pH, polymers A and B microspheres displayed an average diameter of ~ 40 µm. At pH 6, microspheres from polymer A showed a swelling ratio of 167%, while at pH 10, a 296% swelling ratio was recorded for polymer B particles.

4.2. Introduction

Hydrogels are three-dimensional networks composed of polymeric materials (natural or synthetic) that are capable of absorbing a considerable amount of water and swelling in aqueous medium, while maintaining physical integrity due to the presence of hydrophilic functional groups (-OH, -COOH, -SO_3H and $CONH_2$) [21]. Hydrogels have been extensively applied in the field of tissue engineering [214–217] and as drug delivery systems [218–220] due to their biocompatibility and resemblance to a natural tissue.

Depending on the properties of the functional groups present on the polymeric chains, some hydrogels can respond to specific environmental changes such as temperature, light, and pH [221]. In the case of pH-responsive hydrogels, polymers containing acidic and basic pendants can accept or release protons according to the pH of the solution [222]. For hydrogels containing carboxyl groups, they become negatively charged at high pH values, forming anionic polyelectrolytes. Amine groups, on the other hand, become positively charged at low pH values. Applications of pH-responsive hydrogels are numerous, ranging from controlled drug carriers and delivery systems to sensors [223–226].

Responsive hydrogels possessing basic functional groups can be applied as drug delivery vehicles to cancerous environment. Growth of cancer cells within a healthy tissue culminates in remodeling of the tissue environment, resulting in stiffening of the extracellular matrix and an increase of interstitial pressure [37]. The latter combined with the disorganized structure of the tumor area affects the clearance of waste products [45], leading to a decrease in pH in the tumor area to values as low as 5.6 [227]. Therefore, pH responsive cationic hydrogels are expected to release molecular cargos in the tumor area by swelling due to the acidic environment [228–230].

Anionic hydrogels, on the other hand, have been applied as oral delivery systems, since they overcome the acidic condition in the stomach to deliver drugs to the small intestine [231–233].

Gelatin is a natural polymer originated from collagen, derived through a denaturation process. Either gelatin type A or gelatin type B are obtained depending on the denaturation type (acidic or basic treatment) [234]. Gelatin Methacryloyl is a semi-synthetic biomaterial prepared from the addition of methacrylate (reaction with methacrylic anhydride [149, 235]) and methacrylamide (reaction with glycidyl methacrylate [236]) groups in gelatin. The presence of arginine-glycine-aspartic acid (RGD) sequences on the gelatin backbone of GelMA promotes cell attachment and results in a biomaterial suitable for a variety of biomedical applications [109, 237]. While most of the GelMA synthesis protocols focus on the reaction between methacrylate groups and amino residues, resulting in the decrease of free lysine groups [110, 235], certain conditions favors reaction involving hydroxyl and carboxyl groups in the gelatin backbone with methacryl groups [238].

This work reports the synthesis of two GelMA-based polymers (Polymers A and B) that presented pH-dependent swelling behavior. The presence of carboxyl, hydroxyl and amino groups on the gelatin backbone [109, 110, 239] allows selective modification with methacryl groups. In the case of polymer A, the synthesis of GelMA was modified in order to maintain available amine groups, while reacting hydroxyl and carboxyl groups with glycidyl methacrylate. On the other hand, in the case of polymer B, amine groups were allowed to react with methacrylic anhydride, while carboxyl and hydroxyl groups remained unreacted. Microspheres of polymers A and B were produced using a flow-focusing microfluidic device and mineral oil/span 80 as the continuous phase. The behavior of the GelMA-based microspheres in solutions of different pH values was determined by quantifying the degree of pH-dependent volume changes.

4.3. Materials and Methods

4.3.1. Materials

Gelatin from porcine skin (Type A, gel strength 300), gelatin from bovine skin (Type B), methacrylic anhydride (MAA) (contains 2000 ppm topanol A as inhibitor, 94%), glycidyl methacrylate (GMA) (≥ 97%), 2-hydroxy-4’-(2-hydroxyethoxy)-2-methylpropiophenone (Irgacure 2959, 98%), Span 80 (nonionic surfactant), and Mineral Oil (light), Phosphate Buffer Solution (PBS, pH 7.4) were purchased from Sigma-Aldrich. Tetrahydrofuran (THF, 99.9%), hydrochloric acid (36.5-38.0%), and Dialysis Membrane Tubing (12,000 to 14,000 Dalton MWCO) were purchased from Fisher Scientific. Fluorescent Carboxylated PS Latex Particles (CAF-100nm) were purchased from Magsphere Inc. SU-8 and SU-8 developer were purchased from Kayaku Advanced Materials. Sylgard 184 Silicone Elastomer Kit was purchased from Dow Corning. Silicon wafers (76.2 mm, P-type, Boron) were purchased from Silicon Materials Inc.

4.3.2. Synthesis of Polymers A and B

Polymer A was synthesized from gelatin type A and glycidyl methacrylate (GMA). As illustrated by **Figure 4.1**, the reaction was performed in a water bath at 40°C. Initially, 2.5 g of gelatin type A was dissolved in 125 mL of acidic water with HCl (pH 3.5) in a round-bottom flask while stirring at 400 rpm. After all gelatin A was dissolved, 5 mL of glycidyl methacrylate was added dropwise (rate 0.5 mL/min) to the solution. The pH of the mixture was adjusted back to 3.5 every 30 min using HCl throughout the reaction. 50 mL of pH 3.5 water was added to the mixture after 18 h and the reaction continued for an additional 6 h. After the total reaction time of 24 h, 100 mL of acidic water was added to the round-bottom flask and the mixture was allowed to stir for additional 10 minutes. The solution was then transferred to dialysis membranes in order to eliminate unreacted glycidyl methacrylate. Dialysis was performed for one week at 40 °C, followed by freezing at -80°C and lyophilization to obtain the dry product polymer A.

Polymer B was synthesized by the reaction between gelatin type B with methacrylic anhydride (MAA). As shown in **Figure 4.1**, 2.5 g of gelatin B was dissolved in 50 mL of PBS in a round bottom flask while stirring at 400 rpm. Once all gelatin B was dissolved, 2.0 mL of methacrylic anhydride was added dropwise (rate 0.5 mL/min) to the solution. The mixture was allowed to react for 3 h and the temperature was kept constant at 40°C by a water bath. After 3 h, 100 mL of PBS was added to the reaction mixture, followed by dialysis at 40 °C for one week, in order to eliminate unreacted methacrylic anhydride. The dry polymer B was finally isolated after freezing at -80°C and lyophilization.

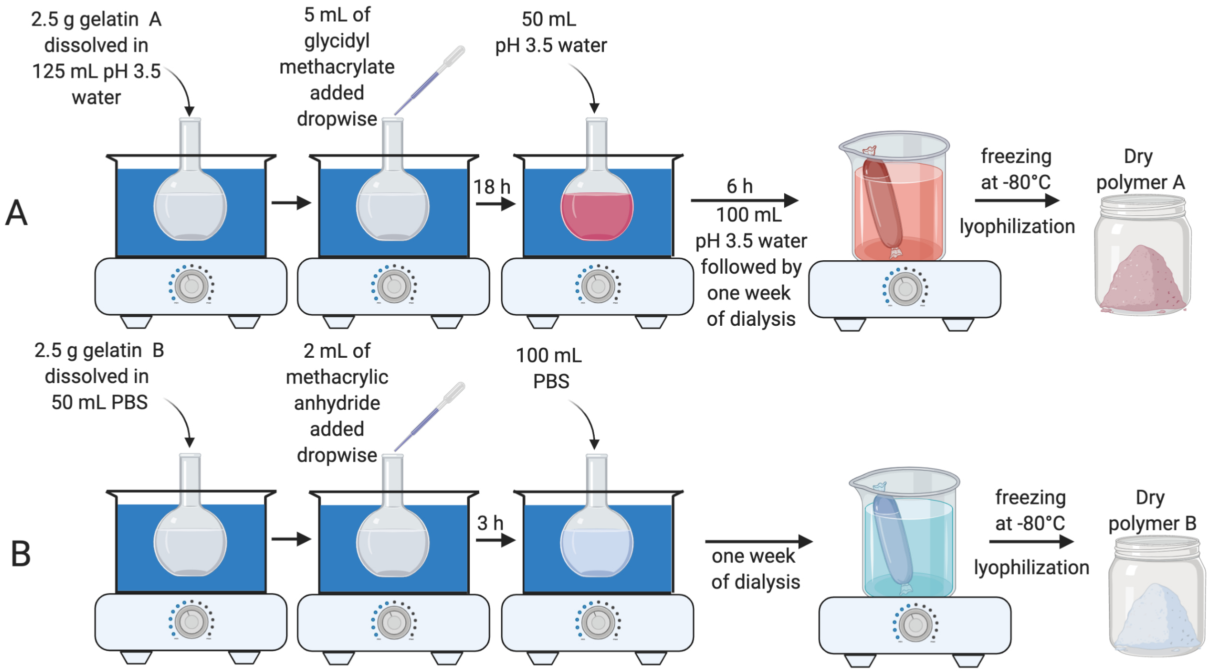

Figure 4.1 Synthesis of Polymers A and B
A) Polymer A was produced by reacting gelatin A with glycidyl methacrylate at pH 3.5. After a total reaction time of 24 h, 100 mL of pH 3.5 water was added to the solution. Solution was then transferred to dialysis membrane, followed by lyophilization to obtain polymer A. B) Polymer B was produced by reacting gelatin B with methacrylic anhydride. After a total reaction time of 3 h, 100 mL of PBS was added to the solution, followed by dialysis and lyophilization.

4.3.3. Characterization of Polymers A and B

^{1}H NMR experiments were recorded on a Bruker Avance 500 MHz spectrometer. Samples were dissolved in 1 mL of deuterium oxide (D_2O) containing 3-(trimethylsilyl)propionic-2,2,3,3,-d_4 acid (TMSP) as an internal standard (δ (^{1}H) = 0 ppm). The amount of methacryl groups (AM) in the samples were calculated as described previously [240]. Equation 4 was used to calculate the amount (in mmol per g of polymer sample) of methacryl groups (AM), while equation 5 was used to calculate the degree of methacrylation of lysine groups (DM_{lysine}) [241].

$$AM(mmol\ g^{-1}) = \frac{\int methacryl\ peaks}{\int TMSP} \times \frac{9H}{1H} \times \frac{mmol\ (TMSP)}{g\ (polymer\ sample)} \tag{4}$$

$$DS_{lysine} = \left(1 - \frac{\int lysine\ in\ polymer\ sample}{\int lysine\ in\ gelatin}\right) \times 100\% \tag{5}$$

4.3.4. Fabrication of Microfluidic Device

A flow-focusing microfluidic device was fabricated using standard photolithography. Briefly, SU-8 was spin coated on the surface a silicon wafer to a final thickness of 150 µm. The wafer was then soft baked at 65°C for 30 min and then for 60 min at 95°C. Using a photolithography mask, the flow-focusing design was patterned on the SU-8 layer by exposing it to UV light. The patterned wafer was post-baked at 95°C for 90 min, followed by a development step using SU-8 developer. Polydimethylsiloxane (PDMS) was prepared by 10:1 (w/w) mixture of silicone elastomer base and curing agent. PDMS was then deposited at the surface of the SU-8 patterned silicon wafer. After degassing in a vacuum chamber, the assembly was baked at 100°C for 3 h, to allow PDMS polymerization and hardening. After 3 h, the PDMS was then peeled off from the wafer and holes were punched in the inlets and outlets of the channels. The PDMS layer was permanently bonded to a glass slide using plasma cleaning. The chips were then baked at 60°C for at least 3 h in order to allow hydrophobicity to be restored in the PDMS channels. The design of the microfluidic device consisted of an inner channel for the dispersed phase and two outer channels for the continuous phase.

4.3.5. Synthesis and Characterization of Hydrogel Microspheres

Hydrogel microspheres were produced in a flow-focusing microfluidic device. A solution containing 5% (w/v) of polymer A or B was prepared in 0.5% (w/v) of irgacure 2959 in PBS. This solution was used as the dispersed phase inside the microfluidic device. The continuous phase was composed of a 4:1 (w/w) ratio of mineral oil (16.8 g):Span 80 (4.2 g). Flow rates of 1 µL/min and 20 µL/min were used for dispersed and continuous phases, respectively. The outlet tubing was cut to two meters total length and positioned in a 3D printed support, creating a meander. A 365 nm UV light was located on top of the meander, allowing microspheres leaving the microfluidic device to be exposed to UV light for 10 min before being collected. After collection, the microspheres were allowed to stabilize for 12 h at room temperature and in the dark. A volume of 0.5 mL of solution containing the microspheres was washed by using 1 mL of THF, followed by centrifugation for 7 min at 8,000 rpm. This washing procedure was repeated three times. The microspheres were then stored in 0.5 mL of PBS prior to use, to a final concentration of $2x10^6$ microspheres/mL. In order to generate fluorescently labeled microspheres, 20 µL of fluorescent polystyrene nanoparticles were added to a 0.5 mL hydrogel solution of Polymer A or B and the synthesis proceeded as described above.

The impact of pH on the diameter of the microspheres was investigated by incubating 200 µL of particle suspensions in 1 mL of aqueous solutions with pH of 6, 7.4, and 10 for 2 h. The change in diameter was observed using the bright field camera on the Laser Scanning Microscope (Zeiss LSM 880). In the case of the microspheres containing polystyrene nanoparticles, fluorescent images were taken with the LSM. The excitation was at 543 nm (helium-neon laser, 40% laser power) and the emission band covered the range between 560 and 700 nm. Images were collected at a frame size of 0.35 µm x 0.35 µm (4096 pixels x 4096 pixels), pixel time of 1.03 µs, and a frame time of 162.32 s using an EC Plan-Neofluar 10x/0.30 M27 objective lens.

The diameter of 100 microspheres were measured for each experiment using the measure tool on Zen 2.3 software in both bright field and fluorescent images. The diameter of the particles was obtained by averaging the measurement for each experiment (100 particles) and calculating the standard deviation. The experiments were repeated three times from different batches of polymers A and B. The swelling ratio was calculated based on the fractional increase in volume presented previously [242], using equations 6 and 7 for swelling and shrinkage percentages for polymer A and B.

$$Q_{pH\ 6\ or\ 10-PBS} = \left(\frac{D_{pH\ 6}^{3} - D_{PBS}^{3}}{D_{PBS}^{3}}\right) \times 100\% \tag{6}$$

$$Q_{pH\ 10\ or\ 6-PBS} = \left(\frac{D_{pH\ 10}^{3} - D_{PBS}^{3}}{D_{PBS}^{3}}\right) \times 100\% \tag{7}$$

Where $D_{pH\ 6}$, $D_{pH\ 10}$, and D_{PBS} correspond to the diameter of the particles in pH 6, pH 10, and PBS, respectively.

4.4. Results and Discussion

4.4.1. Determination of Degree of Modification of Polymers A and B

Polymer A is a GelMA-based material that expands in acidic environment due to the presence of free amine groups that ionize at low pH values. Polymer A was synthesized by reacting gelatin type A with glycidyl methacrylate at pH 3.5 (see experimental section for a detailed description of the synthesis and **Figure 4.2B**). It has been shown that in acidic conditions, glycidyl methacrylate reacts with hydroxyl and carboxylic acid groups of polymers through an epoxide ring-opening route [240]. This route leads to the formation of 3-methacryloyl-1-glycerylester (GMA1) and 3-methacryloyl-2-glycerylester (GMA2). GMA1 and GMA2 attacks the carboxyl and hydroxyl groups of the gelatin A backbone, as indicated in **Figure 4.2B**. The presence of GMA1 and GMA2 fragments in polymer A was verified by ^{1}H NMR presented in **Figure 4.2C**. The overlapping NMR signals observed at 6.18 and 5.76 ppm (indicated in the green region in **Figure 4.2C**) correspond to the geminal vinyl hydrogens of GMA1 and GMA2. The additional peak at 2.07 ppm seen in **Figure 4.2C** (pink region) is associated to the methyl carbon-linked hydrogens at the vinyl carbon, which also confirms the modification of the polymer backbone by GMA.

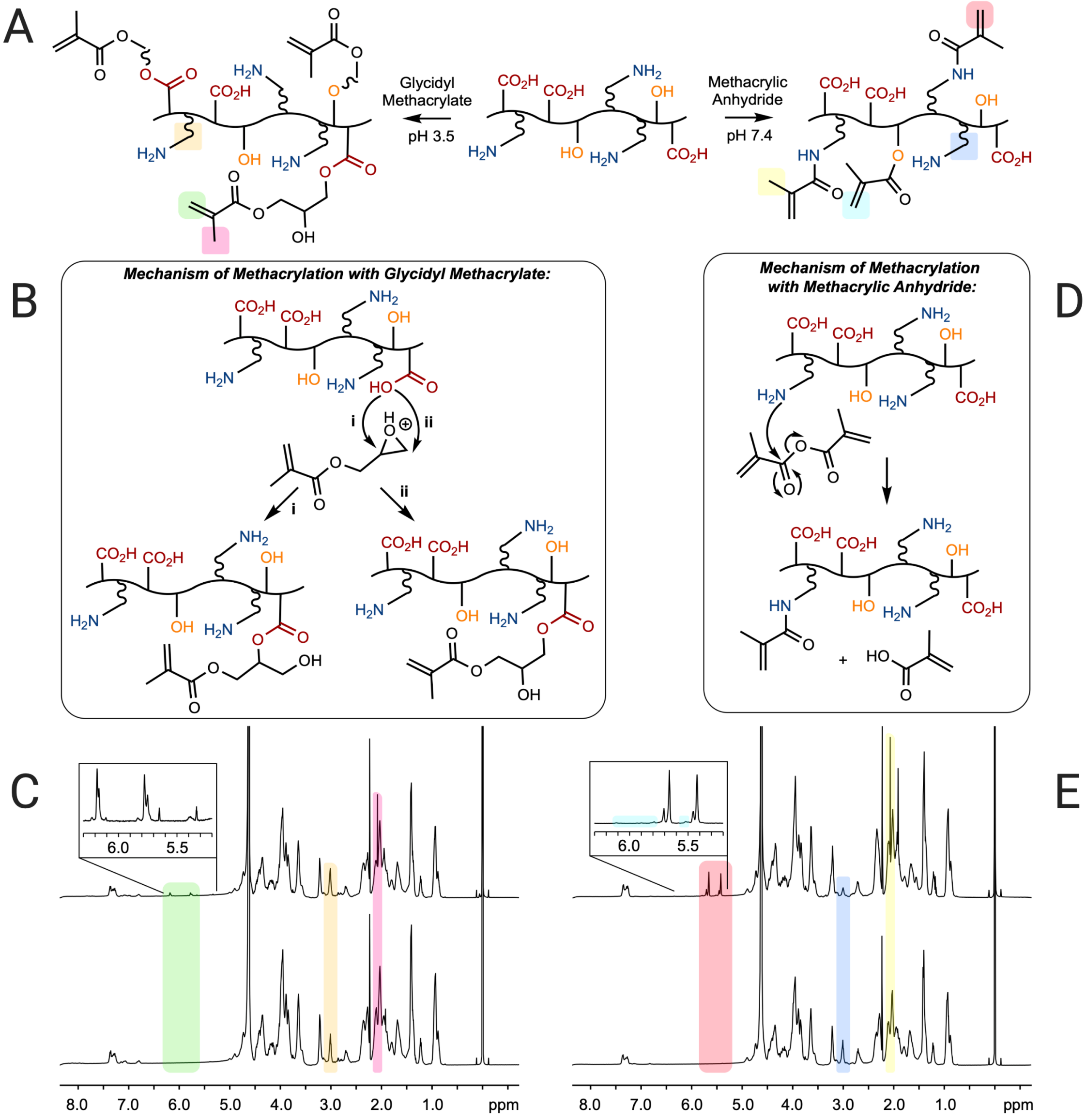

Figure 4.2 Synthesis of Polymers A and B

A) Two synthesis routes from gelatin. The reaction of gelatin with glycidyl methacrylate at pH 3.5 produced polymer A (left), while the reaction with methacrylic anhydride at pH 7.4 generated polymer B (right). B) Mechanism of methacrylation of gelatin type A with glycidyl methacrylate through ring-opening reaction. C) ^{1}H NMR spectra of polymer A (top) and gelatin type A (bottom). D) Mechanism of methacrylation of gelatin type B with methacrylic anhydride. E) ^{1}H NMR spectra of polymer B (top) and gelatin type B (bottom).

The extension of the chemical modification was 0.103 mmol of methacryl group/g of polymer A, obtained using equation 4. The integration of the peak at 6.18 ppm (green region in **Figure 4.2C**) takes into account the total amount of methacryl groups, including GMA1 and GMA2, in polymer A.

Additional peaks were also seen within the green region of **Figure 4.2C**(inset) at 5.33 and 5.65 ppm. While these peaks could be an indication of a side reactions involving GMA and the amine groups in the polymer backbone, amine-epoxy reactions are expected to display NMR signatures correspondent to the vinyl groups at 6.2-5.8 ppm which are not observed in **Figure 4.2C** [243] In addition, the DM_{lysine} values calculated from the integration of lysine peaks at 3.00 ppm were around 0%. Therefore, the small peaks at 5.33 and 5.65 ppm in **Figure 4.2C** are assigned to impurities from either GMA or D_2O.

The polymer B synthesis involved the reaction between gelatin type B with methacrylic anhydride at pH 7.4, as indicated in **Figure 4.2D**. The conditions of the synthesis involved a higher pH value than the isoelectric point of gelatin type B (between 5 and 6) to favor a higher degree of methacrylation [238]. Methacrylic acid is a by-product as the reaction proceeds, which lowers the pH of the solution during the synthesis. Previous reports have indicated that pH readjust of the reaction mixture during the synthesis [239, 242] results in a stiffer hydrogel. Therefore, the synthesis of polymer B was performed here (**Figure 4.2D**) without further pH adjustment. **Figure 4.2E** shows ^1H NMR data that confirms the formation of the desired product. The decrease in the lysine peak at 3.00 ppm (blue region in **Figure 4.2E**) indicates the functionalization of the free amine groups of the gelatin B precursor. In addition, **Figure 4.2E** display prominent peaks at 5.65 and 5.42 ppm (pink region) which are assigned to methacrylamide groups. Additionally, the peak at 2.07 ppm in the NMR spectrum of polymer B (yellow region in **Figure 4.2E**) can be associated to the methyl carbon-linked hydrogens at the methacryl group, confirming the reaction with MAA. The small peak at 6.11 ppm suggests the MAA reaction with hydroxyl (methacrylate) groups, although the other methacrylate vinyl proton is overlapped with the 5.65 ppm for methacrylamide peak (**Figure 4.2E**). The integration of the peak at 5.65 ppm represents then the total amount of methacryl groups present in polymer B.

The DM_{lysine} value, obtained from the integration of the lysine peak at 3.00 ppm, was 58%. This relative low DM value is due to the formation of methacrylic acid during the synthesis, which lowers the pH, resulting in a lower DS value. Values of 0.227 mmol of methacryl/g of polymer B and 0.062 mmol of methacrylate/g of polymer B were obtained from the integration of the peaks at 5.65 ppm (methacrylate and methacrylamide) and at 6.11 ppm, respectively.

4.4.2. Fabrication of Hydrogel Microspheres

A flow-focusing microfluidic device, presented in **Figure 4.3A**, was used for the fabrication of hydrogel microspheres. In the inner channel of the microfluidic device, a solution containing 5% (w/v) polymer solution (either polymer A or polymer B) with 0.5% (w/v) irgacure 2959 (photoinitiator) moved at a rate of 1 μL/min. GelMA-based solutions are highly viscous at room temperature; therefore, a controlled chamber was created around the syringe pump and tubing to maintain the solution temperature at 40 °C during the flow. The mineral oil/span 80 mixture was injected in the outer channels of the device (**Figure 4.3B**). When the two immiscible phases flow into a cross-junction, a flow-focusing region is created in which a stream of the dispersed phase is developed. The dispersed phase is then broken into spherical particles due to shear forces (high flow rate of continuous phase) and to perturbation in the flow [121, 122, 244] (**Figure 4.3C**). The surfactant (span 80) was added to the mineral oil to preclude aggregation of the microspheres inside the microfluidic device.

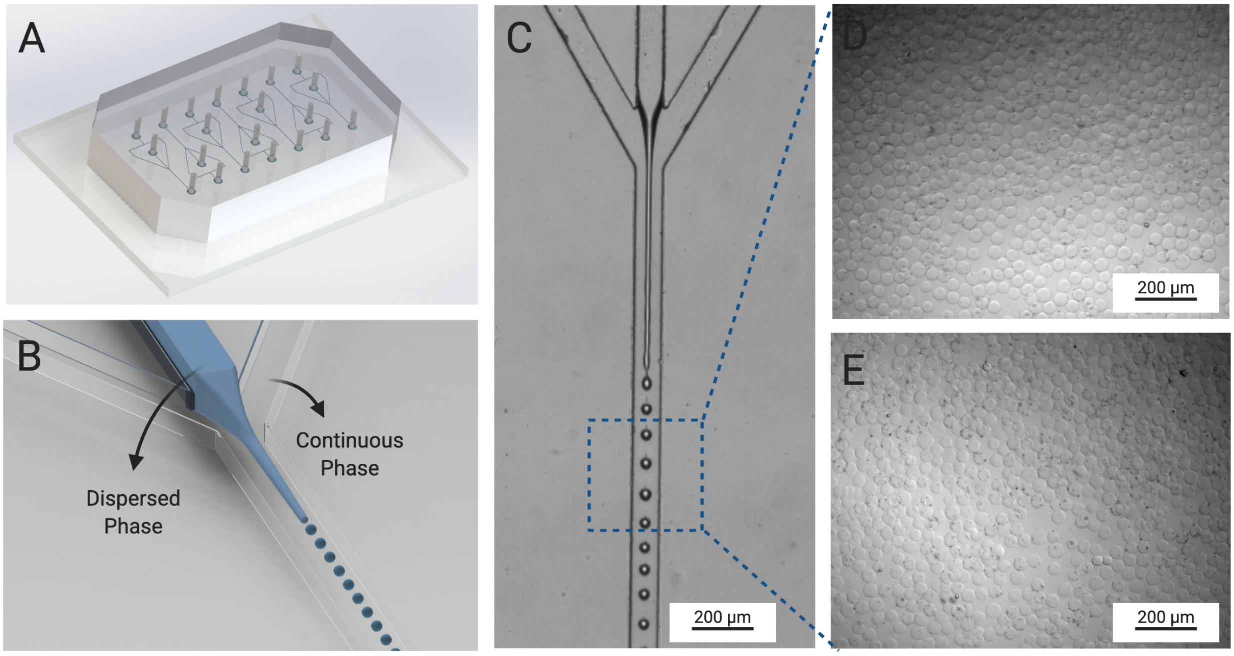

Figure 4.3 Fabrication of GelMA Microspheres
A) Microspheres were fabricated inside of a flow-focusing microfluidic. B) The device contained two phases (continuous and dispersed). Continuous phase was composed of 5%(w/v) GelMA (polymer A or B), while the dispersed phase consisted of mineral oil with span 80. C) Flow profile during production of microspheres. D) Polymer A microspheres. E) Polymer B microspheres.

GelMA microspheres leaving the outlet of the microfluidic device entered in a 2-meter meander tubing region that was exposed to UV light. The UV light activated the radical photoinitiator irgacure 2959 for 10 minutes that transformed the GelMA particles into crosslinked hydrogel microspheres. The hydrogel microspheres were then collected, stored, and allowed to stabilize overnight in the dark. The hydrogel microspheres were washed in THF to remove the oil/surfactant mixture and excess photoinitiator, kept in PBS solution for 24 h, and then used within 3 days. **Figure 4.3D** and **Figure 4.3E** show that the microspheres were uniform in size and shape, with diameters of 39.4 ± 2.6 µm and 38.6 ± 2.3 µm for particles produced from Polymers A and B, respectively.

4.4.3. Swelling and Shrinking Behavior of Hydrogel Microspheres

Hydrogels swell due to expansion of their hydrophilic cross-linked chains when in contact with an aqueous environment. Ionizable functional groups in the polymer chain can either accept or release protons in response to the pH of the environment. Polymer A synthesis was conducted at pH 3.5 so their amine groups were protonated, and therefore, unavailable to react with glycidyl methacrylate. Consequently, the hydroxyl and carboxyl groups of polymer A were modified by GMA1 and GMA2, while the amine groups remained unreacted. **Figure 4.4A** shows bright field images displaying the response of the hydrogel microspheres produced from polymer A when exposed to solutions of different pH values. Polymer A microspheres increase in diameter in acidic solutions and decrease in diameter in basic media. The swelling in acidic solutions can be explained by the protonation of amine groups, which creates repulsion between the polymer chains increasing the overall volume of the materials (**Figure 4.4A**). Swelling and de-swelling were also investigated by encapsulating red fluorescent PS nanoparticles in the polymer A solution prior to the production of the microspheres (**Figure 4.4B**). **Figure 4.4B** exposes a more obvious change in the particle diameter allowing for better visualization and quantification. De-swelling (shrinking) of polymer A microspheres was observed at pH 10. Polymer A microspheres displayed diameters of 39.4 ± 2.6 μm in pH 7.4, of 54.6 ± 3.0 μm in pH 6, and of 28.7 ± 1.6 μm in pH 10 (**Figure 4.5A**).

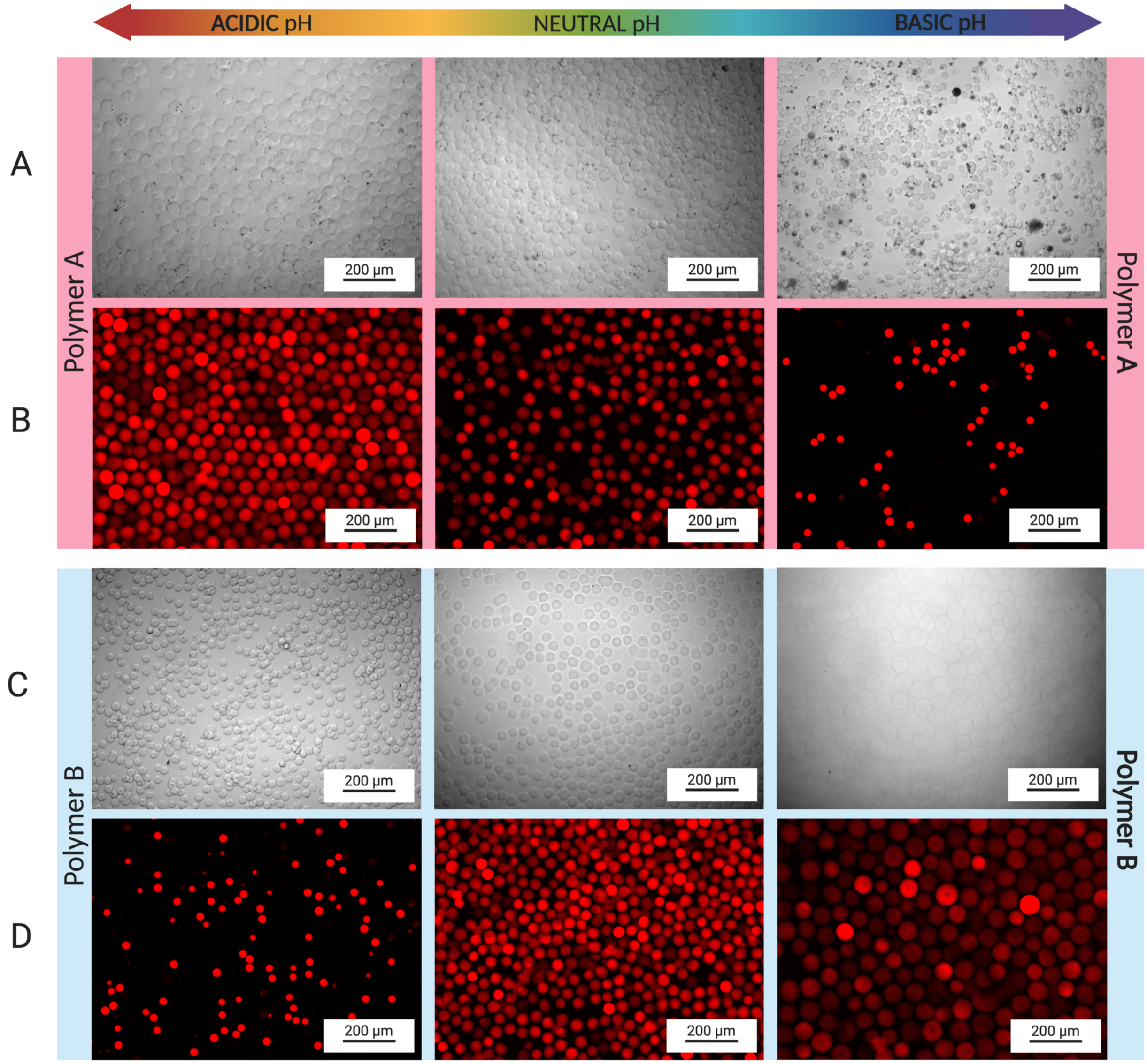

Figure 4.4 Swelling Behavior of GelMA Microspheres
A) Polymer A microspheres displayed swelling in acidic pH (6.0), while shrinkage was seen in basic pH(10). B) Swelling and shrinking of polymer A microspheres was also investigated by adding red-fluorescent PS nanoparticles to the hydrogel solution. The same swelling and de-swelling behavior was observed for the fluorescent microspheres. C) The opposite behavior was observed for polymer B microspheres, in which swelling was observed in basic pH, while shrinkage was seen in acid environment. D) Microspheres were also fabricated by adding PS particles to polymer B in order to better observe the increase and decrease in the diameter of the microspheres.

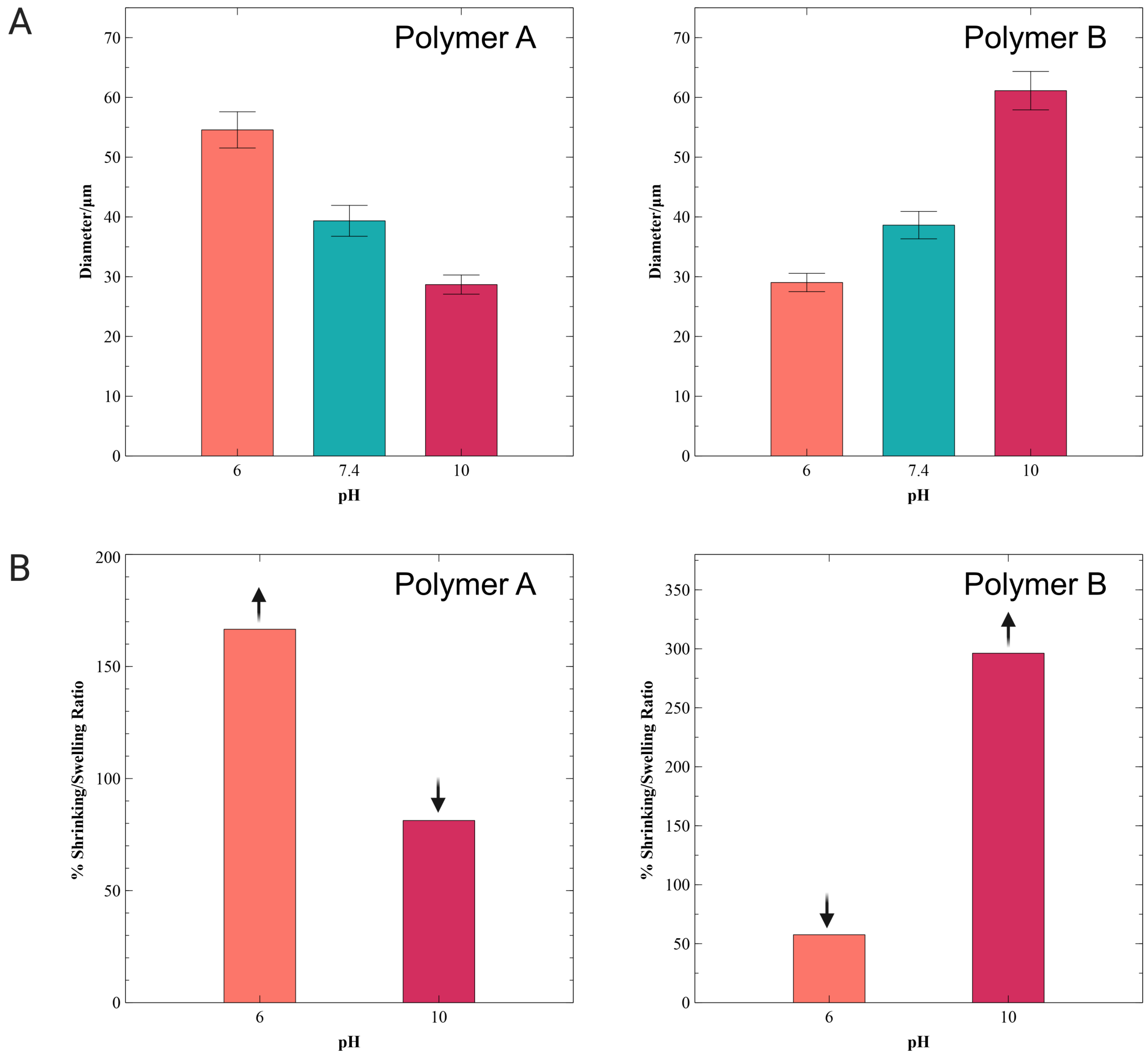

Figure 4.5 Swelling and De-swelling Behavior of Microspheres
A) Change in diameter was observed for polymers A and B, according to the pH of the environment. A decrease in diameter was seen with an increase in pH in the case of polymer A, while the opposite behavior was observed for polymer B (increase in diameter with increase in pH). B) Swelling ratios of 166.7% and 296.3% were obtained for polymers A and B, respectively, in pH 6 and pH 10. Shrinking ratios of 61.3% and 57.6% were observed for polymer A in pH 10 and for polymer B in pH 6, respectively.

Figure 4.5A summarizes the diameters of the hydrogel microspheres formed from both polymer A and polymer B, measured from the fluorescent images in **Figure 4.4**. **Figure 4.5B** are plots of volumes variation (swelling and de-swelling ratios) measured using the volume at pH = 7.4 as reference (100% value). The microspheres generated from polymer A displayed a swelling ratio of 167% at pH 6 and a shrinking ratio of 61% at pH 10 (**Figure 4.5B**).

The swelling behavior of hydrogel microspheres fabricated using polymer B is driven by the effect of free carboxyl groups. Although the DM_{lysine} of 58% implies that a good amount of amine remained unmodified at the polymer backbone, amino acid composition analysis has shown that gelatin B contains less lysine residues (per 1000 total amino acid) when compared to gelatin A [245]. In addition, gelatin type B displays a higher quantity of free carboxyl groups per 100 g of gelatin than type A [246]. Therefore, hydrogel microspheres formed from polymer B displayed swelling at basic medium due to the ionization of carboxylic groups in the backbone, which results in ionic repulsion within the polymer (**Figure 4.4B**). Similar to polymer A, the change in diameter of the polymer B microspheres was investigated using fluorescent PS particles in the polymer B solution (**Figure 4.4D**). A decrease in size was observed at pH 6. These microspheres exhibited diameters of 38.6 ± 2.3 μm in pH 7.4, of 29.0 ± 1.5 μm in pH 6, and of 61.1 ± 3.2 μm in pH 10 (**Figure 4.5A**). This resulted in 296% swelling and 58% de-swelling (**Figure 4.5B**). For both polymer A and B microspheres, in addition to the fast swelling and de-swelling process (< 2 h), we observed that swelling and shrinking were reversible.

4.5. Conclusions

Two synthetic routes for methacrylation of gelatin that produced the pH-responsive polymers A and B were reported. Microspheres from polymer A presented swelling and de-swelling at acidic and basic media, respectively, due to the presence of free amino groups. In the case of the microspheres produced from polymer B, even though not all amine groups were methacrylated, the presence of unreacted carboxyl groups resulted in an anionic hydrogel, displaying swelling at high pH values. Swelling and shrinking ratios of 167% and 61% were obtained for polymer A. In the case of polymer B, ratios of 296% and 58% were seen for swelling and de-swelling, respectively.

GelMA has shown to be an excellent biomaterial for tissue engineering [113, 247, 248], 3D printing [249–251] and drug delivery systems [252, 253]. The presence of RGD sequences in its gelatin backbone enhances cell attachment and biocompatibility. Although the diversity in functional groups on the gelatin backbone is well known, to our knowledge, they have not yet been explored in the fabrication of pH-responsive GelMA-based hydrogels. The swelling/de-swelling of GelMA-based microspheres showed in this study amplifies the application of this biomaterial as pH-responsive hydrogels, from drug delivery systems, to pH-responsive sensor applications.

Chapter 5 Preparation of Gold Nanoparticles-Loaded Gelatin Methacryloyl Nanogels: Nanocarriers for Drug Delivery Systems*

Karolina P. Valente [1], Cameron Polglase [2], Elaina Bourque [3], Roman G. Belli [3], Afzal Suleman [1], Alexandre G. Brolo [3]

[1] Department of Mechanical Engineering, University of Victoria, Victoria, BC, Canada.
[2] Department of Biomedical Engineering, University of Victoria, Victoria, BC, Canada
[3] Department of Chemistry, University of Victoria, Victoria, BC, Canada.

*Manuscript to be submitted to Nanoresearch (Springer).

Keywords:

Gold Nanoparticles, Nanogels, Microfluidics, Drug Delivery Systems, Hydrodynamic Flow focusing

Author contribution:

Karolina P. Valente designed, set-up and performed most of the experimental procedures, analysis and preparation of manuscript. Cameron Polglase performed some of the experiments and edited the manuscript. Elaina Bourque performed some of the experiments. Roman G. Belli analyzed ^1H NMR data. Afzal Suleman and Alexandre G. Brolo provided feedback on the experimental analysis and edited the manuscript.

5.1. Abstract

Polymeric nanoparticles have been employed in many biomedical applications, particularly in the field of drug delivery. Gelatin Methacryloyl is a semi-synthetic biocompatible hydrogel prepared from gelatin. In addition to high biocompatibility, its gelatin backbone is highly functionalizable, allowing for tunable chemical properties. In this study, a methodology for the fabrication of GelMA nanogels loaded with gold nanoparticles (GNPs) is described. The nanogels were prepared in a hydrodynamic flow focusing microfluidic device containing a polymeric stream and a nonsolvent phase. GNP-loaded GelMA nanogels (GNP@GelMA) were prepared at a concentration of 5 x 10^{12} nanogels/mL, displaying an average size of 65 ± 12 nm. The microfluidic technology offers highly controllable nanogel production that cannot be matched with bulk synthesis. In addition, due to their sizes, both the nanogels and the GNP displayed potential as drug delivery carriers in passive and active tumor extravasation.

5.2. Introduction

Hydrogels are three-dimensional polymer networks that swell in water due to the presence of hydrophilic functional groups (OH, COOH, SO_3H, and $CONH_2$) [21]. The biomedical applications of hydrogels extend from mimicking extracellular matrix in tissue engineering [113, 254, 255] to drug delivery systems [244, 252, 256]. Depending on the polymer, hydrogels can be natural, synthetic, or hybrid (semi-synthetic) [257]. Gelatin Methacryloyl is a photo-crosslinkable semi-synthetic hydrogel prepared by adding methacrylate and methacrylamide groups in the gelatin backbone [149]. The presence of arginine-glycine-aspartic acid (RGD) motifs and target sequences of matrix metalloproteinase (MMP) in gelatin promotes cell adhesion and cell remodeling [109, 258]. Considering that methacrylation of gelatin involves mainly amino and hydroxyl groups, RGD and MMP groups are not influenced, resulting in a biocompatible hydrogel that promotes cell adhesion and presents tunable physical properties [108, 259].

Hydrogels can be formulated into micro/nanoparticles, expanding their applications to drug delivery systems [260–262]. The microfluidic techniques provide the necessary tool for the development of polymeric particles of different sizes and shapes with narrow distributions [263]. Hydrogel microparticles are produced in microfluidics operating on dripping and jetting regimes, in which a dispersed phase is composed of the hydrogel solution while a continuous immiscible phase breaks the hydrogel into particles [120]. Nanogels, on the other hand, are fabricated due to the nanoprecipitation process. In this case, fast mixing of an outer nonsolvent phase with the polymer stream results in the formation of homogenous nanoparticles [264].

Nanoparticles have been extensively used as nanocarriers in nanomedicine to systematically deliver drugs to cancerous tissues [265–267]. The application of nanoparticles in the targeted delivery of drugs to cancer is due to a phenomenon known as enhanced permeability and retention (EPR) [268, 269]. The growth of solid tumors within heathy tissue results not just in an increase of interstitial pressure due to a poor lymphatic system, but also in fast sprouting of new blood vessels. The new vasculature system is disorganized, with blood vessels that are leaky due to the presence of endothelial gaps [270]. Particles circulating intravenously can escape circulation by moving through endothelial gaps and accumulate in the tumor area. After reaching the tumor, nanoparticles can then release a drug in the tumor cells, resulting in a targeted delivery system [271].

Efficient extravasation is dependent on particle size. Leaky vasculatures present pore sizes mostly below 400 nm, and therefore, nanoparticle dimensions must be below this cut-off size in order to perform an efficient extravasation [70]. However, the kidneys and liver also have an impact on the selection of the optimal nanoparticle size for drug delivery. Particles smaller than 10 nm undergo renal clearance, while the liver is capable of capturing particles above 100 nm [199, 200]. Therefore, the nanoparticle sizes that represent a compromise between efficient extravasation and minimal removal from natural processes are within the range of 10-100 nm.

Radiation therapy is a type of cancer treatment that relies on deposition of photons such as gamma and X-rays to effectively ionize biological matter. The drawback of this technique is that the dose deposition varies exponentially with tissue depth, resulting in a high radiation dose delivery to the healthy tissue located above the cancerous area [125]. The delivery of lower-energy radiation from multiple angles around the tumor and the use of radiosensitizers can minimize this problem. GNPs are a class of radiosensitizers that enhance the effect of radiation in tumors by local amplification of the dose [126].

Although a correlation between GNP size and radiation dose enhancement has been proposed [272, 273], the design of an efficient drug delivery system requires the combination of multiple parameters, including particle size, cellular uptake, dose enhancement and diffusion. The poorly organized vasculature combined with rapid proliferation of cancer cells increases the amount of pressure in the tissue, inhibiting distribution of large molecules by convection [43]. Therefore, the penetration of drugs and particles in to the tumor is limited by diffusion, decreasing the efficacy of systemic therapies in cancer [45]. While small particles diffuse faster and display a higher diffusion coefficient, movement of large particles is hindered by the ECM, and they are unable to diffuse efficiently through the tumor interstitial matrix [201].

In this work, the advantage of extravasation of large particles was combined with the high diffusivity of small nanoparticles into a hybrid material involving GelMA nanoparticles loaded with GNPs. GelMA nanoparticles were produced in a hydrodynamic flow focusing microfluidic device in the absence and in the presence of GNPs. This approach successfully demonstrated the synthesis of multiple GNPs entrapped in a GelMA nanogel suitable for EPR (~75 nm) using microfluidics. The simplicity of the synthesis of the nanogels combined with high throughput and high GNP loading provide a material that is suitable for enhanced radiotherapy and drug delivery.

5.3. Materials and Methods

5.3.1. Materials

Gelatin from porcine skin (Type A, gel strength 300), glycidyl methacrylate (≥ 97%), 2-hydroxy-4’-(2-hydroxyethoxy)-2-methylpropiophenone (Irgacure 2959, 98%), Span 80 (nonionic surfactant), and toluene, Phosphate Buffer Solution (PBS, pH 7.4) were purchased from Sigma-Aldrich. Tetrahydrofuran (THF, 99.9%), hydrochloric acid (36.5-38.0%), and Dialysis Membrane Tubing (12,000 to 14,000 Dalton MWCO) were purchased from Fisher Scientific. Accurate spherical 10 nm gold nanoparticles were purchased from Nanopartz. SU-8 and SU-8 developer were purchased from Kayaku Advanced Materials. Sylgard 184 Silicone Elastomer Kit was purchased from Dow Corning. Silicon wafers (76.2 mm, P-type, Boron) were purchased from Silicon Materials Inc. Formvar (200 mesh, copper) transmission electron microscope (TEM) grids were obtained from TED PELLA.

5.3.2. Synthesis and Characterization of Gelatin Methacryloyl

Synthesis procedure for GelMA (polymer A) has been described previously (Chapter 4). Briefly, 2.5 g of gelatin type A was dissolved in 125 mL of pH 3.5 water acidified with HCl while stirring at 400 rpm. A volume of 5 mL of glycidyl methacrylate was added dropwise to the gelatin solution. The reaction was conducted for 18 h, with pH adjustments every 30 min. A volume of 50 mL of pH 3.5 water with HCl was added to the mixture and the reaction continued for an additional 6 h. After a total of 24 h, 100 mL of pH 3.5 water with HCl was added to the solution. Dialysis was performed on the solution, followed by freezing and lyophilization, in order to obtain GelMA as a dry product.

^{1}H NMR experiments were recorded on a Bruker Avance 500 MHz spectrometer. Samples were dissolved in 1 mL of deuterium oxide (D_2O) containing 3-(trimethylsilyl)propionic-2,2,3,3,-d_4 acid (TMSP) as an internal standard at (δ (^{1}H) = 0 ppm).

5.3.3. Fabrication of Microfluidic Device

A hydrodynamic flow focusing microfluidic device was fabricated using standard photolithography. Briefly, SU-8 was spin-coated on the surface of a silicon wafer to a final thickness of 150 μm. The wafer was then soft baked for 30 min at 65°C and for 60 min at 95°C. Using a photolithography mask, the flow focusing design was patterned on the SU-8 layer by exposing it to UV light. The patterned wafer was post-baked at 95°C for 90 min, followed by a development step using SU-8 developer. The pattern consisted of a 100 μm central channel connected to two 100 μm lateral channels at an angle of 150°.

Polydimethylsiloxane (PDMS) prepared by a 10:1 (w/w) mixture of silicone elastomer base and curing agent was deposited at the surface of the SU-8 patterned silicon wafer. After bubble removal from PDMS using a vacuum chamber, the assembly was baked at 150°C for 3 h to allow PDMS polymerization and hardening. After 3 h, the PDMS was then peeled off from the wafer and holes were punched in the inlets and outlets of the channels. The PDMS layer was permanently bonded to a PDMS-coated glass slide using plasma cleaning. The chips were then baked at 80°C for at least 3 h in order to allow restoration of hydrophobicity. The solvent phase circulated in the central channels, while the nonsolvent phase was injected in the lateral channels.

5.3.4. Preparation and Characterization of GelMA Nanoparticles

GelMA nanoparticles were produced inside of a hydrodynamic flow focusing microfluidic device. GelMA at 5% (w/v) was dissolved in PBS containing 0.5% (w/v) of irgacure 2959. This solution was used as the solvent phase which flowed in the central channel of the microfluidic device. The nonsolvent phase was composed of toluene and span 80 mixed at a 4:1 (w/w) ratio. The nonsolvent phased circulated in the lateral channel at a flow rate of 400 μL/min, while 4.5 μL/min was used in the hydrogel phase.

Aliquots of 500 μL of the nanogel solution were collected in the outlet of the microfluidic device. These samples were kept in the dark for 12 h at room temperature to allow for particle stabilization. After 12 h, the sample vials were exposed to a 300 nm UV light (2 mW/cm^2) for 30 min under 200 rpm stirring. After light exposure, nanogels were washed using 1 mL of THF, followed by centrifugation for 7 min at 8,000 rpm. This washing procedure was repeated three times. Nanogels were then stored in 0.5 mL of deionized water. A volume of 10 μL of the nanogel solution was pipetted in a Formvar TEM grid and TEM images were taken using a Jeol 1011 Transmission Electron Microscope.

In the case of GNP@GelMA, a solution containing 10% (w/v) of GelMA was prepared in 1% (w/v) of irgacure 2959 in PBS. This solution was then diluted to 5% (w/v) and 0.5% (w/v) of GelMA and irgacure 2959, respectively, using a 10 nm spherical GNP suspension to a final concentration of 2 x 10^{12} nanoparticles/mL. The suspension containing GelMA and GNPs was then injected in the central channel of the microfluidic device as the solvent phase. The same fabrication and washing procedures listed above was used.

TEM images provided a visualization of the size of the nanogels using image processing program ImageJ (http://imagej.net), in which the diameter of 100 nanogels were measured. The final diameter of the nanogels was calculated by averaging the measurement for each experiment (100 particles) and calculating the standard deviation. The experiments were repeated three times from different batches of nanogels fabricated in the microfluidic device.

5.4. Results and Discussion

5.4.1. Characterization of Gelatin Methacryloyl

Figure 5.1(a) shows the preparation of GelMA through the reaction between glycidyl methacrylate and gelatin type A in acidic conditions (pH 3.5). The mechanism of this reaction, presented in **Figure 5.1(b)**, involves an epoxide ring-opening of glycidyl methacrylate by the hydroxyl and carboxylic functional groups of gelatin [240]. with the geminal vinyl hydrogen of 3-methacryloyl-1-glycerylester and 3-methacryloyl-2-glycerylester fragments in GelMA. The peak at 2.07 ppm, shown in orange in **Figure 5.1(c)**, also indicates the reaction of gelatin type A with glycidyl methacrylate, since it corresponds to the methyl carbon-linked hydrogens at the vinyl carbon. In addition, the presence of the lysine peak at 3.00 ppm, illustrated in pink in **Figure 5.1**(**c**), in the GelMA spectrum confirms the reaction of glycidyl methacrylate with hydroxyl and carboxylic groups, instead of amine groups.

The resulting GelMA material (polymer A) is a pH-responsive hydrogel that displays swelling at pH 6.0 (Chapter 4). In the case of the tumor microenvironment, a cascade effect occurs due to the growth of cancer cells within healthy tissue. These include an increase in interstitial pressure resulting from the increase in the elastic stress of the rapid proliferation, and a decrease in pH in the tumor area due to a disorganized blood vessel network and poor tissue lymphatics [37, 44]. Consequently, cationic hydrogels, such as the GelMA synthesized as described in **Figure 5.1**, should be useful to target release molecules/particles in an acidic tumor environment.

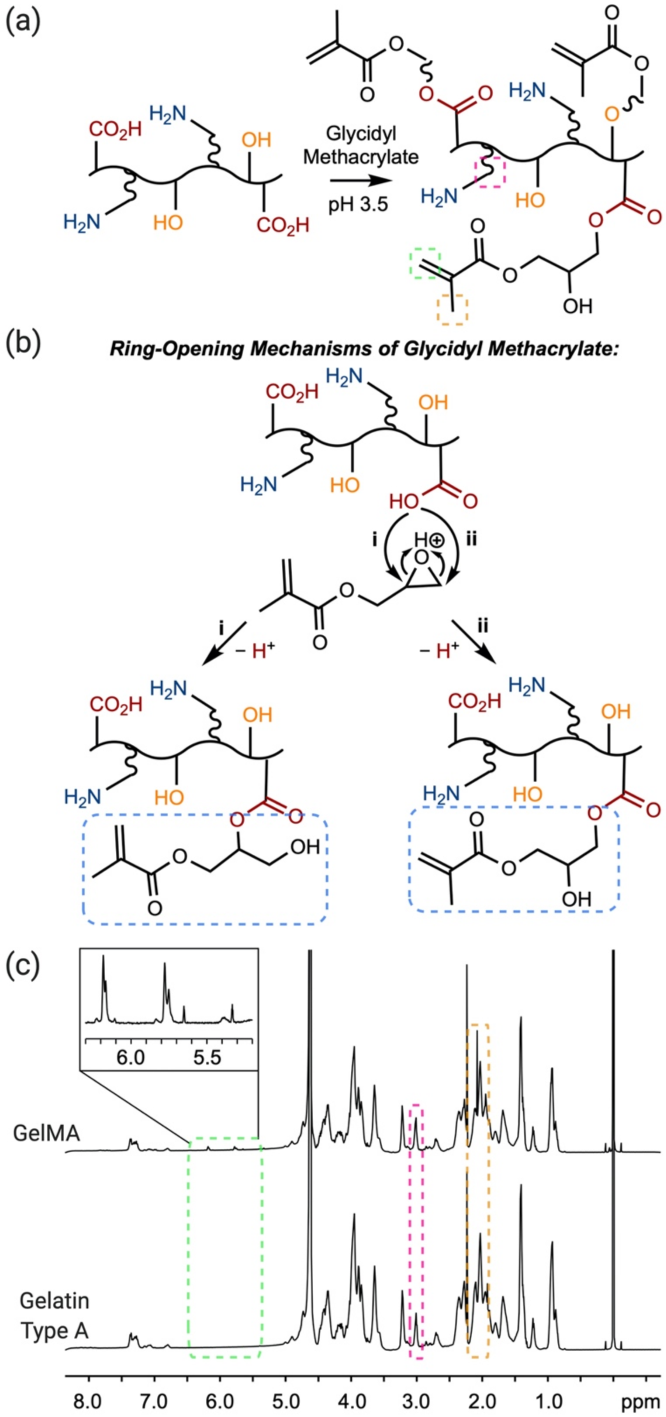

Figure 5.1 Synthesis of GelMA

(a) The reaction of gelatin type A with glycidyl methacrylate at pH 3.5. (b) Reaction happens through epoxide ring-opening. (c) ^{1}H NMR spectra of GelMA (top) and gelatin type A (bottom). Gelatin type A displays the appearance of peaks at 2.07 ppm, 5.76 ppm and 6.18 ppm in the GelMA spectrum, confirming the reaction of glycidyl methacrylate with gelatin type A.

5.4.2. Fabrication of Nanogels in Microfluidic Device

GelMA nanoparticles with and without GNP where produced in a hydrodynamic flow focusing microfluidic device, as illustrated in **Figure 5.2(a)**. A solution containing 5% (w/v) GelMA in PBS was introduced to the central channel of the microfluidic device at 4.5 μL/min. A controlled temperature chamber was created around the syringe pump and tubing in which the solvent solution was circulating to maintain the temperature of the solution at 40 °C. This temperature control was required because GelMA-based solutions are solid-like at room temperature. In the side channels, a nonsolvent solution composed of toluene and span 80 was injected at 400 μL/min, as shown in **Figure 5.2(b)**. Span 80 was used to reduce the interfacial tension between the aqueous and the organic (nonsolvent) phases and also to stabilize the nanogels, preventing the particles from merging into each other. The aqueous solution is compressed into a thin stream by the high flow rate of the nonsolvent fluid. The interfacial diffusion between the two phases produces nanoprecipitation of polymeric nanoparticles.

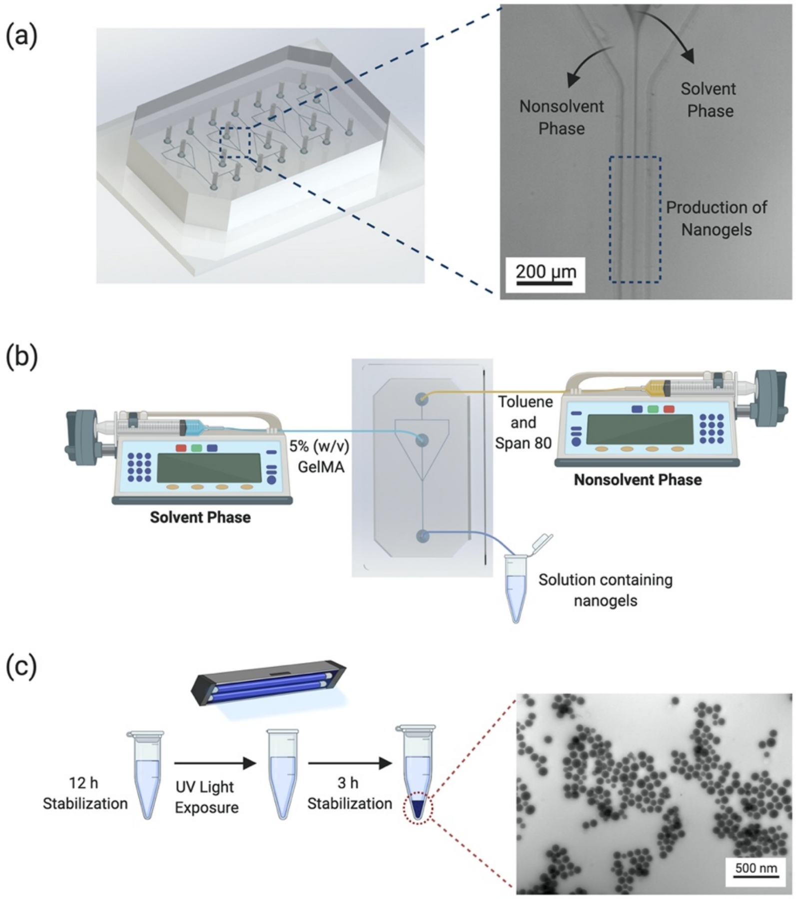

Figure 5.2 Experimental Procedure Steps on the Fabrication of Nanogels
(a) Nanogels were fabricated in a hydrodynamic flow focusing microfluidic device containing a nonsolvent phase (400 µL/min) and a solvent phase (4.5 µL/min). (b) Two separated syringe pumps were used for the different phases. The polymer phase was composed of 5% (w/v) GelMA with or without GNP. The organic phase was composed of toluene and span 80 (surfactant). (c) Nanogel samples collected in the outlet of the microfluidic device were allowed to stabilize overnight, followed by UV exposure at 300 nm for 30 min (stirring at 200 rpm). After UV light exposure, samples were left undisturbed for 3 h, prior the washing steps.

The GelMA nanogels leaving the outlet of the microfluidic device were collected in 500 µL aliquots and allowed to stabilize in the dark for 12 h, as shown in **Figure 5.2(c)**. After 12 h, particles were crosslinked under UV irradiation for 30 min, followed by a 3 h stabilization period. The particles were then washed with THF, in order to remove the nonsolvent phase and any unreacted photoinitiator. The particles were kept in deionized water and samples were used within 3 days. TEM images were collected in order to analyze the size of the particles.

The synthesis of the nanogels using hydrodynamic flow focusing is relatively simple. Temperature control of the GelMA solution is crucial, since an increase in viscosity can affect the velocity of the solution inside the channel, resulting in particles with different sizes. In addition, although PDMS offers the optical transparency and hydrophobicity required in the microfluidic technique, its porosity results in swelling in organic solvents [274]. To decrease swelling, PDMS was baked at 150°C, leading to a decrease in permeability and, consequently, a decrease in swelling [40].

For every batch of nanogels produced, 8 mL of solution containing solvent and nonsolvent phases were collected. 4×10^{14} nanogels were produced within this (8 mL) volume (calculated considering average diameter of 75 nm), resulting in 5×10^{13} particles/mL.

5.4.3. Gelatin Methacryloyl and GNP-loaded Nanogels

Figure 5.3(a) shows TEM images of GelMA nanogels produced in the hydrodynamic flow focusing microfluidic device in the absence of GNP. The GelMA nanogels displayed a general spherical shape. An average diameter of 74 ± 7 nm for the GelMA nanogels was obtained from the size histogram presented in **Figure 5.3(b)**. The relatively narrow size distribution (around 10% dispersity) indicates that the nanogels displayed a homogenous particle size and spherical shape. Exposure of nanogels to 300 nm UV light for 30 min was enough to photopolymerize the hydrogel, leading to crosslinked particles. In addition, the washing procedure was efficient in the removal of the nonsolvent phase.

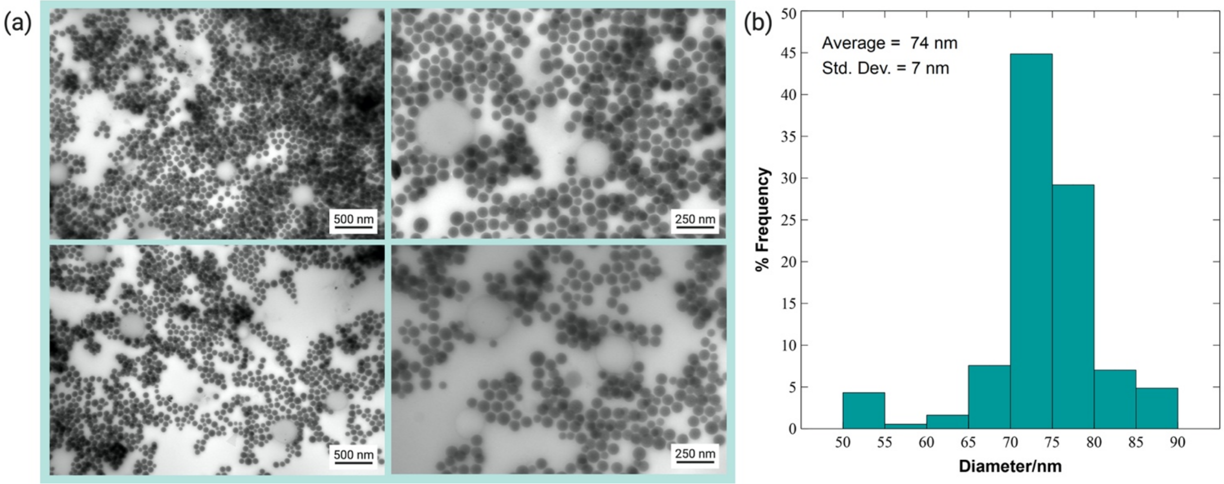

Figure 5.3 Characterization of GelMA Nanogels
(a) TEM images of GelMA nanogels in the absence of gold nanoparticles. (b) Size distribution of nanogels displayed an average particle diameter of 74 nm.

GNP@GelMA nanogels were produced by diluting a 10% (w/v) GelMA solution with GNPs suspension to a final concentration of 2 x 10^{12} nanoparticles/mL. The GelMA suspension containing GNP was then introduced in the hydrodynamic flow focusing microfluidic device, following the same procedure as described above. **Figure 5.4(a)** displays the TEM images of GNP@GelMA nanogels, illustrating spherical GelMA particles loaded with GNPs. **Figure 5.4(b)** shows a size histogram for the GNP@GelMA nanoparticles. An average diameter of 65 ± 12 nm was obtained from the histogram. The relative size distribution (around 18%) observed **Figure 5.4(b)** was broader than obtained for the GelMA nanoparticles (around 10%, **Figure 5.3(b)**). The larger size distribution in GNP@GelMA nanogels can be attributed to an increase in viscosity in the solvent phase due to the presence of the GNPs. The increased viscosity should influence the flow rate ratio (inlet sheath/lateral flows) and, consequently, the final size of the nanogels. Nevertheless, a significant amount of GNPs was loaded into the GelMA nanogels, as illustrated in **Figure 5.5**, while only a 10% reduction in average size (relative to the GelMA nanogels) was observed. In the case of the GNPs, a reduction in size from 9 ± 1 nm to 5 ± 0.5 nm was observed, as illustrated in **Figure 5.6**. The size of the particles was obtained from measuring the size of the GNPs outside and inside of the GelMA using TEM images. We believe that the UV light caused this reduction due to UV light reduction of Au(III) by citrate [275]. Finally, the final concentration of GNP@GelMA nanogels, considering an average diameter of 66 nm, were estimated at 5.1 x 10^{13} nanogels/mL.

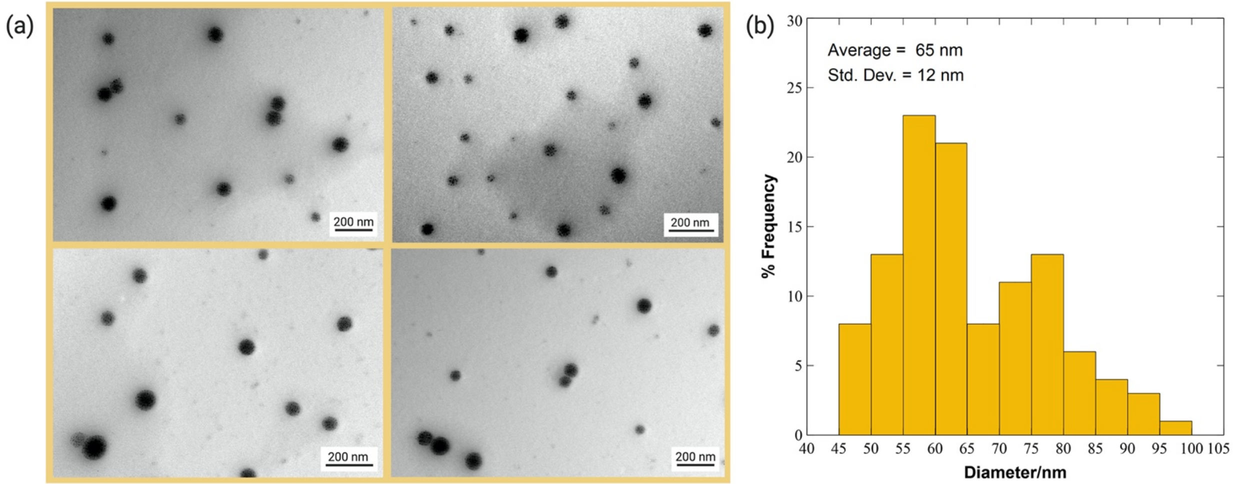

Figure 5.4 Characterization of GNP@GelMA Nanogels
(a) TEM images of GelMA nanogels in the presence of gold nanoparticles. Gold nanoparticles were added to the GelMA solution in the dispersed phase. TEM images illustrate dark particles inside the GelMA nanoparticles. (b) Size distribution of nanogels displayed an average particle diameter of 65 nm.

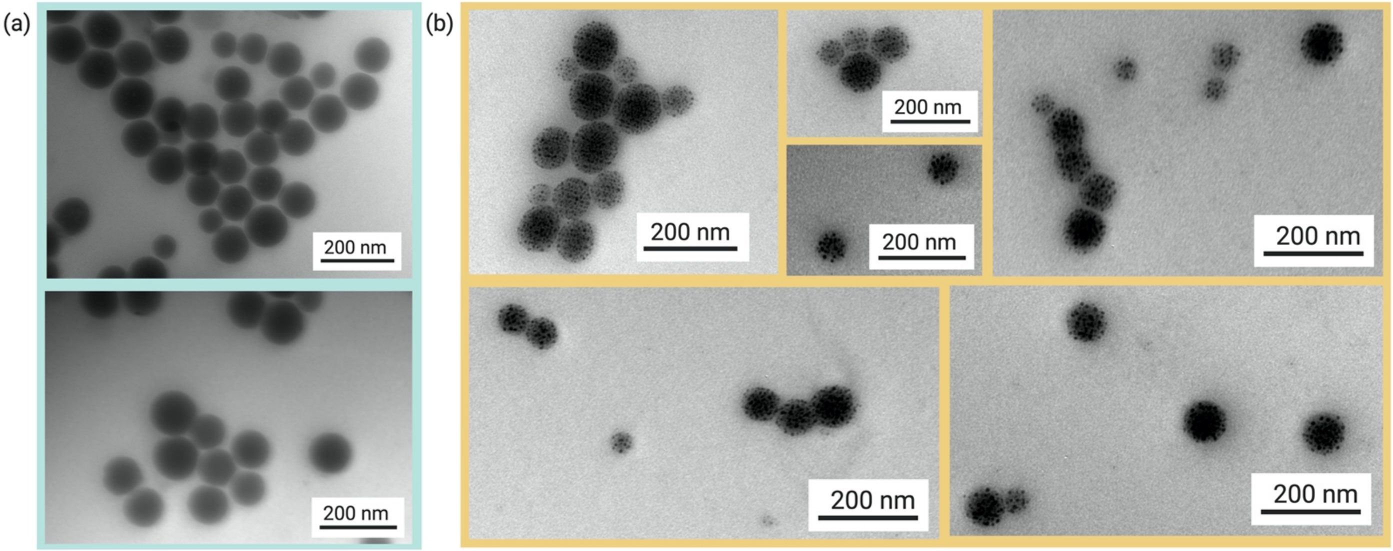

Figure 5.5 GelMA Nanogels
(a) GelMA nanogels produced in the absence of GNP. (b) GNP-loaded GelMA nanogels displaying homogeneous distribution of GNP in the hydrogel particle.

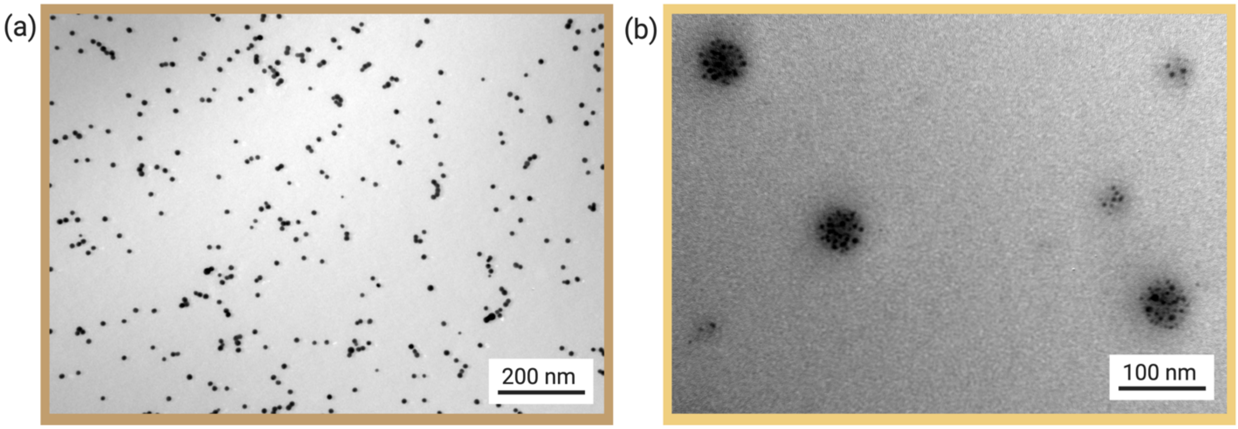

Figure 5.6 GNPs TEM Images
(a) GNPs used in the fabrication of GNP@GelMA nanogels. (b) GNP@GelMA nanogels displayed a decrease in size of the GNPs.

5.5. Conclusions

In this study, we were able to fabricate GelMA nanogels with an average size of around 74 ± 7 nm and relatively narrow size distribution (dispersity around 10%). In addition, the fabrication of GNP@GelMA nanogels was also performed with an average size of 65 ± 12 nm (dispersity around 20%), showing a homogenous distribution of gold particles inside the nanogels. The nanogels were produced inside of a hydrodynamic flow focusing microfluidic device. During the bulk synthesis of nanoparticles, mixing is not just heterogenous, but it is longer than the time scale required for self-assembly [276]. This results in a broader nanoparticle size distribution [277]. Microfluidics, on the other hand, provides precise spatio-temporal manipulation of fluids, in addition to rapid mixing of solutions, resulting in the formation of uniform nanoparticles. In hydrodynamic flow focusing microfluidics, nanoparticles are formed by precipitation, in which mixing time is a key parameter [276]. Mixing time is dependent on the width of the microfluidic channel and on the flow rate ratio (inlet sheath/lateral flows). With a fixed channel width, increasing the flow rate ratio results in an increase of the size of the nanoparticles [278], illustrating the versatility of microfluidic devices on top of the controllable and large-scale production of nanogels (5 x 10^{13} nanogels/mL).

The interaction of nanoparticles with the tumor microenvironment is complex mainly due to the heterogeneous nature of solid tumors and their vasculature. While the EPR effect is a key feature on the passive extravasation pathway of particles from the blood vessels into the tumor area, large particles accumulate in the peripheral area of the tumor and cannot reach the cancer cells localized deeply in the tumor area. While large particles show low diffusivity through the interstitial matrix [279], nanoparticles larger than 60 nm have shown to be unable to diffuse through the collagen matrix [280]. Small particles, on the other hand, can diffuse faster and penetrate deeply into the tumor area. Although recent results have shown that nanoparticle extravasation through a passive pathway only accounts to a fraction of the accumulation of nanoparticles in tumors (25% in the case of 100 nm GNP), it has been shown that nanoparticles are also able to use trans-endothelial pathways (active route) to extravasate into the cancer area

[92]. Here we have shown the final sizes of the GNPs and GNP@GelMA nanogels to be 5 ± 0.5 and 65 ± 12 nm, respectively. While nanogels sizes are appropriated to avoid renal and liver clearance [281] and to perform passive and active extravasation, we have shown previously that GelMA displays negative surface charge [195], which was shown to enhance systemic circulation and accumulation in the tumor area [281, 282]. Additionally, the final diameter of the GNP seems to be ideal to enhance tumor uptake and permeability [211], highlighting the promising future applications of GNP@GelMA nanogels.

Chapter 6 Discussion and Conclusions

The overall focus of this research was to apply microfluidic devices and biomaterials to the study of cancer. The studies performed using microfluidic devices ranged from diffusion to drug delivery systems. In addition, the use of biomaterials was explored to provide a more realistic model ECM for breast cancer cells. Drug delivery systems were also created using GelMA with future applications to cancer therapy.

6.1. Discussion and Conclusion of Research Objective 1

The objective was to create a hydrogel composite matrix to simulate the mechanical properties of healthy and cancerous breast cancer ECM. In addition, by using a pressurized microfluidic device, the study of impact of interstitial pressure and ECM stiffness was the diffusion of species was also investigated.

The creation of a hydrogel composite composed of gelatin methacryloyl and collagen type I was demonstrated in Chapter 2. GelMA was selected due to its high elastic modulus, biocompatibility, negative charge, and tuning capabilities. Collagen type I was chosen since it is the most abundant protein in *in vivo* ECM, enhancing biocompatibility and the creation of a more realistic ECM. Tuning the collagen type I-gelatin methacryloyl hydrogel composition allowed the simulation of *in vitro* healthy ECM and cancerous ECM in terms of stiffness. Hydrogel composites displayed elastic moduli of 183 ± 10 Pa 5914 ± 120 Pa for 3 Coll I-3.75 GelMA and for 1 Coll I-11.25 GelMA, respectively, similar to elastic modulus values displayed by healthy and cancerous breast ECM. Breast cancer cells encapsulated in the hydrogel matrices displayed high cell viability and proliferation.

Given that the chemotherapy and radiation therapy are common cancer treatment options, the diffusion of fluorescein dye (simulating a drug) and gold nanoparticles through the hydrogel composite matrices simulating healthy and cancerous tissues was analyzed. The diffusion of the species was tracked by fluorescence within a microfluidic device. The microfluidic device was composed of three channels: one ECM-mimicking central channel and two identical lateral channels, mimicking capillary vessels. The hydrogel composite was injected in the central channel, while fluorescein and 10 nm gold nanoparticles were injected in the lateral channels. Pressurization of the channel containing the hydrogel matrix to 18 mmHg simulated the increase in interstitial pressure seen in solid tumors. On the other hand, implementation of 3 mmHg on the lateral channel simulated pressurized capillary vessels in heathy tissue. A decrease in diffusion coefficients of 77% and 68% were obtained for the gold nanoparticles and for fluorescein, respectively. These results indicated that with the opposing advection, adverse pressure gradient also hindered diffusion, illustrating the impact of the tumor microenvironment on the delivery of species.

Furthermore, the creation of a collagen type I-GelMA composite with different concentration provided the mimicking of mechanical and chemical properties of native ECM. The microfluidic device, on other hand, showed to be a promising platform to analyze transport of species due to its versatility and manipulation of small samples.

6.2. Discussion and Conclusion of Research Objective 2

The objective was to further investigate the transport of gold nanoparticles by introducing the impact of surface charge on diffusion. The transport of charged gold nanoparticles was evaluated in the same microfluidic device used in Chapter 2. In addition, cellular uptake of the gold nanoparticles was analyzed in 3D breast cancer *in vitro* models in order to find a correlation between cellular uptake and diffusion.

In Chapter 3, transport and cellular uptake of neutral, positive, and negative gold nanoparticles were studied. Collagen type I-gelatin methacryloyl hydrogel composite (1 Coll I-

11.25 GelMA) was used to mimic cancerous ECM (as detailed in Chapter 2). The diffusion coefficients obtained by the gold nanoparticles displayed movement of neutral particles, followed by negative, and then positive particles. Considering that the hydrogel composite showed overall negative charges, it was expected to verify fastest diffusion in the case of negatively charged particles. However, since collagen type I is positively charged, it is possible that electrostatic interaction between negative gold nanoparticles and collagen fibers had happened, decreasing the diffusion coefficient. In the case of positively charged particles, since GelMA is the major component in the hydrogel composite, electrostatic interaction between these species slowed down the movement of the particles.

Cellular uptake of the charged gold nanoparticles was evaluated in 3D breast cancer *in vitro* models using TEM (qualitative analysis) and ICP-MS (quantitative analysis). Breast cancer cells lines (MCF-7 and MDA-MB-231) encapsulated in 1 Coll I-11.25 GelMA hydrogel matrix displayed high cell viability and proliferation. Charged gold nanoparticles were in contact with 3D models for 48 hours. Uptake of the particles was observed in TEM. However, no quantitative investigation was possible due to the size of the hydrogel scaffolds. Quantitative analysis was performed by ICP-MS. The results confirmed higher cellular uptake for positively charged particles. However, surprisingly, a relatively higher cellular uptake was seen for negative particles than neutral.

Furthermore, the analysis of cellular uptake and diffusion resulted in an inverse correlation between these two parameters. Most of cellular uptake experiments is performed in 2D and diffusion is not considered in 2D experiments. Therefore, the results illustrated the need for complex 3D models in order to analyzed transport of drug delivery systems. In addition, it is evidenced that diffusion and cellular uptake of particles should be studied together in more realistic *in vitro* models.

6.3. Discussion and Conclusion of Research Objective 3

The objective was to investigate the synthesis of pH-responsive GelMA hydrogels. Two pH-responsive polymers, polymers A and B, were created based on the reaction with different functional groups in the gelatin backbone. A flow focusing microfluidic device was used in the production of hydrogel microspheres.

In Chapter 4, two pH-responsive polymers were synthesized. Polymer A was produced by the reaction of gelatin type A with glycidyl methacrylate. This synthesis was conducted at pH 3.5, restricting the reaction of glycidyl methacrylate to the hydroxyl and carboxylic groups in the gelatin backbone. Consequently, amine groups remained unreacted once polymer A was obtained, as observed in ^{1}H NMR. Using a flow focusing microfluidic device, uniform microspheres of 39.4 ± 2.6 μm were created. These microspheres showed an increase in diameter to 54.6 ± 3.0 μm at pH 6 (pH of the tumor microenvironment), displaying a swelling behavior of 167% when compared to basic pH.

In the case of polymer B, gelatin type B was reacted with methacrylic anhydride at neutral pH. Methacrylate reacted mostly with amine and hydroxyl groups was observed in ^{1}H NMR. Consequently, carboxylic groups were available in the polymeric chains of polymer B. Microspheres of polymer B were produced inside of the microfluidic devices, displaying a final size of 38.6 ± 2.3 μm. When these particles were introduced to a basic solution (pH 10), a change in diameter to 61.1 ± 3.2 μm was seen, displaying a swelling of 296 % when compared with acidic pH.

Furthermore, novel pH-responsive GelMA hydrogels were produced. The swelling of GelMA-based microspheres showed in this study amplifies the application of this biomaterial as a pH-responsive hydrogel, from drug delivery systems, to pH-responsive sensor applications.

6.4. Discussion and Conclusion of Research Objective 4

The objective was to investigate the fabrication of nanogels of polymer A (from Chapter 4) using microfluidic devices. In addition, it was also aimed to introduce gold nanoparticles to the nanogels.

In Chapter 5, nanogels of 74 ± 7 nm were produced using polymer A in a flow focusing microfluidic device. Considering unique features of solid tumors include a leaky vasculature and a decrease in pH, the polymer A nanogels could be applied as drug delivery systems to the cancer area due to its swelling behavior in acidic pH (as seen in Chapter 4).

Although large nanoparticles may be able to accumulate at the tumor area, further diffusion is hindered due to the size of the particles. Considering that gold nanoparticles are radiotherapy enhancers; small gold nanoparticles were introduced to the hydrogel samples in order to produce gold nanoparticles-loaded GelMA nanogels. The nanogels produced in the flow focusing microfluidic device displayed an average diameter of 65 ± 12 nm. Although it is believed that the broad size distribution is due to a change in viscosity in the hydrogel solution, a significant amount of gold was loaded in the GelMA nanogels.

6.5. Overall conclusions and future work

The combination of microfluidic devices and drug delivery systems explored in this work contributes to the state-of-the-art in the field of cancer research. Research aspects not previously explored or documented in the open literature were addressed here: i) the impact of properties of the tumor microenvironment, such as stiffness and interstitial pressure, in the transport of species, ii) the correlation between cellular uptake and diffusion in 3D in vitro models, and iii) the combination of extravasation and diffusion in drug delivery systems by producing gold nanoparticles-loaded GeMA hydrogels.

Future work related to the results presented in Chapters 2 and 3 include the modification of the microfluidic device in order to allow the addition of breast cancer cells to the hydrogel composite. In addition, the study of diffusion and cellular uptake of charged gold nanoparticles (with different sizes and shapes) should also be performed by including 18 mmHg in the systems. This will provide a broader understanding of the correlation between diffusion and cellular uptake in more realistic *in vitro* systems.

The encapsulation and release of chemotherapy drugs in an *in vitro* model should be explored and studied to extend the work presented in Chapter 4. Although swelling behavior of GelMA microspheres was investigated, it is necessary to explore the drug encapsulation and the drug release profile in a system containing a pH gradient.

The fabrication of more uniform gold nanoparticles-loaded GelMA nanogels should be investigated to enhance the work presented in Chapter 5. In addition, the release of gold nanoparticles needs to be explored *in vitro* and *in vivo* in order to verify the type of delivery (swelling or degradation). These experiments will be essential for *in vivo* applications of these nanogels

Chapter 7 Academic activities

7.1. Research and Review Papers Published

1. Katy Schafer, Heiko Ihmels, Cornelia Bohne, Karolina Papera Valente, Anton Granzhan. **Hydroxybenzo[b]quinolizium Ions: Water-Soluble and Solvatochromic Photoacids**. *J. Org. Chem.* 2016, 81, 22, 10942-10954

2. Mohammad Hossein Mohammadi, Behnaz Heidary Araghi, Vahid Beydaghi, Armin Geraili, Farshid Moradi, Parya Jafari, Mohsen Janmaleki, Karolina Papera Valente, Mohsen Akbari, Amir Sanati-Nezhad. **Skin Diseases Modeling Using Combined Tissue Engineering and Microfluidic Technologies**. *Adv Healthc Mater*. 2016, 5(19), 2459-2480

3. Karolina P. Valente, Sultan Khetani, Ahmad R. Kolahchi, Amir Sanati-Nezhad, Afzal Suleman, Mohsen Akbari. **Microfluidic technologies for anticancer drug studies**. *Drug Discovery Today* 2017, 22, 11, 1654-1670

4. Shirin Soleimani, Milad Shamsi, Mehran Ghazani, Hassan Modarres, Karolina Papera Valente, Mohsen Saghafian, Mehdi Mohammadi Ashani, Mohsen Akbari, Amir Sanati-Nezhad. **Translational Models of Tumor Angiogenesis: A nexus of in Silicon and *in Vitro* Models**. *Biotechnol Adv*. 2018, 36, 4, 880-893

5. America Palacios, Karolina Papera Valente, Alexandre G. Brolo. **Optofluidic Platforms for Applications in Cancer Research**. *Conference on Lasers and Electro-Optics, OSA*. 2018

6. Karolina P. Valente, Sapanbir S. Thind, Mohsen Akbari, Afzal Suleman, Alexandre G. Brolo. **Collagen Type I-Gelatin Methacryloyl Composites: Mimicking the Tumor Microenvironment**. *ACS Biomater. Sci. Eng*. 2019, 5, 6, 2887-2898

7. Meghan Robinson, Karolina Papera Valente, Stephanie M Willerth. **A novel Toolkit for Characterizing the Mechanical and Electrical Properties of Engineered Neural Tissues**. *Biosensors (Basel)*. 2019, 9, 2, 51

8. Karolina P. Valente, Sapanbir S. Thind, Afzal Suleman, Alexandre G. Brolo. **Merging micro and nano: study of transport of gold nanoparticles inside a tumor microenvironment-on-a-chip**. *SPIE BiOS*. 2019

9. Karolina Papera Valente, Alexandre Brolo, Afzal Suleman. **From Dermal Patch to Implants-Applications of Biocomposites in Living Tissues**. *Molecules*. 2020, 25, 3, 507

7.2. Manuscripts Under Preparation/Submission

1. Karolina P. Valente, Afzal Suleman, Alexandre G. Brolo. **Exploring Diffusion and Cellular Uptake: Charged Gold Nanoparticles in an *in vitro* Breast Cancer Model**

2. Karolina P. Valente, Cameron Polglase, Roman G. Belli, Elaina Bourque, Afzal Suleman, Alexandre G. Brolo. **Synthesis and Fabrication of pH-responsive Gelatin Methacryloyl Microspheres**

3. Karolina P. Valente, Cameron Polglase, Elaina Bourque, Roman G. Belli, Afzal Suleman, Alexandre G. Brolo. **Preparation of Gold Nanoparticles-Loaded Gelatin Methacryloyl Nanogels: Nanocarriers for Drug Delivery Systems**

7.3. Oral and Poster Presentations

1. (2016) **Tumor-on-a-chip: A new ally against cancer**. 3MT Competition on Engineering and Science Heat, University of Victoria, Victoria BC, Canada

2. (2016) **Tumor-on-a-chip: A new ally against cancer**. Idea Fest: 4th Annual Pecha Kucha Biomedica Oral Presentation, University of Victoria, Victoria BC, Canada

3. (2017) **Microfluidic Devices: Miniaturizing the tumor environment**. STEM Research Symposium, University of Victoria BC, Canada (3rd place Best Oral Presentation)

4. (2018) **Effect of the Tumor Microenvironment on the Diffusion of Gold Nanoparticles**. 34th Annual Meeting of The Canadian Biomaterials Society, Victoria BC, Canada (Poster)

5. (2018) **Mimicking the Tumor Microenvironment on a Microfluidic Device Using a Hydrogel Mixture**. 101st Canadian Society of Chemistry Conference, Edmonton AB, Canada (Oral)

6. (2018) **When Nano Meets Micro: Studying the Transport of Gold Nanoparticles in a Microfluidic Device**. Pacific Centre for Advanced Materials and Microstructures Conference, Vancouver BC, Canada (Poster)

7. (2018) **When Micro Meets Nano: Gold Nanoparticles in Microfluidic Devices**. STEM Research Symposium, University of Victoria BC, Canada (2nd place Best Oral Presentation)

8. (2019) **Merging Micro and Nano: Study of Transport of Gold Nanoparticles inside of a Tumor-on-a-chip**. SPIE Photonics West, San Francisco CA, United States (Oral)

9. (2019) **Exploring Diffusion and Cellular Uptake: Transport of Gold Nanoparticles in an *in vitro* Breast Cancer Model**. 102nd Canadian Society of Chemistry Conference, Quebec QC, Canada (Oral)

10. (2019) **Taking Advantage of the Tumor Microenvironment: Exploring Drug Delivery Systems**. STEM Research Symposium, University of Victoria BC, Canada (1st place Best Oral Presentation)

Appendix A

Appendix A presents the supplementary information for Chapter 2[c].

A1. Absorption and Emission Spectra

The absorption spectra of CY3-GNP and fluorescein sodium salt were measured in deionized water (pH 7) using Cary 60 UV-Vis (Agilent Technologies). Excitation of CY3-GNP and fluorescein dye was performed at 543 nm and 488 nm, respectively. The emission spectra were collected on Cary Eclipse Fluorescence Spectrophotometer (Agilent Technologies) and a wavelength range of 550 – 800 nm and 500 – 800 nm was employed for CY3-GNP and fluorescein sodium salt, respectively.

A2. 2, 4, 6-Trinitrobenzene Sulfonic Acid Assay (TNBS)

In order to quantify the degree of methacrylation of GelMA, TNBS assay was used, where free amino groups were quantified. The detailed description of this process has been reported elsewhere [111, 283]. Briefly, Gelatin bloom 300 and GelMA were dissolved in 0.1 M sodium bicarbonate buffer ($NaHCO_3$) solution to obtain a final concentration of 1.6 mg/mL. Glycine standard solutions with a range of concentrations (0, 0.8, 8, 16, 24, 32, and 64 μg/mL) were also prepared in the same buffer solution. A solution of 0.01% TNBS was prepared in 0.1 M $NaHCO_3$ buffer and 0.5 mL of this solution was added to gelatin, GelMA and glycine samples to obtain a final volume of 1 mL. The mixture was incubated at 37 ˚C for 3 h. Following, 0.5 mL of 10% (w/v) sodium dodecyl sulfate and 0.25 mL of 1M HCl were added to the samples in order to stop the reaction. Absorbance values of the samples were measured at 335 nm using Cary 60 (Agilent Technologies). Based on glycine

---

[c] The following chapter is from: Karolina P. Valente, Sapanbir S. Thind, Mohsen Akbari, Afzal Suleman, Alexandre Brolo. **Collagen Type I-Gelatin Methacryloyl Composites: Mimicking the Tumor Microenvironment.** *ACS Biomater. Sci. Eng.*, 2019, 5, 2887-2898.

samples, a calibration curve was created and the concentration of amino groups in gelatin and GelMA samples were determined and, consequently, the degree of substitution by methacryloyl groups.

A3. Modification of substrate surface for hydrogel adhesion

Circular glass cover slips were modified in order to enhance hydrogel adhesion to the surface of the glass. For GelMA hydrogel pellets, a TMSPMA coating was performed based on a previously published protocol [284]. In brief, the cover slips were initially cleaned with 10% sodium hydroxide (NaOH) solution overnight and rinsed with deionized water, followed by a washing with ethanol, methanol and isopropanol. After the cleaning process, all the glass slips were dried under nitrogen atmosphere and then stacked, followed by 0.5 mL deposition of TMSPMA on top of the slips. The assembly was kept in the oven at 80 °C for 12 h. Finally, the glass cover slips were rinsed with ethanol, methanol and isopropanol, and dried under nitrogen. All the coverslips were used within 7 days after TMSPMA coating.

For collagen type I pellets, the cover slips were modified similarly to previously published protocol [285]. Briefly, glass cover slips were cleaned with ethanol and deionized water and dried with nitrogen. After cleaning, the cover slips were plasma treated for 5 min prior incubation in a 1% solution of APTES in 100% ethanol for 45 min. After incubation, slips were washed with ethanol and deionized water and incubated in 0.5% solution of glutaraldehyde in 1x PBS for 1 h. Finally, the glass cover slips were washed with deionized water and allowed to air dry.

A4. Hydrogel Porosity

Hydrogel pellets were prepared as described previously. In order to assess porosity, the solvent replacement method was used [197, 198]. The dry weight (M_{dry}) of the hydrogel composites was recorded after the dehydration process. Sequentially, dried samples were immersed in absolute ethanol overnight. After blotting excess of ethanol from the surfaces of the gels using a paper tissue, the wet masses (M_{wet}) of the samples were recorded. The porosity was calculated as:

$$\%Porosity = \frac{\left(M_{wet} - M_{dry}\right)}{\rho V} \times 100\% \tag{8}$$

where V is the volume of hydrogel samples and ρ is the density of absolute ethanol (0.789 g/cm^3).

A5. Zeta Potential

The electrical surface charge of hydrogel samples (collagen I, GelMA and collagen I-GelMA composites) and CY3-GNP were determined by zeta potential measurements using a Particle Analyzer Litesizer 500 (Anton Paar). A volume of 10 µL of each solution was mixed with 1 mL of deionized water (pH 7) and transferred to a zeta potential omega cuvette. Refractive index (1.33), relative permittivity (78.368), and viscosity (8.9x10^{-4} Pa.s) were assumed to be the same as for water.

A6. SEM Imaging

To visualize the internal structure of the collagen I-GelMA composite hydrogels, the samples were initially dehydrated for 10 min in solutions prepared with ethanol and deionized water (30%, 50%, 70%, 90%, and 100% ethanol). The detailed description of this process is reported elsewhere [286]. After deionized water/ethanol incubation steps, hydrogel samples were washed with ethanol/HMDS mixtures (33%, 50%, 66%, and 100% HMDS) for 15 min each. Finally, the hydrogel pellets were left to dry overnight and these dried hydrogels were then sputtered with gold coating for 3 min using an Anatech Hummer VI SEM sputtering system. Hitachi S-4800 Field Emission Scanning Electron Microscope (FESEM) was employed to characterize the morphology of the synthesized hydrogel films using an accelerating voltage of 2.0 kV and magnifications of 30,000x and 100,000x. The ethanol, followed by HMDS, dehydration process was chosen since lyophilization altered the pore size and structure of the hydrogels (**Figure A.2**).

A7. Elastic Modulus Calculation

The elastic modulus (E) of the gels were calculated based a modified Hertz Model theory for thin films [287]:

$$\frac{E}{E_{Hertz}} = \frac{1 + 2.3\omega}{1 + 1.15\omega^{1/3} + \alpha\left(\frac{R}{h}\right)\omega + \beta\left(\frac{R}{h}\right)\omega^2} \tag{9}$$

$$E_{Hertz} = \frac{3(1 - \nu^2)F}{4R^{1/2}\delta^{2/3}} \tag{10}$$

$$\omega \equiv \left(\frac{R\delta}{h^2}\right)^{1/2} \tag{11}$$

where R is the radius of the indenter, E_{Hertz} is the elastic modulus calculated using the Hertz Theory and ν is the Poisson's ratio of the hydrogel mixture (ν = 0.5) [288].

For a frictionless condition between the spherical indenter and the gel surface [287]:

$$\alpha\left(\frac{R}{h}\right) = 10.05 - 0.63\sqrt{\frac{h}{R}}\left(3.1 + \frac{h^2}{R^2}\right) \tag{12}$$

$$\beta\left(\frac{R}{h}\right) = 4.8 - 4.23\left(\frac{h^2}{R^2}\right) \tag{13}$$

All hydrogel measurements were in the parameter ranges of $\delta/h \leq \min(0.6, R/h)$ and $0.3 \leq R/h \leq 12.7$ (**Table 7**).

A8. Fabrication of tumor microenvironment-on-a-chip

The microfluidic device was fabricated by photolithography. Briefly, SU-8 100 was spin coated on top of a silicon wafer to a final thickness of 400 µm. The assembly was soft baked for 30 min at 65 °C and 90 min at 95 °C. Using a photolithography mask, the desired design was patterned on top of the SU-8 layer after exposure to UV light. A post baking at 95°C was performed before the development step. The wafers were developed using SU-8 developer solution and rinsed with isopropanol. Polydimethylsiloxane (PDMS) was prepared by 10:1 mixture of silicone elastomer base and elastomer curing agent and deposited on top of the SU-8 coated silicon wafer. After degassing, the assembly was baked at 70 °C for 12 h in order to allow PDMS polymerization. The PDMS layer was then peeled off from the wafer and inlet and outlet ports were punched using biopsy punchers. The PDMS layer was permanently bonded to a glass slide using plasma cleaning. Since a 10% decrease in power was seen on the UV light after a layer of PDMS is added on top of the sample (from 6.3 mW cm^{-2} to 5.7 mW cm^{-2}), hydrogel samples inside the chip were crosslinked for 20 extra seconds (4 min and 20 seconds), compared to the 4 minutes crosslinked of hydrogels in coverslips.

A9. Calculation of Diffusion Coefficient

Zen 2.3 software was used to obtain the intensity profiles of the CY3-GNP and fluorescein inside of the microfluidic device at different time scales. Intensity values were related to concentration of the two species and the profiles were fitted using Fick's second law of diffusion:

$$\frac{\partial^2 C}{\partial x^2} = \frac{1}{D}\frac{\partial C}{\partial t} \tag{14}$$

where D is the diffusion coefficient.

Two different solutions for the equation above were used: for the case where CY3-GNP and fluorescein solution were injected in only one of the two lateral channels, as illustrated by **Figure A.5**, a one-dimensional transient diffusion in semi-infinite medium solution was used [196]:

$$\frac{C_i - C}{C_i - C_0} = \operatorname{erf}\left(\frac{x}{2\sqrt{Dt}}\right) = \operatorname{erf}(\varphi) \tag{15}$$

$$\operatorname{erf}(\varphi) = \frac{2}{\sqrt{\pi}}\int_0^{\varphi} e^{-\xi^2} d\xi \tag{16}$$

For the case of injection of the solution containing both species (CY3-GNP and fluorescein) in both lateral channels, as illustrated by **Figure A.6**, a one-dimensional transient diffusion in finite medium solution was used [196]:

$$Y = \frac{C - C_i}{C_0 - C_i} = \frac{4}{\pi}\sum_{n=1}^{\infty} \frac{\sin\left(\frac{n\pi x}{L}\right) e^{-Dt\left({n\pi}/{L}\right)^2}}{n}, n = 1,3,5, \dots \tag{17}$$

Pressure-driven flow was also considered when mimicking a net inward pressure from the lateral channel to the central channel (3 mmHg), and an outward pressure from the central channel to the lateral channels (18 mmHg). For these cases, concentration profiles were generated by including an advection term in Fick’s second law, obtaining the advection-diffusion equation for incompressible flow with constant viscosity:

$$D\frac{\partial^2 C}{\partial x^2} = \frac{\partial C}{\partial t} + u\frac{\partial C}{\partial x} \tag{18}$$

To account for the effects of pressure-driven flow in porous media, the Darcy’s law was used in conjunction with the equation above:

$$q = -\frac{k}{\mu}\nabla P \tag{19}$$

where q is the flux (m/s), k is the intrinsic permeability of the medium (m^2), μ is viscosity (Pa.s) and ∇P is the pressure gradient (Pa/m). The fluid velocity (u) can be obtained by:

$$u = \frac{q}{\varepsilon} \tag{20}$$

where ε is the porosity of the medium.

To solve the one-dimensional advection-diffusion equation, a finite difference approximation of the spatial and temporal derivatives of the equation was employed. Initial conditions and a combination of fixed wall concentration and free flow boundary conditions was used in the initial value problem. The experimental data was then fitted to the model by a least-squares minimization process.

In all cases, a single component system was used during the fitting of the diffusion coefficient. Even though two components (GNP and fluorescein) were added simultaneously in the lateral channel during the diffusion experiment, the diffusion coefficients obtained for these species were the same as obtained for the species alone. This is due to the large pore size exhibited by the hydrogel matrix, compared to the small sizes of the diffusing species.

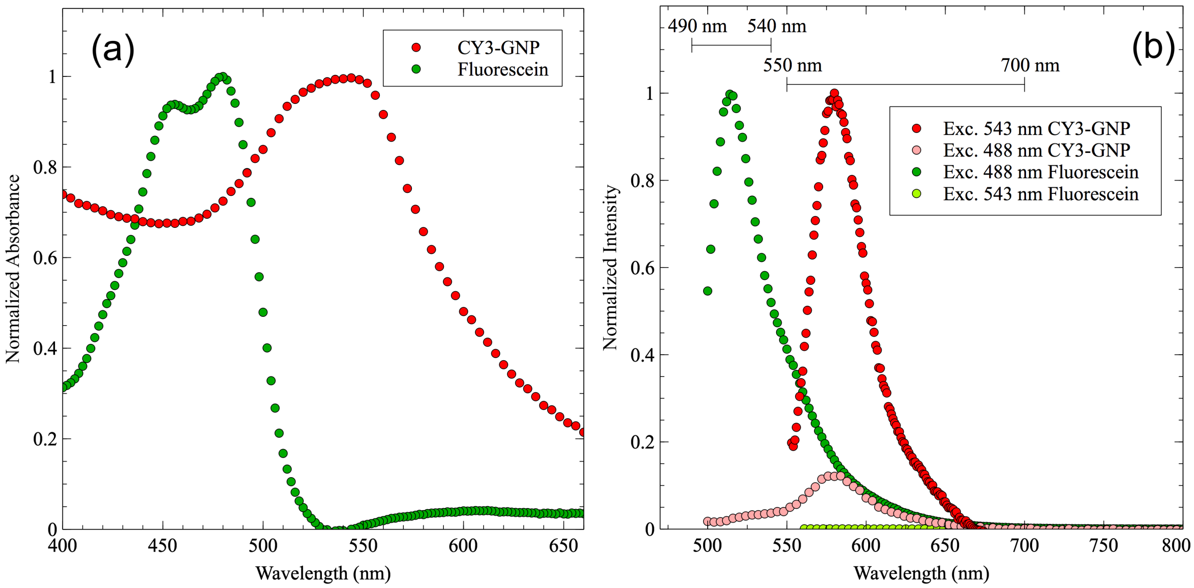

Figure A.1 Spectra of Gold Nanoparticles

Excitation (a) and Emission (b) Spectra of Gold Nanoparticles and Fluorescein Sodium Salt: Two emission collection windows were used for the acquisition of fluorescence signal from Fluorescein (490 nm to 540 nm) and CY3-GNP (550 nm to 700 nm).

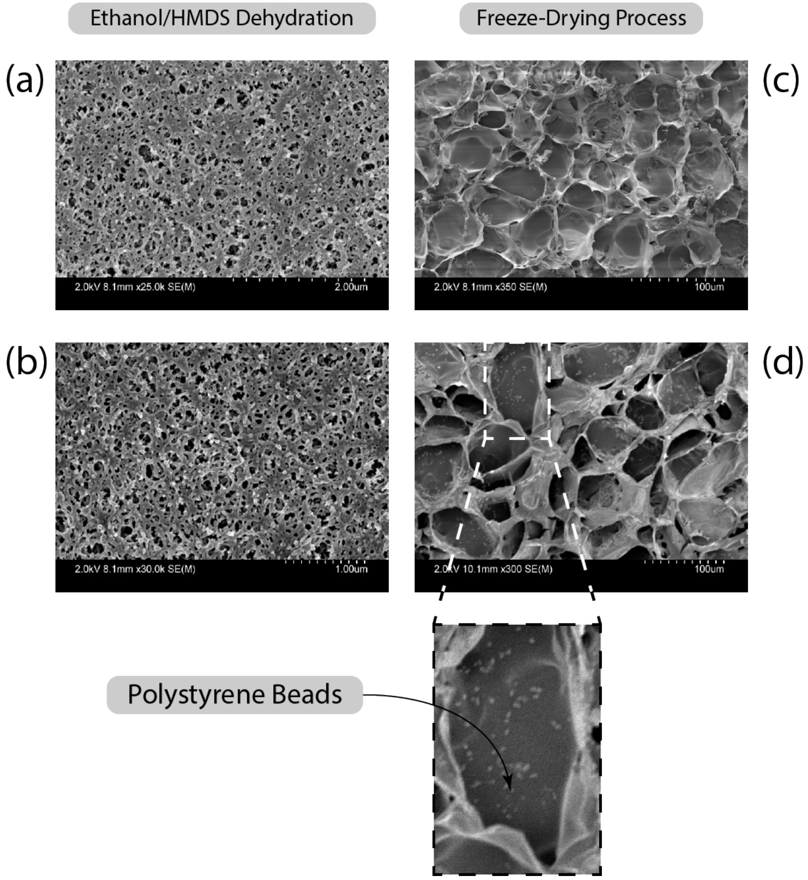

Figure A.2 Hydrogel Drying Method

While dehydration methods conserve hydrogel internal structure (a and b), dry-freezing methods, such as lyophilization, are not appropriate for soft gels due to the extensive change in pore size (c and d). Scale bars of 1.0 μm and 2.0 μm for Ethanol/HMDS images and of 100 μm for freeze-drying images were used.

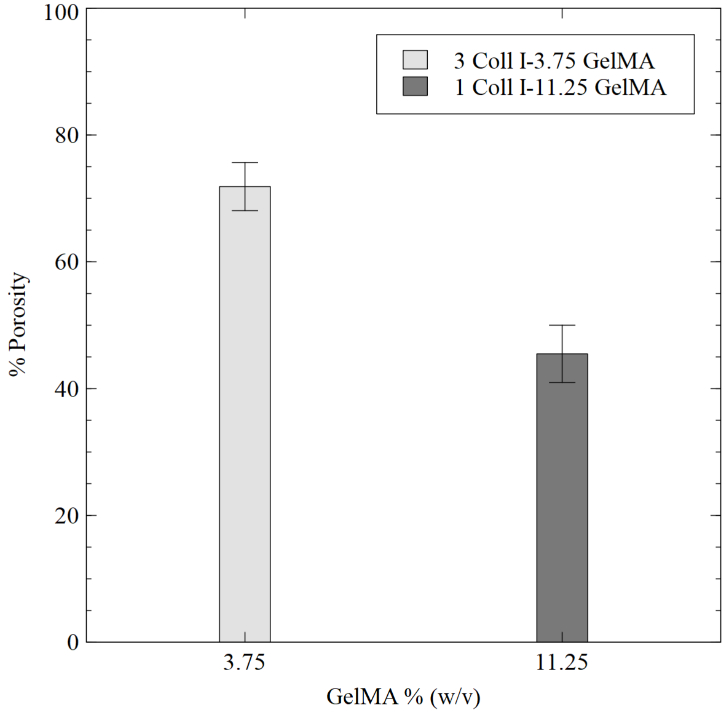

Figure A.3 Percentage Porosity of Hydrogel Composites

3-Coll I-3.75 GelMA (grey) and 1 Coll I-11.25 GelMA (white). Five samples were analyzed for each hydrogel concentration. Scale bars represent one standard deviation.

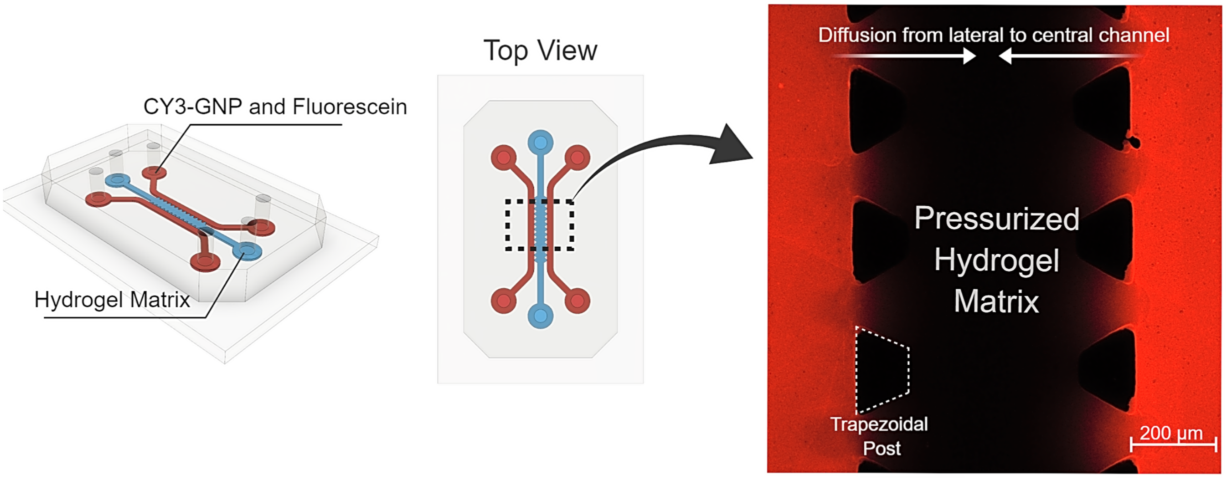

Figure A.4 Design of the microfluidic device

Device contained two identical lateral channels and one central channel. On the lateral channels, CY3-GNP and fluorescein sodium salt was injected, while the central channel contained the hydrogel composite. The diffusion of the species was tracked from the lateral channel into the central channel by fluorescence. Gaps created by trapezoidal posts allowed the contact between the hydrogel matrix and the solution in the lateral channels.

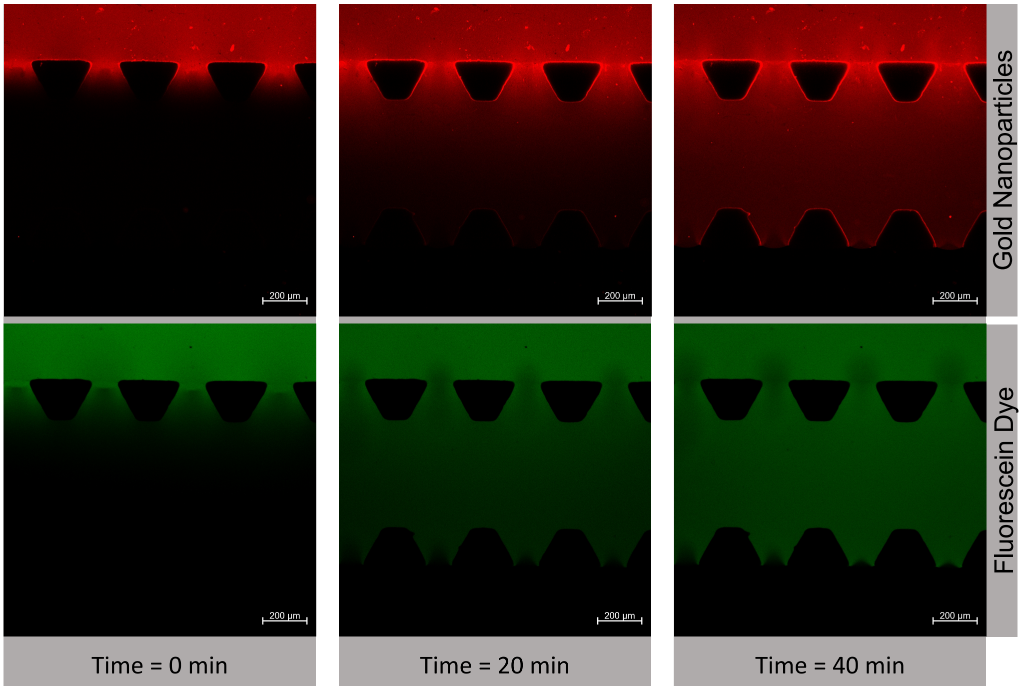

Figure A.5 Injection in one of the lateral channels of the microfluidic device
Diffusion process for CY3-GNP (red) and fluorescein sodium salt (green).

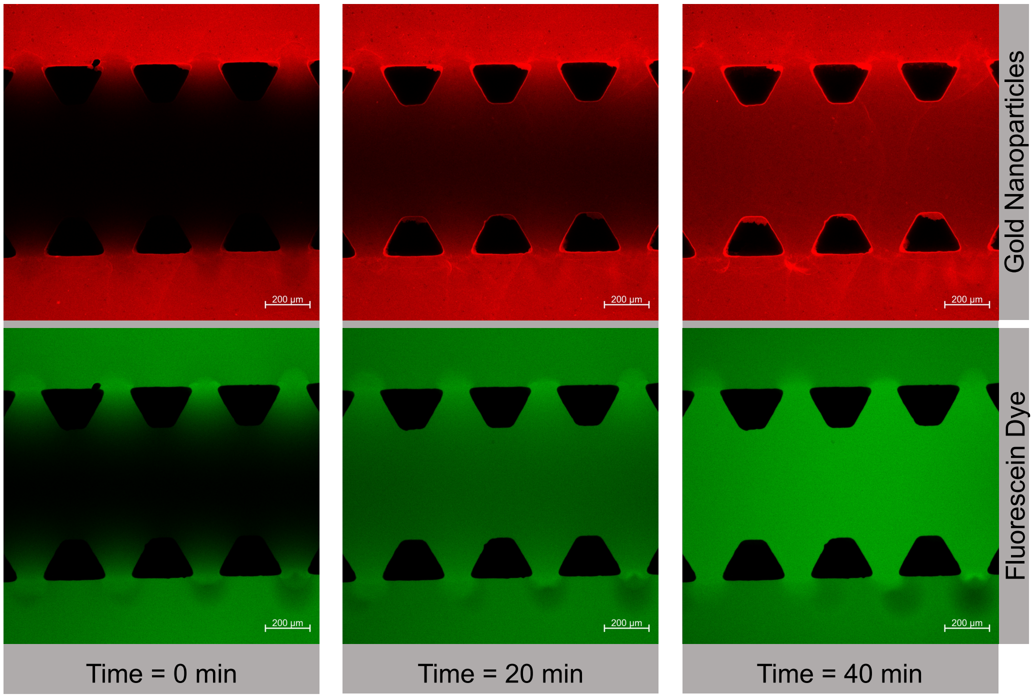

Figure A.6 Injection in both lateral channels of the microfluidic device
Diffusion process for CY3-GNP (red) and fluorescein sodium salt (green).

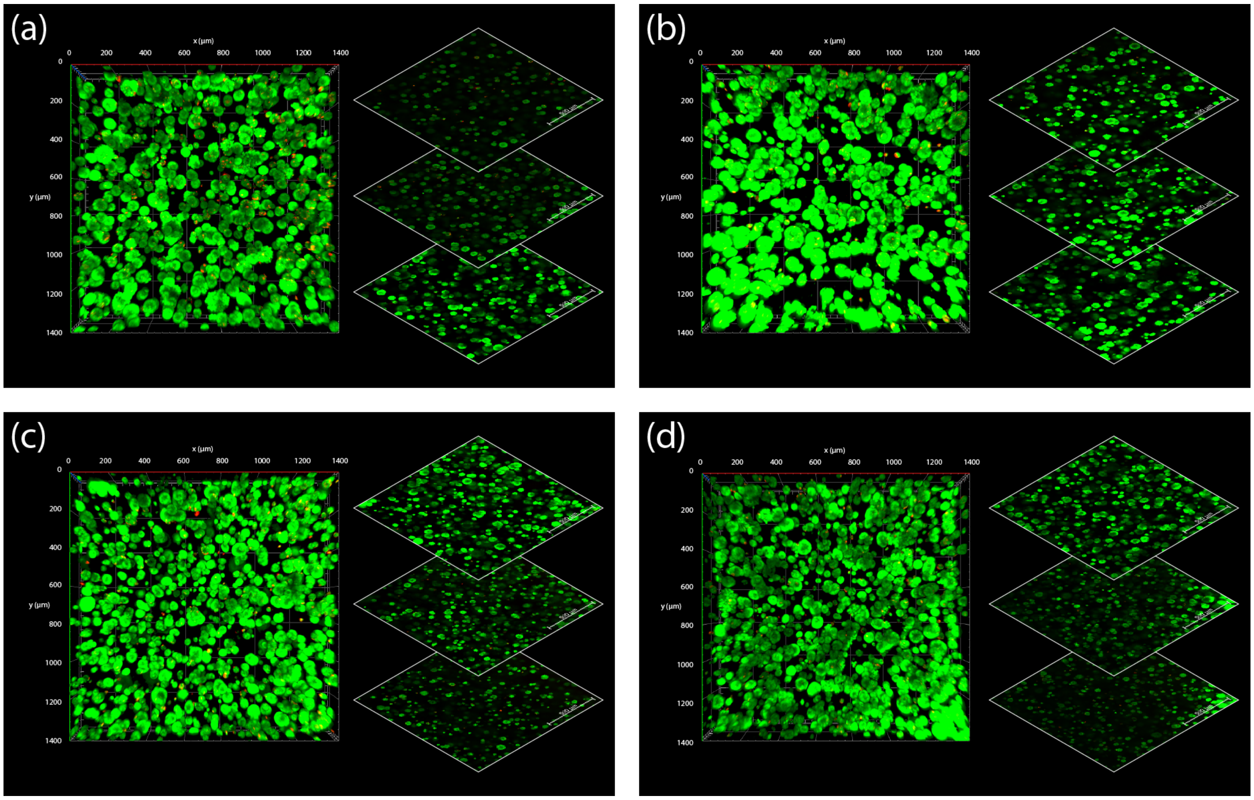

Figure A.7 Z-stack images of MCF-7 cell morphology in hydrogel pellets
a) 3.75 GelMA, b) 3 Coll I-3.75 GelMA, c) 11.25 GelMA, and d) 1 Coll I-11.25 GelMA.

Indentation Parameters	4 Coll I	3.75 GelMA	3 Coll I-3.75 GelMA	11.25 GelMA	1 Coll I-11.25 GelMA
δ/h ≤ min (0.6, R/h)	0.285±0.008	0.199±0.013	0.185±0.025	0.269±0.004	0.270±0.006
0.3 ≤ R/h ≤ 12.7	0.896±0.064	1.133±0.143	1.171±0.077	6.805±0.445	7.039±0.480

Table 7. Parameters for Modified Hertz Model Theory for Thin Films.

Appendix B

Appendix B presents the supplementary information for Chapter 3.

B1. (Trimethoxysilyl)propyl methacrylate (TMSPMA) Coverslip Modification

In order to enhance hydrogel adhesion, the surface of circular coverslips was modified with a TMSPMA coating. The procedure was performed based on a previously published protocol [284]. First, the coverslips were cleaned with 10% sodium hydroxide (NaOH) solution for 12 h, followed by rinsing with deionized water, ethanol, methanol, and isopropanol. After washing, glass coverslips were stacked on a rack and dried. Next, a volume of 0.5 mL of TMSPMA was deposited at the surface of the coverslips, followed by baking at 80 °C for 12 h. Finally, coverslips were rinsed with ethanol, methanol, and isopropanol in order to remove excess of TMSPMA. The coverslips were then dried under nitrogen and stored in the dark. The coverslips were used within 7 days.

B2. PrestoBlue Assay

Evaluation of cell viability was performed using PrestoBlue assay as described previously [195]. A solution of 10X PrestoBlue was diluted to a final concentration of 1X with cell media. Cell media was removed from the wells containing 3D *in vitro* cancer models and models were rinsed three times with PBS. The hydrogel samples were then incubated with 1X PrestoBlue solution for 1 h at 37 °C. After 1 h, a sample of 200 µL of was obtained from the wells to measure fluorescence signal at an excitation of 560 nm, and an emission of 590 nm using a plate reader. The fluorescence signal of the 1X PrestoBlue solution in absence of cells was also measured and used as a background control. Four samples were prepared for each charge of gold nanoparticles.

Viability measurements were performed on days 1, 4, 7, and 9. Measurements performed on day 7 were done prior to incubation with the samples of gold nanoparticles. Measurements performed on day 9 were done after 48 h of incubation of the hydrogel samples with the gold nanoparticles. The samples selected for cell viability measurements were not used for ICP-MS or TEM. The fluorescence values obtained were averaged for all 12 samples and standard deviation value was obtained. No difference in fluorescence signal was obtained on day 9 for the samples encapsulated with different charges of gold nanoparticles.

Increasing in fluorescence intensity was verified for both breast cancer cells (**Figure B.1**). Fluorescence values obtained for control cells (monolayers of MCF-7 and MDA-MB-231) were not included in **Figure B.1** since a much higher signal was obtained. High fluorescence signal obtained for the control samples is due to the direct contact by the cells with PrestoBlue solution. For cells encapsulated in the hydrogel samples, PrestoBlue had to diffuse through the matrix in order to reach the cells.

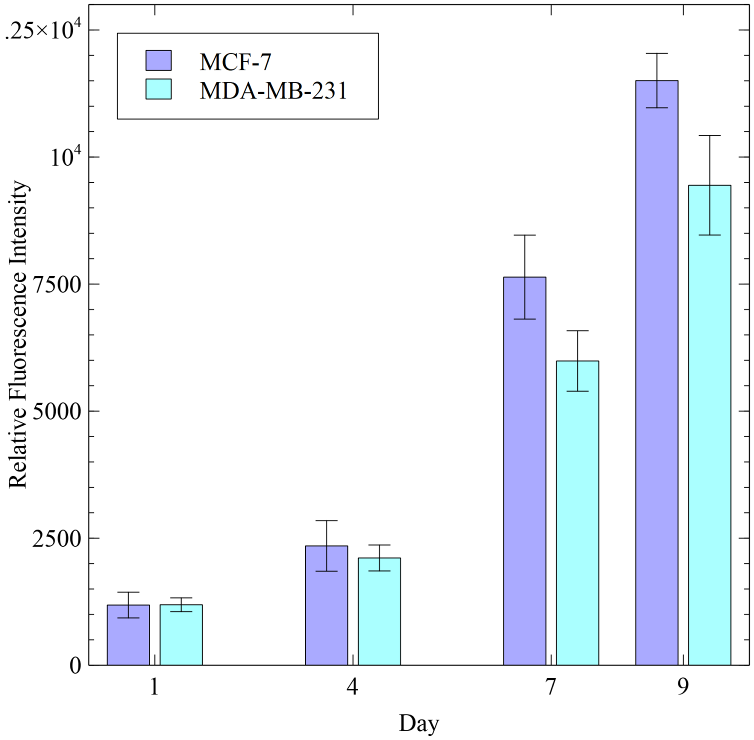

Figure B.1 Quantification of metabolic activity by PrestoBlue
Increasing fluorescence intensity values were obtained for both MCF-7 (purple) and MDA-MB-231 (blue). Scale bars represent one standard deviation.

Sample	Gold Concentration / ppb.g^{-1}
Neutral GNPs in MCF-7 3D hydrogel sample	112.08 ± 19.65
Neutral GNP in 3D hydrogel sample without MCF-7	43.43 ± 3.16
3D hydrogel sample without MCF-7 and without GNP	5.58 ± 1.14
Results for Neutral GNPs	**63.07 ± 3.24**
Negative GNPs in MCF-7 3D hydrogel sample	194.70 ± 18.46
Negative GNP in 3D hydrogel sample without MCF-7	63.02 ± 3.24
3D hydrogel sample without MCF-7 and without GNP	5.58 ± 1.14
Results for Negative GNPs	**126.09 ± 18.45**
Positive GNPs in MCF-7 3D hydrogel sample	2411.27 ± 310.69
Positive GNP in 3D hydrogel sample without MCF-7	408.40 ± 74.42
3D hydrogel sample without MCF-7 and without GNP	5.58 ± 1.14
Results for Positive GNPs	**1997.28 ± 310.69**

Table 8. Average gold concentration in MCF-7
3D hydrogel samples and in controls (GNPs in 3D hydrogel samples in absence of cell and 3 hydrogel samples in absence of cells and in absence of GNPs). The results for each charged GNPs were obtained by subtracting the averaged control values from the averaged concentration value for the MCF-7 3D hydrogel samples.

Sample	Gold Concentration / ppb.g^{-1}
Neutral GNPs in MDA-MB-231 3D hydrogel sample	69.88 ± 5.87
Neutral GNP in 3D hydrogel sample without MDA-MB-231	43.43 ± 3.16
3D hydrogel sample without MDA-MB-231 and without GNP	5.58 ± 1.14
Results for Neutral GNPs	**20.86 ± 5.87**
Negative GNPs in MDA-MB-231 3D hydrogel sample	102.26 ± 8.83
Negative GNP in 3D hydrogel sample without MDA-MB-231	63.02 ± 3.24
3D hydrogel sample without MDA-MB-231 and without GNP	5.58 ± 1.14
Results for Negative GNPs	**33.66 ± 8.82**
Positive GNPs in MDA-MB-231 3D hydrogel sample	5707.33 ± 969.86
Positive GNP in 3D hydrogel sample without MDA-MB-231	408.40 ± 74.42
3D hydrogel sample without MDA-MB-231 and without GNP	5.58 ± 1.14
Results for Positive GNPs	**5293.34 ± 969.86**

Table 9. Average gold concentration in MDA-MB-231
3D hydrogel samples and in controls (GNPs in 3D hydrogel samples in absence of cell and 3 hydrogel samples in absence of cells and in absence of GNPs). The results for each charged GNPs were obtained by subtracting the averaged control values from the averaged concentration value for the MDA-MB-231 3D hydrogel samples.

Bibliography

[1] National Cancer Institute. *Cancer Statistics*; National Cancer Institute, 2016.

[2] McKinnell, R. G.; Parchment, R. E.; Peratoni, A. O.; Damjanov, I.; Pierce, B. *The Biological Basis of Cancer*, 2nd ed.; Cambridge University Press, 2006.

[3] Pardee, A. B.; Stein, G. S. *The Biology and Treatment of Cancer: Understanding Cancer*; Pardee, A. B., Stein, G. S., Eds.; John Wiley & Sons, Inc.: Hoboken, NJ, USA, 2008.

[4] Guan, X. Cancer Metastases: Challenges and Opportunities. *Acta Pharm. Sin. B* **2015**, *5* (5), 402–418.

[5] Steeg, P. S. Targeting Metastasis. *Nat. Rev. Cancer* **2016**, *16* (4), 201–218.

[6] Lyons, L. *Diagnosis and Treatment of Cancer*; Chelsea House, 2007.

[7] Pampaloni, F.; Reynaud, E. G.; Stelzer, E. H. K. The Third Dimension Bridges the Gap between Cell Culture and Live Tissue. *Nat. Rev. Mol. Cell Biol.* **2007**, *8* (10), 839–845.

[8] Xu, X.; Farach-Carson, M. C.; Jia, X. Three-Dimensional in Vitro Tumor Models for Cancer Research and Drug Evaluation. *Biotechnol. Adv.* **2014**, *32* (7), 1256–1268.

[9] Breslin, S.; O'Driscoll, L. Three-Dimensional Cell Culture: The Missing Link in Drug Discovery. *Drug Discov. Today* **2013**, *18* (5–6), 240–249.

[10] Kim, J. Bin. Three-Dimensional Tissue Culture Models in Cancer Biology. *Semin. Cancer Biol.* **2005**, *15* (5), 365–377.

[11] Katt, M. E.; Placone, A. L.; Wong, A. D.; Xu, Z. S.; Searson, P. C. In Vitro Tumor Models: Advantages, Disadvantages, Variables, and Selecting the Right Platform. *Front. Bioeng. Biotechnol.* **2016**, *4* (12), 1–14.

[12] Mehta, G.; Hsiao, A. Y.; Ingram, M.; Luker, G. D.; Takayama, S. Opportunities and Challenges for Use of Tumor Spheroids as Models to Test Drug Delivery and Efficacy. *J. Control. Release* **2012**, *164* (2), 192–204.

[13] Hutmacher, D. W. Biomaterials Offer Cancer Research the Third Dimension. *Nat. Mater.* **2010**, *9* (2), 90–93.

[14] Chan, B. P.; Leong, K. W. Scaffolding in Tissue Engineering: General Approaches and Tissue-Specific Considerations. *Eur. Spine J.* **2008**, *17 Suppl 4* (Suppl 4), 467–479.

[15] Chen, F.-M.; Liu, X. Advancing Biomaterials of Human Origin for Tissue Engineering. *Prog. Polym. Sci.* **2016**, *53*, 86–168.

[16] Okamoto, M.; John, B. Synthetic Biopolymer Nanocomposites for Tissue Engineering Scaffolds. *Prog. Polym. Sci.* **2013**, *38* (10), 1487–1503.

[17] Tamayol, A.; Akbari, M.; Annabi, N.; Paul, A.; Khademhosseini, A.; Juncker, D. Fiber-Based Tissue Engineering: Progress, Challenges, and Opportunities. *Biotechnology Advances*. September 2013, pp 669–687.

[18] Nam, Y. S.; Park, T. G. Biodegradable Polymeric Microcellular Foams by Modified Thermally Induced Phase Separation Method. *Biomaterials* **1999**, *20* (19), 1783–1790.

[19] Ghorbanian, S.; Qasaimeh, M. A.; Akbari, M.; Tamayol, A.; Juncker, D. Microfluidic Direct Writer with Integrated Declogging Mechanism for Fabricating Cell-Laden

Hydrogel Constructs. *Biomed. Microdevices* **2014**, *16* (3), 387–395.

[20] Akbari, M.; Tamayol, A.; Bagherifard, S.; Serex, L.; Mostafalu, P.; Faramarzi, N.; Mohammadi, M. H.; Khademhosseini, A. Textile Technologies and Tissue Engineering: A Path Toward Organ Weaving. *Adv. Healthc. Mater.* **2016**, *5* (7), 751–766.

[21] Nichol, J. W.; Koshy, S. T.; Bae, H.; Hwang, C. M.; Yamanlar, S.; Khademhosseini, A. Cell-Laden Microengineered Gelatin Methacrylate Hydrogels. *Biomaterials* **2010**, *31* (21), 5536–5544.

[22] Annabi, N.; Tamayol, A.; Uquillas, J. A.; Akbari, M.; Bertassoni, L. E.; Cha, C.; Camci-Unal, G.; Dokmeci, M. R.; Peppas, N. A.; Khademhosseini, A. 25th Anniversary Article: Rational Design and Applications of Hydrogels in Regenerative Medicine. *Adv. Mater.* **2014**, *26* (1), 85–124.

[23] Kharaziha, M.; Memic, A.; Akbari, M.; Brafman, D. A.; Nikkhah, M. Nano-Enabled Approaches for Stem Cell-Based Cardiac Tissue Engineering. *Adv. Healthc. Mater.* **2016**, *5* (13), 1533–1553.

[24] Nyga, A.; Cheema, U.; Loizidou, M. 3D Tumour Models: Novel in Vitro Approaches to Cancer Studies. *J. Cell Commun. Signal.* **2011**, *5* (3), 239–248.

[25] O’Brien, F. J. Biomaterials & Scaffolds for Tissue Engineering. *Mater. Today* **2011**, *14* (3), 88–95.

[26] van der Meer, A. D.; van den Berg, A. Organs-on-Chips: Breaking the in Vitro Impasse. *Integr. Biol. (Camb).* **2012**, *4* (5), 461–470.

[27] Huh, D.; Hamilton, G. A.; Ingber, D. E. From 3D Cell Culture to Organs-on-Chips. *Trends Cell Biol.* **2011**, *21* (12), 745–754.

[28] Selimović, S.; Dokmeci, M. R.; Khademhosseini, A. Organs-on-a-Chip for Drug Discovery. *Curr. Opin. Pharmacol.* **2013**, *13* (5), 829–833.

[29] Whitesides, G. M. The Origins and the Future of Microfluidics. *Nature* **2006**, *442* (7101), 368–373.

[30] Bhatia, S. N.; Ingber, D. E. Microfluidic Organs-on-Chips. *Nat. Biotechnol.* **2014**, *32* (8), 760–772.

[31] Tian, W. C.; Finehout, E. *Microfluidics for Biological Applications*; Springer US: Boston, MA, 2009.

[32] Damiati, S.; Kompella, U. B.; Damiati, S. A.; Kodzius, R. Microfluidic Devices for Drug Delivery Systems and Drug Screening. *Genes*. MDPI AG February 16, 2018, p 103.

[33] Hood, R. R.; Vreeland, W. N.; Devoe, D. L. Microfluidic Remote Loading for Rapid Single-Step Liposomal Drug Preparation. *Lab Chip* **2014**, *14* (17), 3359–3367.

[34] Quail, D. F.; Joyce, J. A. Microenvironmental Regulation of Tumor Progression and Metastasis. *Nat. Med.* **2013**, *19* (11), 1423–1437.

[35] Wilson, W. R.; Hay, M. P. Targeting Hypoxia in Cancer Therapy. *Nat. Rev. Cancer* **2011**, *11* (6), 393–410.

[36] Lu, P.; Weaver, V. M.; Werb, Z. The Extracellular Matrix: A Dynamic Niche in Cancer Progression. *J. Cell Biol.* **2012**, *196* (4), 395–406.

[37] Valente, K. P.; Khetani, S.; Kolahchi, A. R.; Sanati-Nezhad, A.; Suleman, A.; Akbari, M. Microfluidic Technologies for Anticancer Drug Studies. *Drug Discovery Today*. Elsevier Ltd November 1, 2017, pp 1654–1670.

[38] Butcher, D. T.; Alliston, T.; Weaver, V. M. A Tense Situation: Forcing Tumour Progression. *Nat. Rev. Cancer* **2009**, *9* (2), 108–122.

[39] Frantz, C.; Stewart, K. M.; Weaver, V. M. The Extracellular Matrix at a Glance. *J. Cell Sci.* **2010**, *123* (Pt 24), 4195–4200.

[40] Berean, K.; Ou, J. Z.; Nour, M.; Latham, K.; McSweeney, C.; Paull, D.; Halim, A.; Kentish, S.; Doherty, C. M.; Hill, A. J.; Kalantar-Zadeh, K. The Effect of Crosslinking Temperature on the Permeability of PDMS Membranes: Evidence of Extraordinary CO2and CH4gas Permeation. *Sep. Purif. Technol.* **2014**, *122*, 96–104.

[41] Minchinton, A. I.; Tannock, I. F. Drug Penetration in Solid Tumours. *Nat. Rev. Cancer* **2006**, *6* (8), 583–592.

[42] Hanahan, D.; Weinberg, R. A. Hallmarks of Cancer: The Next Generation. *Cell* **2011**, *144*, 646–674.

[43] Munson, J. M.; Shieh, A. C. Interstitial Fluid Flow in Cancer: Implications for Disease Progression and Treatment. *Cancer Manag. Res.* **2014**, *6*, 317–328.

[44] Polacheck, W. J.; Zervantonakis, I. K.; Kamm, R. D. Tumor Cell Migration in Complex Microenvironments. *Cell. Mol. Life Sci.* **2013**, *70* (8), 1335–1356.

[45] Trédan, O.; Galmarini, C. M.; Patel, K.; Tannock, I. F. Drug Resistance and the Solid Tumor Microenvironment. *J. Natl. Cancer Inst.* **2007**, *99* (19), 1441–1454.

[46] Heldin, C.-H.; Rubin, K.; Pietras, K.; Ostman, A. High Interstitial Fluid Pressure - an Obstacle in Cancer Therapy. *Nat. Rev. Cancer* **2004**, *4* (10), 806–813.

[47] Salnikov, A. V; Iversen, V. V; Koisti, M.; Sundberg, C.; Johansson, L.; Stuhr, L. B.; Sjöquist, M.; Ahlström, H.; Reed, R. K.; Rubin, K. Lowering of Tumor Interstitial Fluid Pressure Specifically Augments Efficacy of Chemotherapy. *FASEB J.* **2003**, *17* (12), 1756–1758.

[48] Chiche, J.; Brahimi-Horn, M. C.; Pouysségur, J. Tumour Hypoxia Induces a Metabolic Shift Causing Acidosis: A Common Feature in Cancer. *J. Cell. Mol. Med.* **2010**, *14* (4), 771–794.

[49] Eales, K. L.; Hollinshead, K. E. R.; Tennant, D. A. Hypoxia and Metabolic Adaptation of Cancer Cells. *Oncogenesis* **2016**, *5*, e190.

[50] Nishida, N.; Yano, H.; Nishida, T.; Kamura, T.; Kojiro, M. Angiogenesis in Cancer. *Vasc. Health Risk Manag.* **2006**, *2* (3), 213–219.

[51] Weis, S. M.; Cheresh, D. A. Tumor Angiogenesis: Molecular Pathways and Therapeutic Targets. *Nat. Med.* **2011**, *17* (11), 1359–1370.

[52] Infanger, D. W.; Lynch, M. E.; Fischbach, C. Engineered Culture Models for Studies of Tumor-Microenvironment Interactions. *Annu. Rev. Biomed. Eng.* **2013**, *15* (1), 29–53.

[53] Folkman, J. Role of Angiogenesis in Tumor Growth and Metastasis. *Semin. Oncol.* **2002**, *29* (6 Suppl 16), 15–18.

[54] Karimi, M.; Bahrami, S.; Mirshekari, H.; Basri, S. M. M.; Nik, A. B.; Aref, A. R.; Akbari, M.; Hamblin, M. R. Microfluidic Systems for Stem Cell-Based Neural Tissue Engineering. *Lab Chip* **2016**, *16*, 2551–2571.

[55] Mohammadi, M. H.; Heidary Araghi, B.; Beydaghi, V.; Geraili, A.; Moradi, F.; Jafari, P.; Janmaleki, M.; Valente, K. P.; Akbari, M.; Sanati-Nezhad, A. Skin Diseases Modeling Using Combined Tissue Engineering and Microfluidic Technologies. *Adv. Healthc. Mater.* **2016**, *5*, 2459–2480.

[56] Hasan, A.; Paul, A.; Vrana, N. E.; Zhao, X.; Memic, A.; Hwang, Y. S.; Dokmeci, M. R.; Khademhosseini, A. Microfluidic Techniques for Development of 3D Vascularized Tissue. *Biomaterials* **2014**, *35* (26), 7308–7325.

[57] American Cancer Society. *Cancer Facts & Figures 2017*; American Cancer Society, 2017.

[58] Huang, C. P.; Lu, J.; Seon, H.; Lee, A. P.; Flanagan, L. A.; Kim, H.-Y.; Putnam, A. J.; Jeon, N. L. Engineering Microscale Cellular Niches for Three-Dimensional Multicellular Co-Cultures. *Lab Chip* **2009**, *9* (12), 1740–1748.

[59] Choi, Y.; Hyun, E.; Seo, J.; Blundell, C.; Kim, H. C.; Lee, E.; Lee, S. H.; Moon, A.; Moon, W. K.; Huh, D. A Microengineered Pathophysiological Model of Early-Stage Breast Cancer. *Lab Chip* **2015**, *15* (16), 3350–3357.

[60] Bersini, S.; Jeon, J. S.; Dubini, G.; Arrigoni, C.; Chung, S.; Charest, J. L.; Moretti, M.; Kamm, R. D. A Microfluidic 3D in Vitro Model for Specificity of Breast Cancer Metastasis to Bone. *Biomaterials* **2014**, *35* (8), 2454–2461.

[61] Chung, S.; Sudo, R.; Vickerman, V.; Zervantonakis, I. K.; Kamm, R. D. Microfluidic Platforms for Studies of Angiogenesis, Cell Migration, and Cell–Cell Interactions. *Ann. Biomed. Eng.* **2010**, *38* (3), 1164–1177.

[62] Shin, Y.; Han, S.; Jeon, J. S.; Yamamoto, K.; Zervantonakis, I. K.; Sudo, R.; Kamm, R. D.; Chung, S. Microfluidic Assay for Simultaneous Culture of Multiple Cell Types on Surfaces or within Hydrogels. *Nat. Protoc.* **2012**, *7* (7), 1247–1259.

[63] Jeon, J. S.; Zervantonakis, I. K.; Chung, S.; Kamm, R. D.; Charest, J. L. In Vitro Model of Tumor Cell Extravasation. *PLoS One* **2013**, *8* (2), e56910.

[64] Hsu, Y.-L.; Hou, M.-F.; Kuo, P.-L.; Huang, Y.-F.; Tsai, E.-M. Breast Tumor-Associated Osteoblast-Derived CXCL5 Increases Cancer Progression by ERK/MSK1/Elk-1/Snail Signaling Pathway. *Oncogene* **2013**, *32* (37), 4436–4447.

[65] Xu, Z.; Li, E.; Guo, Z.; Yu, R.; Hao, H.; Xu, Y.; Sun, Z.; Li, X.; Lyu, J.; Wang, Q. Design and Construction of a Multi-Organ Microfluidic Chip Mimicking the in Vivo Microenvironment of Lung Cancer Metastasis. *ACS Appl. Mater. Interfaces* **2016**, *8* (39), 25840–25847.

[66] Ma, H.; Xu, H.; Qin, J. Biomimetic Tumor Microenvironment on a Microfluidic Platform. *Biomicrofluidics* **2013**, *7* (1), 11501–11513.

[67] Young, E. W. K. Cells, Tissues, and Organs on Chips: Challenges and Opportunities for the Cancer Tumor Microenvironment. *Integr. Biol. (Camb).* **2013**, *5* (9), 1096–1109.

[68] Murthy, S. K. Nanoparticles in Modern Medicine: State of the Art and Future Challenges.

Int. J. Nanomedicine **2007**, *2* (2), 129–141.

[69] Barua, S.; Mitragotri, S. Challenges Associated with Penetration of Nanoparticles across Cell and Tissue Barriers: A Review of Current Status and Future Prospects. *Nano Today* **2014**, *9* (2), 223–243.

[70] Gullotti, E.; Yeo, Y. Extracellularly Activated Nanocarriers: A New Paradigm of Tumor Targeted Drug Delivery. *Mol. Pharm.* **2009**, *6* (4), 1041–1051.

[71] Chauhan, V. P.; Stylianopoulos, T.; Boucher, Y.; Jain, R. K. Delivery of Molecular and Nanoscale Medicine to Tumors: Transport Barriers and Strategies. *Annu. Rev. Chem. Biomol. Eng.* **2011**, *2* (1), 281–298.

[72] Alexis, F.; Pridgen, E.; Molnar, L. K.; Farokhzad, O. C. Factors Affecting the Clearance and Biodistribution of Polymeric Nanoparticles. *Mol. Pharm.* **2008**, *5* (4), 505–515.

[73] Holback, H.; Yeo, Y. Intratumoral Drug Delivery with Nanoparticulate Carriers. *Pharm. Res.* **2011**, *28* (8), 1819–1830.

[74] Howard, M. D.; Jay, M.; Dziubla, T. D.; Lu, X. PEGylation of Nanocarrier Drug Delivery Systems: State of the Art. *J. Biomed. Nanotechnol.* **2008**, *4* (2), 133–148.

[75] OWENSIII, D.; PEPPAS, N. Opsonization, Biodistribution, and Pharmacokinetics of Polymeric Nanoparticles. *Int. J. Pharm.* **2006**, *307* (1), 93–102.

[76] Black, K. C. L.; Wang, Y.; Luehmann, H. P.; Cai, X.; Xing, W.; Pang, B.; Zhao, Y.; Cutler, C. S.; Wang, L. V.; Liu, Y.; Xia, Y. Radioactive ^{198} Au-Doped Nanostructures with Different Shapes for *In Vivo* Analyses of Their Biodistribution, Tumor Uptake, and Intratumoral Distribution. *ACS Nano* **2014**, *8* (5), 4385–4394.

[77] Ngwa, W.; Kumar, R.; Sridhar, S.; Korideck, H.; Zygmanski, P.; Cormack, R. A.; Berbeco, R.; Makrigiorgos, G. M. Targeted Radiotherapy with Gold Nanoparticles: Current Status and Future Perspectives. *Nanomedicine (Lond).* **2014**, *9* (7), 1063–1082.

[78] McQuaid, H. N.; Muir, M. F.; Taggart, L. E.; McMahon, S. J.; Coulter, J. A.; Hyland, W. B.; Jain, S.; Butterworth, K. T.; Schettino, G.; Prise, K. M.; Hirst, D. G.; Botchway, S. W.; Currell, F. J. Imaging and Radiation Effects of Gold Nanoparticles in Tumour Cells. *Sci. Rep.* **2016**, *6*, 19442.

[79] Kong, T.; Zeng, J.; Wang, X.; Yang, X.; Yang, J.; McQuarrie, S.; McEwan, A.; Roa, W.; Chen, J.; Xing, J. Z. Enhancement of Radiation Cytotoxicity in Breast-Cancer Cells by Localized Attachment of Gold Nanoparticles. *Small* **2008**, *4* (9), 1537–1543.

[80] Chattopadhyay, N.; Cai, Z.; Pignol, J.-P.; Keller, B.; Lechtman, E.; Bendayan, R.; Reilly, R. M. Design and Characterization of HER-2-Targeted Gold Nanoparticles for Enhanced X-Radiation Treatment of Locally Advanced Breast Cancer. *Mol. Pharm.* **2010**, *7* (6), 2194–2206.

[81] Starkewolf, Z. B.; Miyachi, L.; Wong, J.; Guo, T. X-Ray Triggered Release of Doxorubicin from Nanoparticle Drug Carriers for Cancer Therapy. *Chem. Commun.* **2013**, *49* (25), 2545.

[82] Nicodemus, G. D.; Bryant, S. J. Cell Encapsulation in Biodegradable Hydrogels for Tissue Engineering Applications. *Tissue Eng. Part B Rev.* **2008**, *14* (2), 149–165.

[83] Hoare, T. R.; Kohane, D. S. Hydrogels in Drug Delivery: Progress and Challenges.

Polymer (Guildf). **2008**, *49* (8), 1993–2007.

[84] Quignard, S.; Hélary, C.; Boissière, M.; Fullana, J.-M.; Lagrée, P.-Y.; Coradin, T. Behaviour of Silica Nanoparticles in Dermis-like Cellularized Collagen Hydrogels. *Biomater. Sci.* **2014**, *2* (4), 484–492.

[85] Tomasetti, L.; Liebl, R.; Wastl, D. S.; Breunig, M. Influence of PEGylation on Nanoparticle Mobility in Different Models of the Extracellular Matrix. *Eur. J. Pharm. Biopharm.* **2016**, *108*, 145–155.

[86] Jiang, W.; Kim, B. Y.; Rutka, J. T.; Chan, W. C. Advances and Challenges of Nanotechnology-Based Drug Delivery Systems. *Expert Opin. Drug Deliv.* **2007**, *4* (6), 621–633.

[87] Raeesi, V.; Chan, W. C. W.; Sturgis, J. E.; McCallister, M. E.; Robinson, J. P.; Voytik-Harbin, S. L.; Lin, B.; Yin, Q.; Zhang, Z.; Chen, C.; Wang, J.; Zhang, W.; Li, Y.; Lammers, T.; Sabnis, A.; Schnipper, E.; Song, J. J.; Song, Y. H.; Summa, J.; Tompsett, D.; Troiano, G.; Hoven, T. V. G.; Wright, J.; LoRusso, P.; Kantoff, P. W.; Bander, N. H.; Sweeney, C.; Farokhzad, O. C.; Langer, R.; Zale, S. Improving Nanoparticle Diffusion through Tumor Collagen Matrix by Photo-Thermal Gold Nanorods. *Nanoscale* **2016**, *8* (25), 12524–12530.

[88] Albanese, A.; Lam, A. K.; Sykes, E. A.; Rocheleau, J. V; Chan, W. C. W. Tumour-on-a-Chip Provides an Optical Window into Nanoparticle Tissue Transport. *Nat. Commun.* **2013**, *4*, 2718.

[89] Kwak, B.; Ozcelikkale, A.; Shin, C. S.; Park, K.; Han, B. Simulation of Complex Transport of Nanoparticles around a Tumor Using Tumor-Microenvironment-on-Chip. *J. Control. Release* **2014**, *194*, 157–167.

[90] Kumari, P.; Ghosh, B.; Biswas, S. Nanocarriers for Cancer-Targeted Drug Delivery. *J. Drug Target.* **2016**, *24* (3), 179–191.

[91] Torchilin, V. Tumor Delivery of Macromolecular Drugs Based on the EPR Effect. *Advanced Drug Delivery Reviews*. Elsevier March 18, 2011, pp 131–135.

[92] Sindhwani, S.; Syed, A. M.; Ngai, J.; Kingston, B. R.; Maiorino, L.; Rothschild, J.; MacMillan, P.; Zhang, Y.; Rajesh, N. U.; Hoang, T.; Wu, J. L. Y.; Wilhelm, S.; Zilman, A.; Gadde, S.; Sulaiman, A.; Ouyang, B.; Lin, Z.; Wang, L.; Egeblad, M.; Chan, W. C. W. The Entry of Nanoparticles into Solid Tumours. *Nat. Mater.* **2020**, *19* (5), 566–575.

[93] Yu, P.; Yu, H.; Guo, C.; Cui, Z.; Chen, X.; Yin, Q.; Zhang, P.; Yang, X.; Cui, H.; Li, Y. Reversal of Doxorubicin Resistance in Breast Cancer by Mitochondria-Targeted PH-Responsive Micelles. *Acta Biomater.* **2015**, *14*, 115–124.

[94] Lee, E. S.; Kim, J. H.; Sim, T.; Youn, Y. S.; Lee, B. J.; Oh, Y. T.; Oh, K. T. A Feasibility Study of a PH Sensitive Nanomedicine Using Doxorubicin Loaded Poly(Aspartic Acid-Graft-Imidazole)-Block-Poly(Ethylene Glycol) Micelles. *J. Mater. Chem. B* **2014**, *2* (9), 1152–1159.

[95] Sun, Z.; Song, C.; Wang, C.; Hu, Y.; Wu, J. Hydrogel-Based Controlled Drug Delivery for Cancer Treatment: A Review. *Mol. Pharm.* **2020**, *17* (2), 373–391.

[96] Cai, Z.; Zhang, H.; Wei, Y.; Wei, Y.; Xie, Y.; Cong, F. Reduction- and PH-Sensitive Hyaluronan Nanoparticles for Delivery of Iridium(III) Anticancer Drugs.

Biomacromolecules **2017**, *18* (7), 2102–2117.

[97] Raza, F.; Zhu, Y.; Chen, L.; You, X.; Zhang, J.; Khan, A.; Khan, M. W.; Hasnat, M.; Zafar, H.; Wu, J.; Ge, L. Paclitaxel-Loaded PH Responsive Hydrogel Based on Self-Assembled Peptides for Tumor Targeting. *Biomater. Sci.* **2019**, *7* (5), 2023–2036.

[98] Xu, C.; Yan, Y.; Tan, J.; Yang, D.; Jia, X.; Wang, L.; Xu, Y.; Cao, S.; Sun, S. Biodegradable Nanoparticles of Polyacrylic Acid–Stabilized Amorphous CaCO $_3$ for Tunable PH-Responsive Drug Delivery and Enhanced Tumor Inhibition. *Adv. Funct. Mater.* **2019**, *29* (24), 1808146.

[99] Ahmad, M. Z.; Akhter, S.; Jain, G. K.; Rahman, M.; Pathan, S. A.; Ahmad, F. J.; Khar, R. K. Metallic Nanoparticles: Technology Overview and Drug Delivery Applications in Oncology. *Expert Opinion on Drug Delivery*. Expert Opin Drug Deliv August 2010, pp 927–942.

[100] Han, L.; Tang, C.; Yin, C. PH-Responsive Core-Shell Structured Nanoparticles for Triple-Stage Targeted Delivery of Doxorubicin to Tumors. *ACS Appl. Mater. Interfaces* **2016**, *8* (36), 23498–23508.

[101] Ellis, E.; Zhang, K.; Lin, Q.; Ye, E.; Poma, A.; Battaglia, G.; Loh, X. J.; Lee, T. C. Biocompatible PH-Responsive Nanoparticles with a Core-Anchored Multilayer Shell of Triblock Copolymers for Enhanced Cancer Therapy. *J. Mater. Chem. B* **2017**, *5* (23), 4421–4425.

[102] Yilmaz, G.; Guler, E.; Geyik, C.; Demir, B.; Ozkan, M.; Odaci Demirkol, D.; Ozcelik, S.; Timur, S.; Remzi Becer, C. PH Responsive Glycopolymer Nanoparticles for Targeted Delivery of Anti-Cancer Drugs. *Mol. Syst. Des. Eng.* **2018**, *3* (1), 150–158.

[103] Hansen, R. K.; Bissell, M. J. Tissue Architecture and Breast Cancer: The Role of Extracellular Matrix and Steroid Hormones. *Endocr. Relat. Cancer* **2000**, *7* (2), 95–113.

[104] Rønnov-Jessen, L.; Petersen, O. W.; Bissell, M. J. Cellular Changes Involved in Conversion of Normal to Malignant Breast: Importance of the Stromal Reaction. *Physiol. Rev.* **1996**, *76* (1), 69–125.

[105] Muschler, J.; Streuli, C. H. Cell-Matrix Interactions in Mammary Gland Development and Breast Cancer. *Cold Spring Harb. Perspect. Biol.* **2010**, *2* (10), a003202–a003202.

[106] Asghar, W.; El Assal, R.; Shafiee, H.; Pitteri, S.; Paulmurugan, R.; Demirci, U. Engineering Cancer Microenvironments for in Vitro 3-D Tumor Models. *Mater. Today* **2015**, *18* (10), 539–553.

[107] Paszek, M. J.; Zahir, N.; Johnson, K. R.; Lakins, J. N.; Rozenberg, G. I.; Gefen, A.; Reinhart-King, C. A.; Margulies, S. S.; Dembo, M.; Boettiger, D.; Hammer, D. A.; Weaver, V. M. Tensional Homeostasis and the Malignant Phenotype. *Cancer Cell* **2005**, *8* (3), 241–254.

[108] Van Den Bulcke, A. I.; Bogdanov, B.; De Rooze, N.; Schacht, E. H.; Cornelissen, M.; Berghmans, H. Structural and Rheological Properties of Methacrylamide Modified Gelatin Hydrogels. *Biomacromolecules* **2000**, *1* (1), 31–38.

[109] Yue, K.; Trujillo-de Santiago, G.; Alvarez, M. M.; Tamayol, A.; Annabi, N.; Khademhosseini, A. Synthesis, Properties, and Biomedical Applications of Gelatin Methacryloyl (GelMA) Hydrogels. *Biomaterials* **2015**, *73*, 254–271.

[110] Li, X.; Zhang, J.; Kawazoe, N.; Chen, G. Fabrication of Highly Crosslinked Gelatin Hydrogel and Its Influence on Chondrocyte Proliferation and Phenotype. *Polymers (Basel).* **2017**, *9* (8).

[111] Shirahama, H.; Lee, B. H.; Tan, L. P.; Cho, N. J. Precise Tuning of Facile One-Pot Gelatin Methacryloyl (GelMA) Synthesis. *Sci. Rep.* **2016**, *6* (1), 31036.

[112] Sun, M.; Sun, X.; Wang, Z.; Guo, S.; Yu, G.; Yang, H. Synthesis and Properties of Gelatin Methacryloyl (GelMA) Hydrogels and Their Recent Applications in Load-Bearing Tissue. *Polymers*. MDPI AG 2018.

[113] Xiao, S.; Zhao, T.; Wang, J.; Wang, C.; Du, J.; Ying, L.; Lin, J.; Zhang, C.; Hu, W.; Wang, L.; Xu, K. Gelatin Methacrylate (GelMA)-Based Hydrogels for Cell Transplantation: An Effective Strategy for Tissue Engineering. *Stem Cell Reviews and Reports*. Humana Press Inc. October 1, 2019, pp 664–679.

[114] Miri, A. K.; Hosseinabadi, H. G.; Cecen, B.; Hassan, S.; Zhang, Y. S. Permeability Mapping of Gelatin Methacryloyl Hydrogels. *Acta Biomater.* **2018**, *77*, 38–47.

[115] Topkaya, S. N. Gelatin Methacrylate (GelMA) Mediated Electrochemical DNA Biosensor for DNA Hybridization. *Biosens. Bioelectron.* **2015**, *64*, 456–461.

[116] Sung, K. E.; Su, G.; Pehlke, C.; Trier, S. M.; Eliceiri, K. W.; Keely, P. J.; Friedl, A.; Beebe, D. J. Control of 3-Dimensional Collagen Matrix Polymerization for Reproducible Human Mammary Fibroblast Cell Culture in Microfluidic Devices. *Biomaterials* **2009**, *30* (27), 4833–4841.

[117] Anna, S. L.; Bontoux, N.; Stone, H. A. Formation of Dispersions Using “Flow Focusing” in Microchannels. *Appl. Phys. Lett.* **2003**, *82* (3), 364–366.

[118] Lagus, T. P.; Edd, J. F. A Review of the Theory, Methods and Recent Applications of High-Throughput Single-Cell Droplet Microfluidics. *J. Phys. D. Appl. Phys.* **2013**, *46* (11), 114005.

[119] Dendukuri, D.; Tsoi, K.; Hatton, T. A.; Doyle, P. S. Controlled Synthesis of Nonspherical Microparticles Using Microfluidics. *Langmuir* **2005**, *21* (6), 2113–2116.

[120] Nunes, J. K.; Tsai, S. S. H.; Wan, J.; Stone, H. A. Dripping and Jetting in Microfluidic Multiphase Flows Applied to Particle and Fibre Synthesis. *J. Phys. D. Appl. Phys.* **2013**, *46* (11), 114002.

[121] Rayleigh, Lord. VI. On the Capillary Phenomena of Jets. *Proc. R. Soc. London* **1879**, *29* (196–199), 71–97.

[122] Samanipour, R.; Wang, Z.; Ahmadi, A.; Kim, K. Experimental and Computational Study of Microfluidic Flow-Focusing Generation of Gelatin Methacrylate Hydrogel Droplets. *J. Appl. Polym. Sci* **2016**, 43701.

[123] Cooper, D. R.; Bekah, D.; Nadeau, J. L. Gold Nanoparticles and Their Alternatives for Radiation Therapy Enhancement. *Front. Chem.* **2014**, *2*, 86.

[124] Haume, K.; Rosa, S.; Grellet, S.; Śmiałek, M. A.; Butterworth, K. T.; Solov’yov, A. V.; Prise, K. M.; Golding, J.; Mason, N. J. Gold Nanoparticles for Cancer Radiotherapy: A Review. *Cancer Nanotechnol.* **2016**, *7* (1), 8.

[125] Krämer, M.; Durante, M. Ion Beam Transport Calculations and Treatment Plans in

Particle Therapy. *Eur. Phys. J. D* **2010**, *60* (1), 195–202.

[126] Kobayashi, K.; Usami, N.; Porcel, E.; Lacombe, S.; Le Sech, C. Enhancement of Radiation Effect by Heavy Elements. *Mutat. Res. Mutat. Res.* **2010**, *704* (1), 123–131.

[127] Butterworth, K. T.; McMahon, S. J.; Currell, F. J.; Prise, K. M. Physical Basis and Biological Mechanisms of Gold Nanoparticle Radiosensitization. *Nanoscale* **2012**, *4* (16), 4830.

[128] Hainfeld, J. F.; Dilmanian, F. A.; Slatkin, D. N.; Smilowitz, H. M. Radiotherapy Enhancement with Gold Nanoparticles. *J. Pharm. Pharmacol.* **2008**, *60* (8), 977–985.

[129] Kwatra, D.; Venugopal, A.; Anant, S. Nanoparticles in Radiation Therapy: A Summary of Various Approaches to Enhance Radiosensitization in Cancer. *Transl. Cancer Res.* **2013**, *2* (4), 330–342.

[130] Rofstad, E. K.; Galappathi, K.; Mathiesen, B. S. Tumor Interstitial Fluid Pressure-A Link between Tumor Hypoxia, Microvascular Density, and Lymph Node Metastasis. *Neoplasia* **2014**, *16* (7), 586–594.

[131] Bordeleau, F.; Mason, B. N.; Lollis, E. M.; Mazzola, M.; Zanotelli, M. R.; Somasegar, S.; Califano, J. P.; Montague, C.; LaValley, D. J.; Huynh, J.; Mencia-Trinchant, N.; Negrón Abril, Y. L.; Hassane, D. C.; Bonassar, L. J.; Butcher, J. T.; Weiss, R. S.; Reinhart-King, C. A. Matrix Stiffening Promotes a Tumor Vasculature Phenotype. *Proc. Natl. Acad. Sci.* **2017**, *114* (3), 492–497.

[132] Aguirre-Ghiso, J. A.; Estrada, Y.; Liu, D.; Ossowski, L. ERKMAPKactivity as a Determinant of Tumor Growth and Dormancy; Regulation by P38SAPK. *Cancer Res.* **2003**, *63* (7), 1684–1695.

[133] Dewhirst, M. W.; Secomb, T. W. Transport of Drugs from Blood Vessels to Tumour Tissue. *Nat. Rev. Cancer* **2017**, *17* (12), 738–750.

[134] Grzelczak, M.; Pérez-Juste, J.; Mulvaney, P.; Liz-Marzán, L. M. Shape Control in Gold Nanoparticle Synthesis. *Chem. Soc. Rev.* **2008**, *37* (9), 1783.

[135] Zhang, M.; Nigwekar, P.; Castaneda, B.; Hoyt, K.; Joseph, J. V.; di Sant'Agnese, A.; Messing, E. M.; Strang, J. G.; Rubens, D. J.; Parker, K. J. Quantitative Characterization of Viscoelastic Properties of Human Prostate Correlated with Histology. *Ultrasound Med. Biol.* **2008**, *34* (7), 1033–1042.

[136] Sobral-Filho, R. G.; Brito-Silva, A. M.; Isabelle, M.; Jirasek, A.; Lum, J. J.; Brolo, A. G. Plasmonic Labeling of Subcellular Compartments in Cancer Cells: Multiplexing with Fine-Tuned Gold and Silver Nanoshells. *Chem. Sci.* **2017**, *8* (4), 3038–3046.

[137] Kong, F.-Y.; Zhang, J.-W.; Li, R.-F.; Wang, Z.-X.; Wang, W.-J.; Wang, W. Unique Roles of Gold Nanoparticles in Drug Delivery, Targeting and Imaging Applications. *Molecules* **2017**, *22* (9), 1445.

[138] Han, G.; Ghosh, P.; Rotello, V. M. Functionalized Gold Nanoparticles for Drug Delivery. *Nanomedicine* **2007**, *2* (1), 113–123.

[139] Dreaden, E. C.; Austin, L. A.; Mackey, M. A.; El-Sayed, M. A. Size Matters: Gold Nanoparticles in Targeted Cancer Drug Delivery. *Ther. Deliv.* **2012**, *3* (4), 457–478.

[140] Bae, Y. H.; Park, K. Targeted Drug Delivery to Tumors: Myths, Reality and Possibility. *J.*

Control. Release **2011**, *153* (3), 198–205.

[141] Park, K. Facing the Truth about Nanotechnology in Drug Delivery. *ACS Nano* **2013**, *7* (9), 7442–7447.

[142] Galley, H. F.; Webster, N. R. Physiology of the Endothelium. *Br. J. Anaesth.* **2004**, *93* (1), 105–113.

[143] Gross, W.; Kress, H. Simultaneous Measurement of the Young's Modulus and the Poisson Ratio of Thin Elastic Layers. *Soft Matter* **2017**, *13* (5), 1048–1055.

[144] Lee, D.; Rahman, M. M.; Zhou, Y.; Ryu, S. Three-Dimensional Confocal Microscopy Indentation Method for Hydrogel Elasticity Measurement. *Langmuir* **2015**, *31* (35), 9684–9693.

[145] Buxboim, A.; Rajagopal, K.; Brown, A. E. X.; Discher, D. E. How Deeply Cells Feel: Methods for Thin Gels. *J. Phys. Condens. Matter* **2010**, *22* (19), 194116.

[146] Hoffman, A. S. Hydrogels for Biomedical Applications. *Adv. Drug Deliv. Rev.* **2012**, *64*, 18–23.

[147] Tibbitt, M. W.; Anseth, K. S. Hydrogels as Extracellular Matrix Mimics for 3D Cell Culture. *Biotechnol. Bioeng.* **2009**, *103* (4), 655–663.

[148] Yoon, H. J.; Shin, S. R.; Cha, J. M.; Lee, S.-H.; Kim, J.-H.; Do, J. T.; Song, H.; Bae, H. Cold Water Fish Gelatin Methacryloyl Hydrogel for Tissue Engineering Application. *PLoS One* **2016**, *11* (10), e0163902.

[149] Loessner, D.; Meinert, C.; Kaemmerer, E.; Martine, L. C.; Yue, K.; Levett, P. A.; Klein, T. J.; Melchels, F. P. W.; Khademhosseini, A.; Hutmacher, D. W. Functionalization, Preparation and Use of Cell-Laden Gelatin Methacryloyl–Based Hydrogels as Modular Tissue Culture Platforms. *Nat. Protoc.* **2016**, *11* (4), 727–746.

[150] Shoulders, M. D.; Raines, R. T. Collagen Structure and Stability. *Annu. Rev. Biochem.* **2009**, *78* (1), 929–958.

[151] Lodish, H. *Molecular Cell Biology*; W.H. Freeman, 2008.

[152] Zhou, L.; Tan, G.; Tan, Y.; Wang, H.; Liao, J.; Ning, C. Biomimetic Mineralization of Anionic Gelatin Hydrogels: Effect of Degree of Methacrylation. *RSC Adv.* **2014**, *4* (42), 21997–22008.

[153] Lai, V. K.; Nedrelow, D. S.; Lake, S. P.; Kim, B.; Weiss, E. M.; Tranquillo, R. T.; Barocas, V. H. Swelling of Collagen-Hyaluronic Acid Co-Gels: An In Vitro Residual Stress Model. *Ann. Biomed. Eng.* **2016**, *44* (10), 2984–2993.

[154] Yanagishita, M. Function of Proteoglycans in the Extracellular Matrix. *Pathol. Int.* **1993**, *43* (6), 283–293.

[155] Stylianopoulos, T.; Poh, M. Z.; Insin, N.; Bawendi, M. G.; Fukumura, D.; Munn, L. L.; Jain, R. K. Diffusion of Particles in the Extracellular Matrix: The Effect of Repulsive Electrostatic Interactions. *Biophys. J.* **2010**, *99* (5), 1342–1349.

[156] Tomasetti, L.; Breunig, M. Preventing Obstructions of Nanosized Drug Delivery Systems by the Extracellular Matrix. *Adv. Healthc. Mater.* **2018**, *7* (3), 1700739.

[157] Wei, B.; Zhou, X.; Liang, C.; Zheng, X.; Lei, P.; Fang, J.; Han, X.; Wang, L.; Qi, C.; Wei,

H. Human Colorectal Cancer Progression Correlates with LOX-Induced ECM Stiffening. *Int. J. Biol. Sci.* **2017**, *13* (11), 1450–1457.

[158] Acerbi, I.; Cassereau, L.; Dean, I.; Shi, Q.; Au, A.; Park, C.; Chen, Y. Y.; Liphardt, J.; Hwang, E. S.; Weaver, V. M. Human Breast Cancer Invasion and Aggression Correlates with ECM Stiffening and Immune Cell Infiltration. *Integr. Biol.* **2015**, *7* (10), 1120–1134.

[159] Wells, R. G. Tissue Mechanics and Fibrosis. *Biochim. Biophys. Acta - Mol. Basis Dis.* **2013**, *1832* (7), 884–890.

[160] Barnes, J. M.; Przybyla, L.; Weaver, V. M. Tissue Mechanics Regulate Brain Development, Homeostasis and Disease. *J. Cell Sci.* **2017**, *130* (1), 71–82.

[161] Stewart, D. C.; Rubiano, A.; Dyson, K.; Simmons, C. S. Mechanical Characterization of Human Brain Tumors from Patients and Comparison to Potential Surgical Phantoms. *PLoS One* **2017**, *12* (6), e0177561.

[162] Kawano, S.; Kojima, M.; Higuchi, Y.; Sugimoto, M.; Ikeda, K.; Sakuyama, N.; Takahashi, S.; Hayashi, R.; Ochiai, A.; Saito, N. Assessment of Elasticity of Colorectal Cancer Tissue, Clinical Utility, Pathological and Phenotypical Relevance. *Cancer Sci.* **2015**, *106* (9), 1232–1239.

[163] Li, J.; Jamin, Y.; Boult, J. K. R.; Cummings, C.; Waterton, J. C.; Ulloa, J.; Sinkus, R.; Bamber, J. C.; Robinson, S. P. Tumour Biomechanical Response to the Vascular Disrupting Agent ZD6126 in Vivo Assessed by Magnetic Resonance Elastography. *Br. J. Cancer* **2014**, *110* (7), 1727–1732.

[164] Jugé, L.; Doan, B.-T.; Seguin, J.; Albuquerque, M.; Larrat, B.; Mignet, N.; Chabot, G. G.; Scherman, D.; Paradis, V.; Vilgrain, V.; Van Beers, B. E.; Sinkus, R. Colon Tumor Growth and Antivascular Treatment in Mice: Complementary Assessment with MR Elastography and Diffusion-Weighted MR Imaging. *Radiology* **2012**, *264* (2), 436–444.

[165] Janmey, P. A.; Miller, R. T. Mechanisms of Mechanical Signaling in Development and Disease. *J. Cell Sci.* **2011**, *124* (1), 9–18.

[166] Lee, D. H.; Lee, J. M.; Yoon, J. H.; Kim, Y. J.; Lee, J. H.; Yu, S. J.; Han, J. K. Liver Stiffness Measured by Two-Dimensional Shear-Wave Elastography: Prognostic Value after Radiofrequency Ablation for Hepatocellular Carcinoma. *Liver Cancer* **2018**, *7* (1), 65–75.

[167] Lu, Q.; Ling, W.; Lu, C.; Li, J.; Ma, L.; Quan, J.; He, D.; Liu, J.; Yang, J.; Wen, T.; Wu, H.; Zhu, H.; Luo, Y. Hepatocellular Carcinoma: Stiffness Value and Ratio to Discriminate Malignant from Benign Focal Liver Lesions. *Radiology* **2015**, *275* (3), 880–888.

[168] Miyazawa, A.; Ito, S.; Asano, S.; Tanaka, I.; Sato, M.; Kondo, M.; Hasegawa, Y. Regulation of PD-L1 Expression by Matrix Stiffness in Lung Cancer Cells. *Biochem. Biophys. Res. Commun.* **2018**, *495* (3), 2344–2349.

[169] Booth, A. J.; Hadley, R.; Cornett, A. M.; Dreffs, A. A.; Matthes, S. A.; Tsui, J. L.; Weiss, K.; Horowitz, J. C.; Fiore, V. F.; Barker, T. H.; Moore, B. B.; Martinez, F. J.; Niklason, L. E.; White, E. S. Acellular Normal and Fibrotic Human Lung Matrices as a Culture System for in Vitro Investigation. *Am. J. Respir. Crit. Care Med.* **2012**, *186* (9), 866–876.

[170] Pankova, D.; Chen, Y.; Terajima, M.; Schliekelman, M. J.; Baird, B. N.; Fahrenholtz, M.; Sun, L.; Gill, B. J.; Vadakkan, T. J.; Kim, M. P.; Ahn, Y.-H.; Roybal, J. D.; Liu, X.; Parra

Cuentas, E. R.; Rodriguez, J.; Wistuba, I. I.; Creighton, C. J.; Gibbons, D. L.; Hicks, J. M.; Dickinson, M. E.; West, J. L.; Grande-Allen, K. J.; Hanash, S. M.; Yamauchi, M.; Kurie, J. M. Cancer-Associated Fibroblasts Induce a Collagen Cross-Link Switch in Tumor Stroma. *Mol. Cancer Res.* **2016**, *14* (3), 287–295.

[171] Shukla, V. C.; Higuita-Castro, N.; Nana-Sinkam, P.; Ghadiali, S. N. Substrate Stiffness Modulates Lung Cancer Cell Migration but Not Epithelial to Mesenchymal Transition. *J. Biomed. Mater. Res. - Part A* **2016**, *104* (5), 1182–1193.

[172] Rosenblum, D.; Joshi, N.; Tao, W.; Karp, J. M.; Peer, D. Progress and Challenges towards Targeted Delivery of Cancer Therapeutics. *Nat. Commun.* **2018**, *9* (1), 1410.

[173] Nichols, J. W.; Bae, Y. H. Odyssey of a Cancer Nanoparticle: From Injection Site to Site of Action. *Nano Today* **2012**, *7* (6), 606–618.

[174] Danhier, F. To Exploit the Tumor Microenvironment: Since the EPR Effect Fails in the Clinic, What Is the Future of Nanomedicine? *J. Control. Release* **2016**, *244*, 108–121.

[175] Lankelma, J.; Dekker, H.; Luque, R. F.; Luykx, S.; Hoekman, K.; Van Der Valk, P.; Van Diest, P. J.; Pinedo, H. M. Doxorubicin Gradients in Human Breast Cancer. *Clin. Cancer Res.* **1999**, *5* (7), 1703–1707.

[176] Tan, Y. H.; Liu, M.; Nolting, B.; Go, J. G.; Gervay-Hague, J.; Liu, G. Y. A Nanoengineering Approach for Investigation and Regulation of Protein Immobilization. *ACS Nano* **2008**, *2* (11), 2374–2384.

[177] Netti, P. A.; Berk, D. A.; Swartz, M. A.; Grodzinsky, A. J.; Jain, R. K. Role of Extracellular Matrix Assembly in Interstitial Transport in Solid Tumors. *Cancer Res.* **2000**, *60* (9), 2497–2503.

[178] Kenny, P. A.; Lee, G. Y.; Myers, C. A.; Neve, R. M.; Semeiks, J. R.; Spellman, P. T.; Lorenz, K.; Lee, E. H.; Barcellos-Hoff, M. H.; Petersen, O. W.; Gray, J. W.; Bissell, M. J. The Morphologies of Breast Cancer Cell Lines in Three-Dimensional Assays Correlate with Their Profiles of Gene Expression. *Mol. Oncol.* **2007**, *1* (1), 84–96.

[179] Boisselier, E.; Astruc, D. Gold Nanoparticles in Nanomedicine: Preparations, Imaging, Diagnostics, Therapies and Toxicity. *Chem. Soc. Rev.* **2009**, *38* (6), 1759–1782.

[180] Murphy, C. J.; Gole, A. M.; Stone, J. W.; Sisco, P. N.; Alkilany, A. M.; Goldsmith, E. C.; Baxter, S. C. Gold Nanoparticles in Biology: Beyond Toxicity to Cellular Imaging. *Acc. Chem. Res.* **2008**, *41* (12), 1721–1730.

[181] Wang, Y.; Black, K. C. L.; Luehmann, H.; Li, W.; Zhang, Y.; Cai, X.; Wan, D.; Liu, S. Y.; Li, M.; Kim, P.; Li, Z. Y.; Wang, L. V.; Liu, Y.; Xia, Y. Comparison Study of Gold Nanohexapods, Nanorods, and Nanocages for Photothermal Cancer Treatment. *ACS Nano* **2013**, *7* (3), 2068–2077.

[182] Gupta, R.; Rai, B. Effect of Size and Surface Charge of Gold Nanoparticles on Their Skin Permeability: A Molecular Dynamics Study. *Sci. Rep.* **2017**, *7* (1), 1–13.

[183] Carnovale, C.; Bryant, G.; Shukla, R.; Bansal, V. Identifying Trends in Gold Nanoparticle Toxicity and Uptake: Size, Shape, Capping Ligand, and Biological Corona. *ACS Omega* **2019**, *4* (1), 242–256.

[184] Yue, J.; Feliciano, T. J.; Li, W.; Lee, A.; Odom, T. W. Gold Nanoparticle Size and Shape

Effects on Cellular Uptake and Intracellular Distribution of SiRNA Nanoconstructs. *Bioconjug. Chem.* **2017**, *28* (6), 1791–1800.

[185] Chithrani, B. D.; Ghazani, A. A.; Chan, W. C. W. Determining the Size and Shape Dependence of Gold Nanoparticle Uptake into Mammalian Cells. *Nano Lett.* **2006**, *6* (4), 662–668.

[186] Cho, E. C.; Xie, J.; Wurm, P. A.; Xia, Y. Understanding the Role of Surface Charges in Cellular Adsorption versus Internalization by Selectively Removing Gold Nanoparticles on the Cell Surface with a I 2/KI Etchant. *Nano Lett.* **2009**, *9* (3), 1080–1084.

[187] Arvizo, R. R.; Miranda, O. R.; Thompson, M. A.; Pabelick, C. M.; Bhattacharya, R.; David Robertson, J.; Rotello, V. M.; Prakash, Y. S.; Mukherjee, P. Effect of Nanoparticle Surface Charge at the Plasma Membrane and Beyond. *Nano Lett.* **2010**, *10* (7), 2543–2548.

[188] Verma, A.; Stellacci, F. Effect of Surface Properties on Nanoparticle-Cell Interactions. *Small*. Small January 4, 2010, pp 12–21.

[189] Bor, G.; Azmi, I. D. M.; Yaghmur, A. Nanomedicines for Cancer Therapy: Current Status, Challenges and Future Prospects. *Therapeutic Delivery*. Future Medicine Ltd. February 1, 2019, pp 113–132.

[190] Zhang, Y. R.; Lin, R.; Li, H. J.; He, W. ling; Du, J. Z.; Wang, J. Strategies to Improve Tumor Penetration of Nanomedicines through Nanoparticle Design. *Wiley Interdisciplinary Reviews: Nanomedicine and Nanobiotechnology*. Wiley-Blackwell January 1, 2019.

[191] Muraca, F.; Boselli, L.; Castagnola, V.; Dawson, K. A. Ultrasmall Gold Nanoparticle Cellular Uptake: Influence of Transient Bionano Interactions. *ACS Appl. Bio Mater.* **2020**.

[192] Chithrani, D. B. Intracellular Targeting Using Surface-Modified Gold Nanoparticles. In *Biomedical Applications of Functionalized Nanomaterials: Concepts, Development and Clinical Translation*; Elsevier, 2018; pp 315–333.

[193] Xie, X.; Liao, J.; Shao, X.; Li, Q.; Lin, Y. The Effect of Shape on Cellular Uptake of Gold Nanoparticles in the Forms of Stars, Rods, and Triangles. *Sci. Rep.* **2017**, *7* (1), 1–9.

[194] Moser, F.; Hildenbrand, G.; Müller, P.; Al Saroori, A.; Biswas, A.; Bach, M.; Wenz, F.; Cremer, C.; Burger, N.; Veldwijk, M. R.; Hausmann, M. Cellular Uptake of Gold Nanoparticles and Their Behavior as Labels for Localization Microscopy. *Biophys. J.* **2016**, *110* (4), 947–953.

[195] Valente, K. P.; Thind, S. S.; Akbari, M.; Suleman, A.; Brolo, A. G. Collagen Type I-Gelatin Methacryloyl Composites: Mimicking the Tumor Microenvironment. *ACS Biomater. Sci. Eng.* **2019**, *5* (6), 2887–2898.

[196] Crank, J. *The Mathematics of Diffusion: 2d Ed*; Clarendon Press, 1975.

[197] Nanda, S.; Sood, N.; Reddy, B. V. K.; Markandeywar, T. S. Preparation and Characterization of Poly(Vinyl Alcohol)-Chondroitin Sulphate Hydrogel as Scaffolds for Articular Cartilage Regeneration. *Indian J. Mater. Sci.* **2013**, 1–8.

[198] Vishal Gupta, N.; Shivakumar, H. G. Preparation and Characterization of Superporous Hydrogels as Gastroretentive Drug Delivery System for Rosiglitazone Maleate. *DARU, J.*

Pharm. Sci. **2010**, *18* (3), 200–210.

[199] Gabizon, A. A.; Shmeeda, H.; Zalipsky, S. Pros and Cons of the Liposome Platform in Cancer Drug Targeting. *J. Liposome Res.* **2006**, *16* (3), 175–183.

[200] Caliceti, P.; Veronese, F. M. Pharmacokinetic and Biodistribution Properties of Poly(Ethylene Glycol)-Protein Conjugates. *Adv. Drug Deliv. Rev.* **2003**, *55* (10), 1261–1277.

[201] Pluen, A.; Boucher, Y.; Ramanujan, S.; McKee, T. D.; Gohongi, T.; Di Tomaso, E.; Brown, E. B.; Izumi, Y.; Campbell, R. B.; Berk, D. A.; Jain, R. K. Role of Tumor-Host Interactions in Interstitial Diffusion of Macromolecules: Cranial vs. Subcutaneous Tumors. *Proc. Natl. Acad. Sci. U. S. A.* **2001**, *98* (8), 4628–4633.

[202] Freudenberg, U.; Behrens, S. H.; Welzel, P. B.; Müller, M.; Grimmer, M.; Salchert, K.; Taeger, T.; Schmidt, K.; Pompe, W.; Werner, C. Electrostatic Interactions Modulate the Conformation of Collagen I. *Biophys. J.* **2007**, *92* (6), 2108–2119.

[203] Liu, X.; Huang, N.; Li, H.; Jin, Q.; Ji, J. Surface and Size Effects on Cell Interaction of Gold Nanoparticles with Both Phagocytic and Nonphagocytic Cells. *Langmuir* **2013**, *29* (29), 9138–9148.

[204] Jiang, Y.; Huo, S.; Mizuhara, T.; Das, R.; Lee, Y. W.; Hou, S.; Moyano, D. F.; Duncan, B.; Liang, X. J.; Rotello, V. M. The Interplay of Size and Surface Functionality on the Cellular Uptake of Sub-10 Nm Gold Nanoparticles. *ACS Nano* **2015**, *9* (10), 9986–9993.

[205] Duan, X.; Li, Y. Physicochemical Characteristics of Nanoparticles Affect Circulation, Biodistribution, Cellular Internalization, and Trafficking. *Small*. John Wiley & Sons, Ltd May 27, 2013, pp 1521–1532.

[206] Albanese, A.; Tang, P. S.; Chan, W. C. W. The Effect of Nanoparticle Size, Shape, and Surface Chemistry on Biological Systems. *Annu. Rev. Biomed. Eng.* **2012**, *14* (1), 1–16.

[207] Liang, M.; Lin, I. C.; Whittaker, M. R.; Minchin, R. F.; Monteiro, M. J.; Toth, I. Cellular Uptake of Densely Packed Polymer Coatings on Gold Nanoparticles. *ACS Nano* **2010**, *4* (1), 403–413.

[208] Lunnoo, T.; Assawakhajornsak, J.; Puangmali, T. In Silico Study of Gold Nanoparticle Uptake into a Mammalian Cell: Interplay of Size, Shape, Surface Charge, and Aggregation. *J. Phys. Chem. C* **2019**, *123* (6), 3801–3810.

[209] Mailänder, V.; Landfester, K. Interaction of Nanoparticles with Cells. *Biomacromolecules*. American Chemical Society September 14, 2009, pp 2379–2400.

[210] Lu, H.; Su, J.; Mamdooh, R.; Li, Y.; Stenzel, M. H. Cellular Uptake of Gold Nanoparticles and Their Movement in 3D Multicellular Tumor Spheroids: Effect of Molecular Weight and Grafting Density of Poly(2-Hydroxyl Ethyl Acrylate). *Macromol. Biosci.* **2020**, *20* (1).

[211] Huang, K.; Ma, H.; Liu, J.; Huo, S.; Kumar, A.; Wei, T.; Zhang, X.; Jin, S.; Gan, Y.; Wang, P. C.; He, S.; Zhang, X.; Liang, X. J. Size-Dependent Localization and Penetration of Ultrasmall Gold Nanoparticles in Cancer Cells, Multicellular Spheroids, and Tumors in Vivo. *ACS Nano* **2012**, *6* (5), 4483–4493.

[212] Bugno, J.; Hsu, H. J.; Pearson, R. M.; Noh, H.; Hong, S. Size and Surface Charge of

Engineered Poly(Amidoamine) Dendrimers Modulate Tumor Accumulation and Penetration: A Model Study Using Multicellular Tumor Spheroids. *Mol. Pharm.* **2016**, *13* (7), 2155–2163.

[213] Leong, D. T.; Ng, K. W. Probing the Relevance of 3D Cancer Models in Nanomedicine Research. *Advanced Drug Delivery Reviews*. Elsevier December 15, 2014, pp 95–106.

[214] Lee, J.-H.; Kim, H.-W. Emerging Properties of Hydrogels in Tissue Engineering. *J. Tissue Eng.* **2018**, *9*, 2041731418768285.

[215] Zhu, J.; Marchant, R. E. Design Properties of Hydrogel Tissue-Engineering Scaffolds. *Expert Rev. Med. Devices* **2011**, *8* (5), 607–626.

[216] Drury, J. L.; Mooney, D. J. Hydrogels for Tissue Engineering: Scaffold Design Variables and Applications. *Biomaterials* **2003**, *24* (24), 4337–4351.

[217] El-Sherbiny, I. M.; Yacoub, M. H. Hydrogel Scaffolds for Tissue Engineering: Progress and Challenges. *Glob. Cardiol. Sci. Pract.* **2013**, *2013* (3), 316–342.

[218] Ying, L.; Zhu, Z.; Xu, Z.; He, T.; Li, E.; Guo, Z.; Liu, F.; Jiang, C.; Wang, Q. Cancer Associated Fibroblast-Derived Hepatocyte Growth Factor Inhibits the Paclitaxel-Induced Apoptosis of Lung Cancer A549 Cells by Up-Regulating the PI3K/Akt and GRP78 Signaling on a Microfluidic Platform. *PLoS One* **2015**, *10* (6), e0129593.

[219] Sosnik, A.; Seremeta, K.; Sosnik, A.; Seremeta, K. P. Polymeric Hydrogels as Technology Platform for Drug Delivery Applications. *Gels* **2017**, *3* (3), 25.

[220] Daly, A. C.; Riley, L.; Segura, T.; Burdick, J. A. Hydrogel Microparticles for Biomedical Applications. *Nature Reviews Materials*. Nature Research January 1, 2020, pp 20–43.

[221] Rizwan, M.; Yahya, R.; Hassan, A.; Yar, M.; Azzahari, A.; Selvanathan, V.; Sonsudin, F.; Abouloula, C.; Rizwan, M.; Yahya, R.; Hassan, A.; Yar, M.; Azzahari, A. D.; Selvanathan, V.; Sonsudin, F.; Abouloula, C. N. PH Sensitive Hydrogels in Drug Delivery: Brief History, Properties, Swelling, and Release Mechanism, Material Selection and Applications. *Polymers (Basel).* **2017**, *9* (12), 137.

[222] Kocak, G.; Tuncer, C.; Bütün, V. PH-Responsive Polymers. *Polym. Chem.* **2017**, *8* (1), 144–176.

[223] Deligkaris, K.; Tadele, T. S.; Olthuis, W.; van den Berg, A. Hydrogel-Based Devices for Biomedical Applications. *Sensors and Actuators, B: Chemical*. Elsevier June 3, 2010, pp 765–774.

[224] Stuart, M. A. C.; Huck, W. T. S.; Genzer, J.; Müller, M.; Ober, C.; Stamm, M.; Sukhorukov, G. B.; Szleifer, I.; Tsukruk, V. V.; Urban, M.; Winnik, F.; Zauscher, S.; Luzinov, I.; Minko, S. Emerging Applications of Stimuli-Responsive Polymer Materials. *Nature Materials*. Nature Publishing Group January 22, 2010, pp 101–113.

[225] Buenger, D.; Topuz, F.; Groll, J. Hydrogels in Sensing Applications. *Progress in Polymer Science*. Pergamon December 1, 2012, pp 1678–1719.

[226] Ramos, J.; Forcada, J.; Hidalgo-Alvarez, R. Cationic Polymer Nanoparticles and Nanogels: From Synthesis to Biotechnological Applications. *Chemical Reviews*. American Chemical Society January 8, 2014, pp 367–428.

[227] Boedtkjer, E.; Pedersen, S. F. The Acidic Tumor Microenvironment as a Driver of Cancer.

Annu. Rev. Physiol. **2020**, *82* (1), 103–126.

[228] Du, J. Z.; Sun, T. M.; Song, W. J.; Wu, J.; Wang, J. A Tumor-Acidity-Activated Charge-Conversional Nanogel as an Intelligent Vehicle for Promoted Tumoral-Cell Uptake and Drug Delivery. *Angew. Chemie - Int. Ed.* **2010**, *49* (21), 3621–3626.

[229] Johnson, R. P.; Jeong, Y.-I.; Choi, E.; Chung, C.-W.; Kang, D. H.; Oh, S.-O.; Suh, H.; Kim, I. Biocompatible Poly(2-Hydroxyethyl Methacrylate)-b-Poly(L-Histidine) Hybrid Materials for PH-Sensitive Intracellular Anticancer Drug Delivery. *Adv. Funct. Mater.* **2012**, *22* (5), 1058–1068.

[230] Duan, C.; Zhang, D.; Wang, F.; Zheng, D.; Jia, L.; Feng, F.; Liu, Y.; Wang, Y.; Tian, K.; Wang, F.; Zhang, Q. Chitosan-g-Poly(N-Isopropylacrylamide) Based Nanogels for Tumor Extracellular Targeting. *Int. J. Pharm.* **2011**, *409* (1–2), 252–259.

[231] Du, H.; Liu, M.; Yang, X.; Zhai, G. The Design of PH-Sensitive Chitosan-Based Formulations for Gastrointestinal Delivery. *Drug Discovery Today*. Elsevier Ltd August 1, 2015, pp 1004–1011.

[232] Raja, S. T. K.; Thiruselvi, T.; Mandal, A. B.; Gnanamani, A. PH and Redox Sensitive Albumin Hydrogel: A Self-Derived Biomaterial. *Sci. Rep.* **2015**, *5*.

[233] Gao, X.; He, C.; Xiao, C.; Zhuang, X.; Chen, X. Biodegradable PH-Responsive Polyacrylic Acid Derivative Hydrogels with Tunable Swelling Behavior for Oral Delivery of Insulin. *Polymer (Guildf).* **2013**, *54* (7), 1786–1793.

[234] Samal, S. K.; Dash, M.; Van Vlierberghe, S.; Kaplan, D. L.; Chiellini, E.; Van Blitterswijk, C.; Moroni, L.; Dubruel, P. Cationic Polymers and Their Therapeutic Potential. *Chemical Society Reviews*. The Royal Society of Chemistry October 8, 2012, pp 7147–7194.

[235] Claaßen, C.; Claaßen, M. H.; Truffault, V.; Sewald, L.; Tovar, G. E. M.; Borchers, K.; Southan, A. Quantification of Substitution of Gelatin Methacryloyl: Best Practice and Current Pitfalls. *Biomacromolecules* **2018**, *19* (1), 42–52.

[236] Wang, Z.; Tian, Z.; Menard, F.; Kim, K. Comparative Study of Gelatin Methacrylate Hydrogels from Different Sources for Biofabrication Applications. *Biofabrication* **2017**, *9* (4), 044101.

[237] Jaipan, P.; Nguyen, A.; Narayan, R. J. Gelatin-Based Hydrogels for Biomedical Applications. *MRS Commun.* **2017**, *7* (3), 416–426.

[238] Lee, B. H.; Shirahama, H.; Cho, N.-J.; Tan, L. P. Efficient and Controllable Synthesis of Highly Substituted Gelatin Methacrylamide for Mechanically Stiff Hydrogels. *RSC Adv.* **2015**, *5* (128), 106094–106097.

[239] Hoch, E.; Schuh, C.; Hirth, T.; Tovar, G. E. M.; Borchers, K. Stiff Gelatin Hydrogels Can Be Photo-Chemically Synthesized from Low Viscous Gelatin Solutions Using Molecularly Functionalized Gelatin with a High Degree of Methacrylation. *J. Mater. Sci. Mater. Med.* **2012**, *23* (11), 2607–2617.

[240] Reis, A. V.; Fajardo, A. R.; Schuquel, I. T. A.; Guilherme, M. R.; Vidotti, G. J.; Rubira, A. F.; Muniz, E. C. Reaction of Glycidyl Methacrylate at the Hydroxyl and Carboxylic Groups of Poly(Vinyl Alcohol) and Poly(Acrylic Acid): Is This Reaction Mechanism Still Unclear? *J. Org. Chem.* **2009**, *74* (10), 3750–3757.

[241] Lai, T. C.; Yu, J.; Tsai, W. B. Gelatin Methacrylate/Carboxybetaine Methacrylate Hydrogels with Tunable Crosslinking for Controlled Drug Release. *J. Mater. Chem. B* **2016**, *4* (13), 2304–2313.

[242] Jung, J.; Oh, J. Swelling Characterization of Photo-Cross-Linked Gelatin Methacrylate Spherical Microgels for Bioencapsulation. *e-Polymers* **2014**, *14* (3), 161–168.

[243] Kim, S. H.; Yeon, Y. K.; Lee, J. M.; Chao, J. R.; Lee, Y. J.; Seo, Y. B.; Sultan, M. T.; Lee, O. J.; Lee, J. S.; Yoon, S. Il; Hong, I. S.; Khang, G.; Lee, S. J.; Yoo, J. J.; Park, C. H. Precisely Printable and Biocompatible Silk Fibroin Bioink for Digital Light Processing 3D Printing. *Nat. Commun.* **2018**, *9* (1), 1–14.

[244] Suvarnapathaki, S.; Ramos, R.; Sawyer, S. W.; McLoughlin, S.; Ramos, A.; Venn, S.; Soman, P. Generation of Cell-Laden Hydrogel Microspheres Using 3D Printing-Enabled Microfluidics. *J. Mater. Res.* **2018**, *33* (14), 2012–2018.

[245] Hafidz, M.; Yaakob, C. M.; Amin, I.; Noorfaizan, A. *Chemical and Functional Properties of Bovine and Porcine Skin Gelatin*; 2011; Vol. 18.

[246] Neves, N. M.; Reis, R. L. *Biomaterials from Nature for Advanced Devices and Therapies*; Neves, N. M., Reis, R. L., Eds.; John Wiley & Sons, Inc.: Hoboken, New Jersey, 2016.

[247] Gu, L.; Li, T.; Song, X.; Yang, X.; Li, S.; Chen, L.; Liu, P.; Gong, X.; Chen, C.; Sun, L. Preparation and Characterization of Methacrylated Gelatin/Bacterial Cellulose Composite Hydrogels for Cartilage Tissue Engineering. *Regen. Biomater.* **2020**, *7* (2), 195–202.

[248] Klotz, B. J.; Gawlitta, D.; Rosenberg, A. J. W. P.; Malda, J.; Melchels, F. P. W. Gelatin-Methacryloyl Hydrogels: Towards Biofabrication-Based Tissue Repair. *Trends in Biotechnology*. Elsevier Ltd May 1, 2016, pp 394–407.

[249] Gao, Q.; Niu, X.; Shao, L.; Zhou, L.; Lin, Z.; Sun, A.; Fu, J.; Chen, Z.; Hu, J.; Liu, Y.; He, Y. 3D Printing of Complex GelMA-Based Scaffolds with Nanoclay. *Biofabrication* **2019**, *11* (3), 035006.

[250] Yin, J.; Yan, M.; Wang, Y.; Fu, J.; Suo, H. 3D Bioprinting of Low-Concentration Cell-Laden Gelatin Methacrylate (GelMA) Bioinks with a Two-Step Cross-Linking Strategy. *ACS Appl. Mater. Interfaces* **2018**, *10* (8), 6849–6857.

[251] Liu, J.; Li, L.; Suo, H.; Yan, M.; Yin, J.; Fu, J. 3D Printing of Biomimetic Multi-Layered GelMA/NHA Scaffold for Osteochondral Defect Repair. *Mater. Des.* **2019**, *171*, 107708.

[252] Modaresifar, K.; Hadjizadeh, A.; Niknejad, H. Design and Fabrication of GelMA/Chitosan Nanoparticles Composite Hydrogel for Angiogenic Growth Factor Delivery. *Artif. Cells, Nanomedicine, Biotechnol.* **2017**, *46* (8), 1–10.

[253] Vigata, M.; Meinert, C.; Pahoff, S.; Bock, N.; Hutmacher, D. W. Gelatin Methacryloyl Hydrogels Control the Localized Delivery of Albumin-Bound Paclitaxel. *Polymers (Basel).* **2020**, *12* (2), 501.

[254] Gong, H.; Fei, H.; Xu, Q.; Gou, M.; Chen, H. H. 3D-engineered GelMA Conduit Filled with ECM Promotes Regeneration of Peripheral Nerve. *J. Biomed. Mater. Res. Part A* **2020**, *108* (3), 805–813.

[255] Kilic Bektas, C.; Hasirci, V. Cell Loaded 3D Bioprinted GelMA Hydrogels for Corneal Stroma Engineering. *Biomater. Sci.* **2020**, *8* (1), 438–449.

[256] Nguyen, A. H.; McKinney, J.; Miller, T.; Bongiorno, T.; McDevitt, T. C. Gelatin Methacrylate Microspheres for Controlled Growth Factor Release. *Acta Biomater.* **2015**, *13*, 101–110.

[257] Gyles, D. A.; Castro, L. D.; Silva, J. O. C.; Ribeiro-Costa, R. M. A Review of the Designs and Prominent Biomedical Advances of Natural and Synthetic Hydrogel Formulations. *European Polymer Journal*. Elsevier Ltd March 1, 2017, pp 373–392.

[258] Pepelanova, I.; Kruppa, K.; Scheper, T.; Lavrentieva, A. Gelatin-Methacryloyl (GelMA) Hydrogels with Defined Degree of Functionalization as a Versatile Toolkit for 3D Cell Culture and Extrusion Bioprinting. *Bioengineering* **2018**, *5* (3).

[259] Zhu, M.; Wang, Y.; Ferracci, G.; Zheng, J.; Cho, N. J.; Lee, B. H. Gelatin Methacryloyl and Its Hydrogels with an Exceptional Degree of Controllability and Batch-to-Batch Consistency. *Sci. Rep.* **2019**, *9* (1), 1–13.

[260] Xia, L. W.; Xie, R.; Ju, X. J.; Wang, W.; Chen, Q.; Chu, L. Y. Nano-Structured Smart Hydrogels with Rapid Response and High Elasticity. *Nat. Commun.* **2013**, *4* (1), 1–11.

[261] Lu, S.; Neoh, K. G.; Huang, C.; Shi, Z.; Kang, E. T. Polyacrylamide Hybrid Nanogels for Targeted Cancer Chemotherapy via Co-Delivery of Gold Nanoparticles and MTX. *J. Colloid Interface Sci.* **2013**, *412*, 46–55.

[262] Kim, J.-H.; Boote, B. W.; Pham, J. A.; Hu, J.; Byun, H. Thermally Tunable Catalytic and Optical Properties of Gold–Hydrogel Nanocomposites. *Nanotechnology* **2012**, *23* (27), 275606.

[263] Krishnadasan, S.; Brown, R. J. C.; DeMello, A. J.; DeMello, J. C. Intelligent Routes to the Controlled Synthesis of Nanoparticles. *Lab Chip* **2007**, *7* (11), 1434–1441.

[264] Zhao, C.-X.; Middelberg, A. P. J. Synthesis and Characterization of Nanomaterials Using Microfluidic Technology. In *Handbook of Nanoparticles*; Springer International Publishing, 2015; pp 1–16.

[265] Kim, J.; Gauvin, R.; Yoon, H. J.; Kim, J. H.; Kwon, S. M.; Park, H. J.; Baek, S. H.; Cha, J. M.; Bae, H. Skin Penetration-Inducing Gelatin Methacryloyl Nanogels for Transdermal Macromolecule Delivery. *Macromol. Res.* **2016**, *24* (12), 1115–1125.

[266] Kang, M. G.; Lee, M. Y.; Cha, J. M.; Lee, J. K.; Lee, S. C.; Kim, J.; Hwang, Y. S.; Bae, H. Nanogels Derived from Fish Gelatin: Application to Drug Delivery System. *Mar. Drugs* **2019**, *17* (4).

[267] Huang, K.; He, Y.; Zhu, Z.; Guo, J.; Wang, G.; Deng, C.; Zhong, Z. Small, Traceable, Endosome-Disrupting, and Bioresponsive Click Nanogels Fabricated via Microfluidics for CD44-Targeted Cytoplasmic Delivery of Therapeutic Proteins. *ACS Appl. Mater. Interfaces* **2019**, *11* (25), 22171–22180.

[268] Huo, S.; Ma, H.; Huang, K.; Liu, J.; Wei, T.; Jin, S.; Zhang, J.; He, S.; Liang, X. J. Superior Penetration and Retention Behavior of 50 Nm Gold Nanoparticles in Tumors. *Cancer Res.* **2013**, *73* (1), 319–330.

[269] Bennie, L. A.; McCarthy, H. O.; Coulter, J. A. Enhanced Nanoparticle Delivery Exploiting Tumour-Responsive Formulations. *Cancer Nanotechnology*. BioMed Central Ltd. November 21, 2018, pp 1–20.

[270] Kalyane, D.; Raval, N.; Maheshwari, R.; Tambe, V.; Kalia, K.; Tekade, R. K. Employment of Enhanced Permeability and Retention Effect (EPR): Nanoparticle-Based Precision Tools for Targeting of Therapeutic and Diagnostic Agent in Cancer. *Materials Science and Engineering C*. Elsevier Ltd May 1, 2019, pp 1252–1276.

[271] Phillips, M. A.; Gran, M. L.; Peppas, N. A. Targeted Nanodelivery of Drugs and Diagnostics. *Nano Today*. Elsevier April 1, 2010, pp 143–159.

[272] Zhang, X. D.; Wu, D.; Shen, X.; Chen, J.; Sun, Y. M.; Liu, P. X.; Liang, X. J. Size-Dependent Radiosensitization of PEG-Coated Gold Nanoparticles for Cancer Radiation Therapy. *Biomaterials* **2012**, *33* (27), 6408–6419.

[273] Chithrani, D. B.; Jelveh, S.; Jalali, F.; van Prooijen, M.; Allen, C.; Bristow, R. G.; Hill, R. P.; Jaffray, D. A. Gold Nanoparticles as Radiation Sensitizers in Cancer Therapy. *Radiat. Res.* **2010**, *173* (6), 719.

[274] Lee, J. N.; Park, C.; Whitesides, G. M. Solvent Compatibility of Poly(Dimethylsiloxane)-Based Microfluidic Devices. *Anal. Chem.* **2003**, *75* (23), 6544–6554.

[275] Du Toit, H.; Macdonald, T. J.; Huang, H.; Parkin, I. P.; Gavriilidis, A. Continuous Flow Synthesis of Citrate Capped Gold Nanoparticles Using UV Induced Nucleation. *RSC Adv.* **2017**, *7* (16), 9632–9638.

[276] Chiesa, E.; Dorati, R.; Pisani, S.; Conti, B.; Bergamini, G.; Modena, T.; Genta, I. The Microfluidic Technique and the Manufacturing of Polysaccharide Nanoparticles. *Pharmaceutics*. MDPI AG December 1, 2018.

[277] Chan, H. F.; Ma, S.; Leong, K. W. Can Microfluidics Address Biomanufacturing Challenges in Drug/Gene/Cell Therapies? *Regen. Biomater.* **2016**, *3* (2), 87.

[278] Bazban-Shotorbani, S.; Dashtimoghadam, E.; Karkhaneh, A.; Hasani-Sadrabadi, M. M.; Jacob, K. I. Microfluidic Directed Synthesis of Alginate Nanogels with Tunable Pore Size for Efficient Protein Delivery. *Langmuir* **2016**, *32* (19), 4996–5003.

[279] Jain, R. K.; Stylianopoulos, T. Delivering Nanomedicine to Solid Tumors. *Nature Reviews Clinical Oncology*. Nat Rev Clin Oncol November 2010, pp 653–664.

[280] Tee, J. K.; Yip, L. X.; Tan, E. S.; Santitewagun, S.; Prasath, A.; Ke, P. C.; Ho, H. K.; Leong, D. T. Nanoparticles' Interactions with Vasculature in Diseases. *Chemical Society Reviews*. Royal Society of Chemistry November 7, 2019, pp 5381–5407.

[281] Maeda, H. Macromolecular Therapeutics in Cancer Treatment: The EPR Effect and Beyond. *Journal of Controlled Release*. J Control Release December 10, 2012, pp 138–144.

[282] Maeda, H. Toward a Full Understanding of the EPR Effect in Primary and Metastatic Tumors as Well as Issues Related to Its Heterogeneity. *Advanced Drug Delivery Reviews*. Elsevier August 30, 2015, pp 3–6.

[283] Habeeb, A. F. S. A. Determination of Free Amino Groups in Proteins by Trinitrobenzenesulfonic Acid. *Anal. Biochem.* **1966**, *14* (3), 328–336.

[284] Zuo, Y.; Xiao, W.; Chen, X.; Tang, Y.; Luo, H.; Fan, H. Bottom-up Approach to Build Osteon-like Structure by Cell-Laden Photocrosslinkable Hydrogel. *Chem. Commun.* **2012**, *48* (26), 3170.

[285] Staunton, J. R.; Doss, B. L.; Lindsay, S.; Ros, R. Correlating Confocal Microscopy and Atomic Force Indentation Reveals Metastatic Cancer Cells Stiffen during Invasion into Collagen i Matrices. *Sci. Rep.* **2016**, *6* (1), 19686.

[286] Raub, C. B.; Suresh, V.; Krasieva, T.; Lyubovitsky, J.; Mih, J. D.; Putnam, A. J.; Tromberg, B. J.; George, S. C. Noninvasive Assessment of Collagen Gel Microstructure and Mechanics Using Multiphoton Microscopy. *Biophys. J.* **2007**, *92* (6), 2212–2222.

[287] Long, R.; Hall, M. S.; Wu, M.; Hui, C. Y. Effects of Gel Thickness on Microscopic Indentation Measurements of Gel Modulus. *Biophys. J.* **2011**, *101* (3), 643–650.

[288] Hertz, H. Ueber Die Berührung Fester Elastischer Körper. *J. fur die Reine und Angew. Math.* **1882**, *1882* (92), 156–171.